National Institute of Astrophysics, Optics, and Electronics

Study of Optoelectronic Characteristics in Germanium-Silicon Films Deposited by Low Frequency Plasma and Related Devices

Presented by

Francisco Temoltzi Avila

A thesis submitted in partial fulfillment of the

requirements for the degree of

Ph. D. in Electronics

Advisors:

Dr. Andrey Kosarev, INAOE

Dr. Oleksandr Malik, INAOE

Dedicada a:

Mis padres: Francisco Temoltzi Pilotzi y Gloria Juana Avila Salauz, y a mis hermanos: Raul, Alberto, Marilu, Daniel, Javier, Rigoberto, Nely y Yeni.

Abstract

The thin film photovoltaic devices are considered as a promising alternative to conventional crystalline silicon solar cells because: 1) less material is needed per unit area to fully absorb the visible part of the solar spectrum (i.e., the thin film solar cells need intrinsic films with thickness of around $\approx 0.3\mu m$ to fully absorb the visible part of the solar spectrum, whereas the dominant crystalline and polycrystalline silicon solar cells need intrinsic films with thickness of around $\approx 300\mu m$), 2) can be fabricated photovoltaic modules of very large area in comparison with crystalline and polycrystalline silicon photovoltaic modules, 3) can be perform fabrication processes at low temperature using a wide variety of substrates (flexible, rigid, metals or insulators), films (contacts, buffers, active films, reflectors, etc.) and semiconductor materials (silicon, germanium, cadmium telluride, etc.) deposited by a variety of deposition techniques (PVD, CVD, ECD, plasma-based, hybrid, etc.), and 4) manufacturing and installation costs are significantly lower. Consequently, a wide variety of these technologies are being developed and marketed, including amorphous silicon, polymorphous silicon, microcrystalline silicon, polycrystalline silicon, silicon-germanium alloys, cadmium-telluride alloys, copper-indium-gallium-selenium alloys, organic materials, etc. These developments have made it necessary a better understand of the physics of the thin film solar cell devices. However, at present there are still many important issues that have not been studied enough.

The present work is devoted to a systematic study of the optoelectronic characteristics of the germanium-silicon thin films and related photovoltaic devices. The germanium-silicon thin films were deposited by low frequency ($110KHz$) plasma enchanced chemical vapor deposition on glass Corning 1737. The deposition temperature was changed over a range from $T_s = 70℃$ to 300℃. The results obtained from the optoelectronic characteristics showed that the deposition temperature

significantly affect the structural and photoelectric properties of the silicon-germanium thin films. In the germanium-silicon thin films the optoelectronic characteristics (e.g., photoconductivity, σ_{ph}, defects ratio, R_{def}, and energy $E_{u_{pc}}$) which are important for photovoltaic devices were extracted from the spectral response of photoconductivity as a function of the temperature deposition.

The study of the optoelectronic characteristics of photovoltaic devices was performed in photovoltaic devices manufactured with different materials and technologies in different laboratories (i.e., microcrystalline and polymorphous silicon p-i-n photovoltaic structures from the Ecole-Polytechnique, France, GeSi:H thin film photovoltaic structures from the National Institute of Astrophysics, Optics and Electronics, Mexico, and organic photovoltaic devices from the University of Cologne, Germany).

The study was divided into three sections in order to understand and reveal problems related to the performance of photovoltaic devices, problems related to the physical mechanisms that govern the operation of the photovoltaic devices and problems related to the manufacturing technology. The results showed that the performance characteristics (i.e., open circuit voltage, V_{oc}, short circuit current, I_{sc}, fill factor , FF, and power conversion efficiency, η) are not able to provide enough information to understand and develop the technology of photovoltaic devices. Performance characteristics are commonly used in the state-of-art to compare the performance of the photovoltaic devices locally and globally. The results also showed that depending on the material used (e.g., microcrystalline silicon, polymorphous silicon, germanium-silicon alloys or organic materials), the performance characteristics are affected by different operating mechanisms (e.g., surface recombination, carriers transports, built-in potential, optical absorption, etc.) or by different technological problems (e.g., metal-semiconductor contact, shunt leakage current, etc.).

Resumen

Las tecnologías fotovoltaicas de película delgada se consideran una alternativa muy prometedora a los paneles cristalinos convencionales debido a que: 1) se necesita menos material por unidad de área para absorber completamente la parte visible del espectro solar (es decir, las celdas solares de película delgada necesitan películas intrínsecas con espesores de $\approx 0.3\mu m$ para absorber completamente la parte visible del espectro solar, mientras que las celdas solares dominantes de silicio cristalino y silicio policristalino necesitan películas intrínsecas con espesores de $\approx 300\mu m$), 2) se pueden fabricar módulos fotovoltaicos de área muy grande en comparación con los módulos fotovoltaicos de silicio cristalino y silicio policristalino, 3) se pueden realizar procesos de fabricación a bajas temperaturas ($< 300℃$) utilizando una amplia variedad de substratos (flexibles, rígidos, metales o aislantes), películas (contactos, buffers, películas activas, reflectores, etc.) y materiales semiconductores (Silicio, Germanio, Teluro de Cadmio, etc.) depositados por una gran variedad de técnicas de depósito (PVD, CVD, ECD, basados en plasma, híbridos, etc.), y 4) los costos de fabricación e instalación son significativamente más bajos. En consecuencia, se está desarrollado y comercializado una amplia variedad de estas tecnologías, tales como el silicio amorfo, silicio polimorfo, silicio microcristalino, silicio policristalino, aleaciones de silicio-germanio, teluro de cadmio, aleaciones de cobre-indio-galio-selenio, materiales orgánicos, etc. Estos acontecimientos han impuesto la necesidad de comprender mejor la física de los dispositivos solares de película delgada. Sin embargo, en la actualidad todavía hay muchas cuestiones importantes que no se han estudiado suficientemente.

El presente trabajo está enfocado hacia un estudio sistemático de las características optoelectrónicas de las películas delgadas de Germanio-Silicio y de los dispositivos fotovoltaicos relacionados. Las películas delgadas de Germanio-Silicio fueron

depositadas a baja frecuencia ($110KHz$) por depósito químico en fase vapor asistido por plasma (PECVD) sobre sustratos de vidrio "Corning 1737". La temperatura de depósito se varió dentro de un rango de $T_s = 70℃$ a $300℃$. Los resultados obtenidos a partir de las características optoelectrónicas demostraron que la temperatura de depósito afecta significativamente las propiedades estructurales y las propiedades fotoeléctricas de las películas delgadas de Germanio-Silicio. Las características optoelectrónicas de las películas (es decir, fotoconductividad, σ_{ph}, razón de defectos, R_{def}, y energía $E_{u_{pc}}$) se extrajeron de la respuesta espectral de la fotoconductividad en función de la temperatura de depósito.

El estudio de las características optoelectrónicas de los dispositivos fotovoltaicos se llevó a cabo en dispositivos fabricados con diferentes materiales y con diferentes tecnologías en diferentes laboratorios (es decir, estructuras p-i-n fotovoltaicas de silicio microcristalino y silicio polimorfo proporcionados por el "Ecole Polytechnique" de Francia, estructuras fotovoltaicas de $Ge_{0.97}Si_{0.03}$:H fabricadas en el Instituto Nacional de Astrofísica, Óptica y Electrónica, y dispositivos fotovoltaicos orgánicos proporcionados por la Universidad de Colonia de Alemania).

El estudio se dividió en tres secciones con la finalidad de comprender y revelar problemas relacionados con la operación de los dispositivos fotovoltaicos, problemas relacionados con los mecanismos físicos que rigen el funcionamiento de los dispositivos fotovoltaicos y problemas relacionados con la tecnología de fabricación de dispositivos fotovoltaicos. Los resultados demostraron que las características de funcionamiento (es decir, el voltaje de circuito abierto, V_{oc}, la corriente de corto circuito, I_{sc}, el factor de llenado, FF, y la eficiencia de conversión de energía, η) no son capaces de proporcionar suficiente información para comprender y desarrollar la tecnología de los dispositivos fotovoltaicos. Sin embargo, estas características se

utilizan comúnmente en el estado del arte para comparar el rendimiento de los dispositivos fotovoltaicos local y globalmente. Los resultados también demostraron que, dependiendo del material utilizado (por ejemplo, silicio microcristalino, silicio polimorfo, aleaciones de Silicio-Germanio o materiales orgánicos) las características de funcionamiento se ven afectados por diferentes mecanismos de operación (por ejemplo, la recombinación superficial, el transporte de los portadores de carga, el potencial interconstruido, la absorción óptica, etc.) o por diferentes problemas tecnológicos (por ejemplo, la resistencia de contacto metal-semiconductor, las corrientes de fuga, etc.).

Acknowledgments

Specially, I thank to my family: My mother, my father and my brothers and sisters for their help and their unconditional support.

To the Instituto Nacional de Astrofísica, Óptica y Electrónica for provide the facilities and work environment for the successful development of this work.

I acknowledges support from Consejo Nacional de Ciencia y Tecnologia (CONACyT) through the PhD scholarship number 46317.

This work would not have been possible without the funding provided by the SENER-CONACyT under project number 152244.

I would like to acknowledge my supervisors Dr. Andrey Kosarev and Dr. Oleksandr Malik for having accepted me as a doctoral student in the Electronics Department in the INAOE and share me their invaluable knowledge.

Also I would like to tank to Dr. Pere Roca I. Cabarrocas (professors at the Ecole Polytechnique, Palaiseau-Cedex, France) for provided us the pm- and μc-Si:H thin film photovoltaic devices used to develop the methodologies of measurements.

I want to thank all my teachers and friends who made my stay in the PhD was a great experience and a collection of lessons that always help me be a better person.

I am very grateful to all the committee members: Dr. Andrei Sazonov (University of Waterloo, Canada), Dra. Svetlana Masurova, Dr. Alfonso Torres Jacome, Dr. Carlos Zuñiga Islas, Dr. Mario Moreno Moreno, for having examined this thesis and agreed to refereed it.

List of Acronyms

PECVD	**Plasma Enhanced Chemical Vapor Deposition**
LF-PECVD	**Low Frequency PECVD**
RF-PECVD	**Radio Frequency PECVD**
a-SiGe:H	**Amorphous Silicon-Germanium Hydrogenated**
a-Ge:H	**Amorphous Germanium Hydrogenated**
a-Si:H	**Amorphous Silicon Hydrogenated**
μc-Si:H	**Microcrystalline Silicon Hydrogenated**
pm-Si:H	**Polymorphous Silicon Hydrogenated**
ZnO	**Zinc Oxide**
LTMP	**Low Temperature Micro Probe System**
GPIB	**General Purpose Interface Bus**
sccm	**Standard Centimeter Cubic per Minute**
RF	**Radio Frequency**
DC	**Direct Current**
AC	**Alternating Current**
PV	**Photovoltaic**

List of Symbols

E_{photon}	**Photon Energy**	eV
E_u	**Urbach Energy**	eV
$E_{u_{pc}}$	**Parameter of Photoconductivity similar to E_u**	eV
q	**Elementary Electron charge**	C
λ	**Wavelength**	μm
E_{opt}	**Optical Gap**	eV
f	**Frequency**	Hz
P_{out}	**Power**	$Watts$
P	**Pressure**	$Torr$
T_s	**Temperature of the Substrate**	℃
R_{Sh}	**Shunt Resistance**	Ω
R_s	**Series Resistance**	Ω
n_d	**Diode ideality factor**	
$R_{Sh-Light}$	**Shunt Resistance under illumination**	Ω
$R_{s-Light}$	**Series Resistance under illumination**	Ω
V_{oc}	**Open Circuit Voltage**	$Volts$
I_{sc}	**Short Circuit Current**	$Ampers$
FF	**Fill Factor**	
η	**Energy-Conversion Efficiency**	$a.u.$

P_{in}	**Total Power of the Light Incident on the Device**	W/cm^2
$V_m I_m$	**Maximum Power obtained from the PV Device**	W/cm^2
I_0	**Light Beam Intensity**	W/cm^2
Q_{H_2}	**Hydrogen gas flow**	$sccm$
Q_{SiH_4}	**Silane gas flow**	$sccm$
Q_{GeH_4}	**Germane gas flow**	$sccm$
$Q_{B_2H_6}$	**Diborane gas flow**	$sccm$
Q_{PH_3}	**Phosphine gas flow**	$sccm$
Q_{PH_3}	**Phosphine gas flow**	$sccm$
Q_{Ar}	**Argon gas flow**	$sccm$
Q_{SiF_4}	**Silicon tetrafluoride gas flow**	$sccm$

Content

Chapter 1

Introduction

1.1 Background and Justification

Solar energy has been and continues to be a topic of great interest within the scientific and renewable energy because the sun is a source of clean, inexhaustible and it is free. The conversion of solar energy to electrical energy can be done in the same place of consumption without having to transport or rely on other infrastructure. The first solar cells were manufactured in the 50s, built on silicon, and since then has continued to research and develop new technologies to improve the energy conversion efficiencies and reduce manufacturing costs. This steady improvement has allowed the development, both laboratory and commercial, of a variety of photovoltaic technologies currently coexist, with different degrees of maturity.

The crystalline silicon photovoltaic technology has been and continues to be the dominant PV technology, with a current market share of over 89% and a cumulative installed capacity of over $50GW$ worldwide. It also has numerous operating facilities with more than 30 years. It is based on silicon, abundant material in the earth's crust, with well-known properties and processing technology which has been widely studied and exploited in the microelectronics industry. Within this technology encompass monocrystalline silicon, in which the starting material is a single crystal silicon and

multicrystalline silicon, formed by multiple grains, each having a different crystallographic orientation. In both cases the wafers obtained from ingots, the crystallization process consumes enormous amounts of energy and is therefore very costly, especially in the case of monocrystalline silicon. A third way, much less exploited is the silicon tape (or ribbon), which is crystallized directly into sheets from which wafers can be cut.

In contrast to wafer-based technologies, thin-film modules are done growing or depositing the semiconductor directly on a rigid or flexible substrate that will become part of the photovoltaic module. Semiconductors are used with high absorption coefficient, so that it is sufficient with a few microns of material. This allows the manufacturing process more economical, since it uses a smaller quantity of raw material, and also allow much higher levels of automation. Furthermore the energy consumption in manufacturing is much lower. Thin film technologies mainly include those based on cadmium-telluride alloys (CdTe), amorphous silicon (a-Si:H), silicon-germanium alloys (SiGe:H), and copper-indium-diselenide-gallium alloys (CIGS). There are also other thin film technologies whose level of technological maturity is lower. For example, those based on organic materials or photoelectrochemical cells.

Although the technology of thin film solar cells allows us to have lower manufacturing costs and higher levels of automation. The technology of these devices are not fully developed, and their operating mechanisms are not sufficiently understood. For this reason, in this thesis work was carried out a systematic study of the optoelectronic characteristics of silicon-germanium thin films and related photovoltaic devices in order to try to understand more precisely some of the main problems that hinder the proper operation of these devices.

The silicon-germanium thin films are of great interest for the development of photovoltaic devices because they allow us a better exploitation of the solar spectrum by means of the absorption of long wavelengths. To absorb long wavelengths with silicon-germanium alloys, it is adjusted the optical bandwidth by changing the

germanium content in the alloy. Besides that this technology is compatible with the technology of amorphous silicon solar cells and can be deposited at low temperature. In this work we studied the optoelectronic characteristics of germanium-silicon thin films with high germanium content ($\approx 97\%$) deposited by low frequency plasma at low temperatures (from $T_s = 300$ to 70℃).

The performance characteristics of the photovoltaic devices are commonly used in the state-of-art to compare and test the performance of photovoltaic devices. Unfortunately, the information provided by these features is not sufficient to understand and reveal some of the main problems that significantly affect the performance of photovoltaic devices (e.g., leakage currents, losses generated by parasitic elements, quality of junctions, etc.). In this work, we developed a set of methodologies that allow us to evaluate and study the performance of photovoltaic devices fabricated with different technologies.

1.2 **Objective and Tasks**

The objective of this work is to perform a systematic study of the optoelectronic characteristics in germanium-silicon thin films and related photovoltaic devices, including performance and diagnostic characteristics.

The systematic study will be divided into three sections:

1. The study of optoelectronic characteristics of silicon-germanium thin films which are important for photovoltaic devices.

2. The study of performance characteristics of photovoltaic devices.

3. The study of diagnostic characteristics. This section will be divided in two subsections:

a) Physics of Performance.
b) Technological Problems.

The systematic study of optoelectronic characteristics will be realized in photovoltaic devices fabricated by different laboratories:

a) Photovoltaic devices deposited by plasma at the installations of the National Institute of Astrophysics, Optics and Electronics from Mexico.
b) Photovoltaic devices deposited by plasma at the installations of the Ecole-Polytechnic from France.
c) Photovoltaic devices of organic materials manufactured at the installations of the University of Cologne from Germany.

1.2.1 **Tasks**

In order to reach the objective the following task will be solved:

- Development and implementation of methodologies utilized to obtain the optoelectronic characteristics in the thin films and photovoltaic devices based on germanium-silicon films deposited by low frequency plasma.

1) Optoelectronic characteristics of thin films which are important for photovoltaic devices will be measured:

- Measurement of optoelectronic characteristics (i.e., spectral response of sub-gap photoconductivity, $E_{u_{pc}}$ and defects ratio) in the germanium-silicon thin films. The wavelength of the incident light will be changed over a range from $hv \approx 0.8eV$ to $1.8eV$ with a change of at least 2 orders of magnitude. Optoelectronic characteristics which are important for photovoltaic devices.

2) Performance of photovoltaic devices will be characterized:

- Measurement of performance characteristics (i.e., current-voltage characteristics under illumination, open-circuit voltage, short-circuit current, fill factor and energy conversion efficiency) of the different photovoltaic devices. The performance characteristics will be measured with an accuracy that allows us to see problems related to physical mechanisms or the manufacturing technology.
- Comparison and analysis of performance characteristics (i.e., open circuit voltage, short-circuit current, fill factor and energy conversion efficiency) measured in the different photovoltaic devices to study the principal factors which affect their performance.
- Comparison and analysis of performance characteristics (i.e., open circuit voltage, short-circuit current, fill factor and energy conversion efficiency) measured in the photovoltaic devices deposited in the installations of the INAOE to study the effect of the structural configuration in the performance of the photovoltaic devices.
- Measurement of current-voltage characteristics under illumination at different operating temperatures to study how changes the performance of photovoltaic devices with the operating temperature in contrast with a crystalline photovoltaic device for example. The operation temperature will be changed from $T_p = 300K$ to $480K$ with a resolution of $\Delta T = 20K$.

3) Diagnostic characteristics related to physics of performance will be studied:

- Comparison and analysis of current-voltage characteristics measured under illumination in the photovoltaic devices deposited in the installations of the INAOE to study the effect of the structural configuration on the physical mechanisms of performance.

- Measurement of spectral response of short-circuit current in the different photovoltaic devices. The wavelength of the incident light will be changed over a range from $hv \approx 0.8eV$ to $3.8eV$ with a change of at least 2 orders of magnitude.
- Comparison and analysis between the spectral responses measured in the different photovoltaic devices to observe principal problems with the mechanisms operating.
- Comparison and analysis between the electronic characteristics obtained in the measurements of the different photovoltaic devices.
- Measurement of dark current-voltage characteristics in the different photovoltaic devices. For this study we will consider only the region with forward bias, but all the measurements will be made with both polarizations. The forward bias region should vary by at least two orders of magnitude to observe the effect of all parasitic elements.
- Comparison and analysis of dark current-voltage characteristics to monitoring the quality of the junctions by means of the diode ideality factor and saturation current.
- Measurements of dark current-voltage characteristics at different operating temperatures to monitoring the quality of the junctions in function of the operating temperature.

4) Diagnostic characteristics related to technological problems will be studied:

- Comparison and analysis of performance characteristics of photovoltaic devices deposited in the installation of the Ecole-Polytechnique to study the losses generated by the parasitic elements of photovoltaic devices (i.e., Shunt and series resistances).

- Study and analyze the behavior of the parasitic resistances measured in the photovoltaic devices fabricated at installations of the INAOE to monitor its effect on function of the structural configuration of the devices.
- Study and analyze the behavior of the parasitic resistances measured in the photovoltaic devices from the Ecole-Polytechnique in function of the operating temperature.
- Comparison and analysis of the sub-gap photocurrent to monitoring the structural disorder in function of the structural configuration of the photovoltaic devices manufactured at the installations of the INAOE.

Chapter 2

Analysis of Literature

2.1 Introduction

Thin film solar cells are a promising approach for terrestrial and space photovoltaics and offer a wide variety of choices in terms of the device design and fabrication. A variety of substrates (flexible or rigid, metal or insulator) can be used for deposition of different layers (contact, buffer, absorber, reflector, etc.) using different techniques (PVD, CVD, ECD, plasma-based, hybrid, etc.). Such versatility allows tailoring and engineering of the layers in order to improve device performance. For large-area devices required for realistic applications, thin-film device fabrication becomes complex and requires proper control over the entire process sequence. Proper understanding of thin-film deposition processes can help in achieving high-efficiency devices over large areas, as has been demonstrated commercially for different cells. Research and development in new, exotic and simple materials and devices, and innovative, but simple manufacturing processes need to be pursued in a focused manner. Which cells and which technologies will ultimately succeed commercially continue to be anybody's guess, but it would surely be determined by the simplicity of manufacturability and the cost per reliable watt. Cheap and moderately efficient of thin film solar cells are expected to receive a due commercial place under the sun [1].

In this chapter it is shown the analysis realized to the state-of-art for optoelectronic characteristics (spectral characteristics, dark and illumination current-voltage characteristics, temperature dependence of dark current-voltage characteristics, etc.) of Germanium-Silicon thin films deposited by Low Frequency Plasma Enhanced Chemical Vapor Deposition with high concentration of germanium ($x = 0.97$) and related devices.

2.2 Hydrogenated Amorphous Silicon-Germanium Thin Films

Hydrogenated amorphous silicon-germanium (a-GeSi:H) alloy thin films are potential candidates to replace the lower optical bandgap absorber layer in single-junction or multi-junction solar cells because: 1) The optical bandgap (E_{opt}) of hydrogenated amorphous silicon-germanium alloys can be easily varied (from 1.7 to $1.0eV$) to match with the long-wavelength range by changing the germanium content (a lower optical bandgap allow us a better exploitation of the solar spectrum), 2) They are compatible with amorphous silicon films deposited by plasma, and 3) The mobility of holes and electrons in germanium films is higher than in silicon films. Unfortunately, the electronic properties are deteriorate as the optical bandgap is reduced with the increase of the germanium content [2-12]. In this section the analysis of the state-of-art for the electronic properties of silicon-germanium thin films as a function of the germanium content and the deposition temperature, and the Staebler–Wronski Effect in silicon-germanium films are presented.

2.2.1 Effect of the Germanium Concentration on the Electronic Properties of the a-GeSi:H Thin Films

Currently, several groups have tried to prepared hydrogenated amorphous silicon-germanium (a-SiGe:H) alloys from a SiH_4/GeH_4 starting gas mixture by PECVD for solar cell aplicattions. Nevertheless, the quality of such prepared alloys is relatively

poor in comparison with a-Si:H thin films, since a high density of Ge dangling bonds ($> 10^{17} cm^{-3}$) due to the preferential attachment of H to Si [2]. A network structure of a thin film is principally determined by the energy relaxation process of adsorbed precursors on the growing surface of the film [2-4]. There are two main factors, which cause the low density network of a-SiGe:H film [2]. Firstly, Ge-related adsorbed radicals have smaller surface diffusion coefficient than Si-related adsorbed radicals on the growing surface. Secondly, H atoms bonding with Ge are thermally evolved at lower temperatures compared to H on Si. In other words, the optoelectronic properties of a-SiGe:H are strongly depend on the $[Ge]/[Si]$ atomic ratio. Beside that, the deposition parameters (i.e., frequency, substrate temperature, power, and pressure) are also essential in determining films properties.

2.2.1.1 **Optical band gap**

As mentioned previously, the silicon-germanium thin films are a promising candidate for photovoltaic aplications because its optical bandgap can be tailored to lower energies by adding germanium to the alloys composition. This enhances the near infrared response of the photovoltaic devices. In the silicon-germanium thin films deposited by PECVD, the germanium content can be increased by increasing the $[GeH_4]/[SiH_4]$ ratio during the deposition of the films. The studies conducted by Pratima Agarwal et al. [5] showed that the optical bandgap decreases from $E_{opt} = 1.84$ to $1.37eV$ as $[GeH_4]/[SiH_4]$ ratio increases from 0 to 1.43. As the germanium content increases in the films, less hydrogen is incorporated in the films. Further, a part of the hydrogen goes in to $Ge - H$ mode as well. The ratio of hydrogen in dihydride to monohydride mode also increases with increasing germanium content, except for highly germanium rich films, where it is low, but in these films, the hydrogen also goes in to $Ge - H_2$ mode as well. This behavior was also reported by Mursal et al. [6] as it is shown in Figure 2.1. On these films the optical bandgap decreases from $E_{opt} = 1.27$ to $1.07eV$ as the $[GeH_4]/[SiH_4]$ ratio increases from 0.036 to 0.36. The optical

bandgap does not have a linear relation to the $[GeH_4]/[SiH_4]$ ratio, because of the difference in incorporation of Si, Ge, and H into the film. The studies conducted by A. H. Mahan et al. [7] demonstrate that indeed the germanium content in solid phase increases when the $[GeH_4]/[SiH_4]$ ratio increases as it is shown in Figure 2.2. On the other hand, the hydrogen content decreases when the $[GeH_4]/[SiH_4]$ ratio increases.

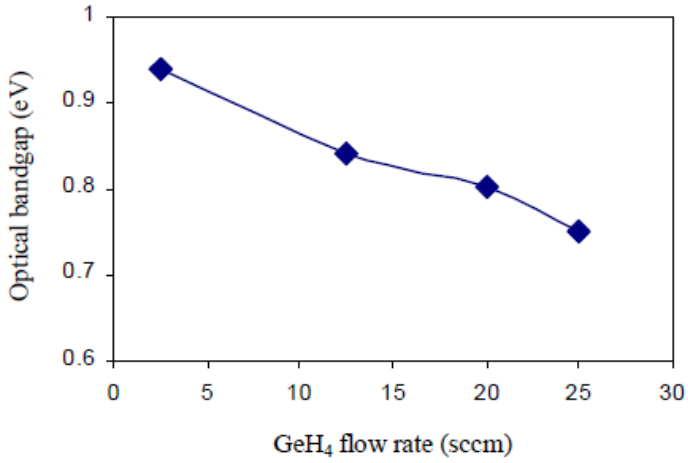

Figure 2.1: The optical bandgap of a-SiGe:H alloys films as a function of GeH_4 flow rate [6]

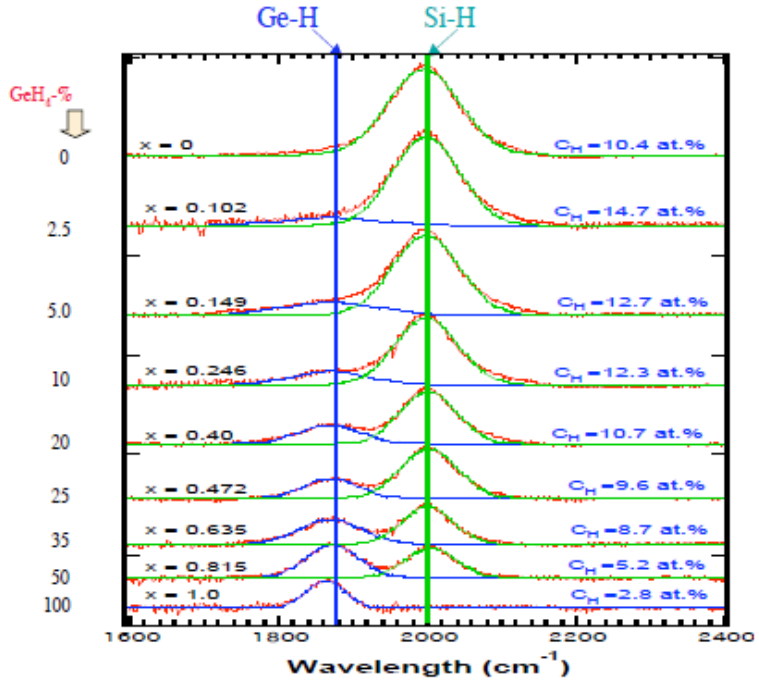

Figure 2.2: IR scans of a-SiGe:H sretch mode region for different film Ge contents [7]

In several works the influence of hydrogen on microstructure of germanium and silicon films has been studied and some recent results are mentioned in references [8-10]. On these results it was found that hydrogen bonding configurations, density fluctuations, clustered and dispersed hydrogen distributions all have an effect on the formation of voids in the films. In the PECVD these factors are controlled by a complex process related to micro particles in the plasma, ion and electron bombardments [11], density of radicals, pressure, feed gas, dilution, doping species and deposition temperature.

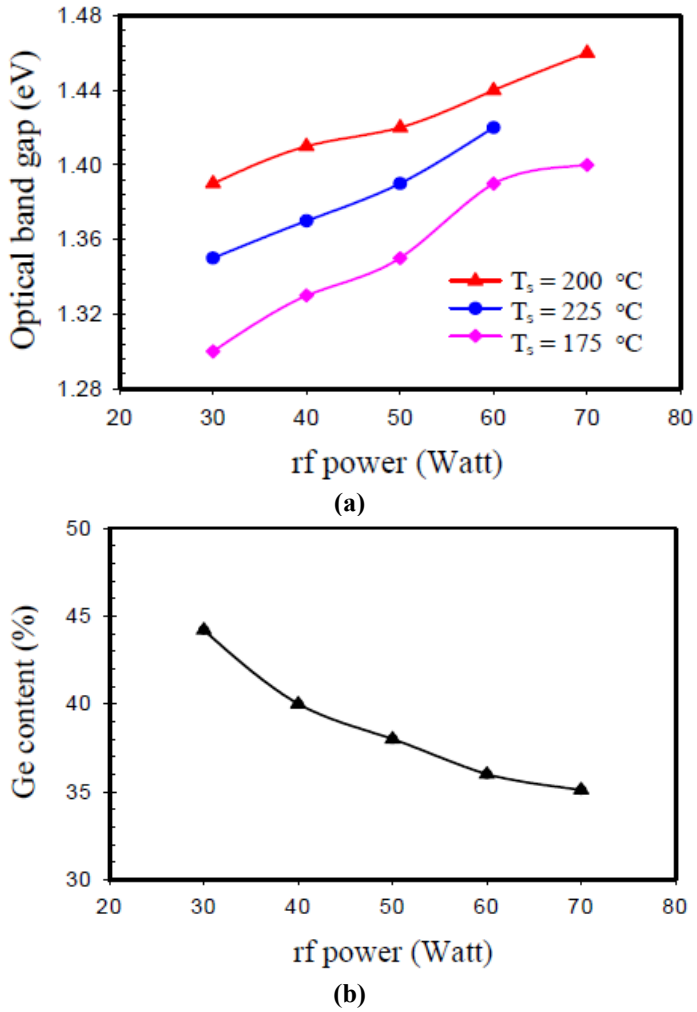

Figure 2.3: (a) The optical band gap of a-SiGe:H thin films deposited at different substrate temperature as a function of RF power and (b) Germanium content (C_{Ge}) of a-SiGe:H thin films deposited at substrate temperature of $T_d = 200$℃ as a function of RF power [12]

In more recent publications, the content of germanium in the silicon-germanium alloy was varied in function of the plasma power. Figure 2.3(a) shows the optical bandgap of a-SiGe:H thin films deposited at different substrate temperature as a function of RF power and Figure 2.3(b) shows the germanium content in solid phase in the a-SiGe:H thin films as a function of RF power. The a-SiGe:H thin films were grown on glass Corning 7059 by an RF-PECVD reactor from a gas mixture of silane (SiH_4) and germane (GeH_4) 10% diluted in hydrogen (H_2). The substrate temperature was varied from 150 to 250℃. From Figure 2.3(a) and Figure 2.3(b) we can observe that for all substrate temperatures, the optical bandgap increases with the decrease of germanium content. Mursal, S. et al. [12] declares that this behavior is due to the dissociation rate of both silane and germane is not the same; it is too sharp for silane. Therefore, the increase of RF power will decrease the relative density of germanium-related radicals in gas phase. Consequently, the germanium incorporation decreases in solid phase as shown in Figure 2.3(b). At substrate temperature of $T_d = 200℃$, the germanium content of a-SiGe:H thin films decrease from $C_{Ge} = 44.2 - 35.1\%$ with the increase of RF power from $P_{out} = 30 - 70Watt$. Thus, the dependency of E_{opt} on RF power was mainly attributed to the change in germanium content.

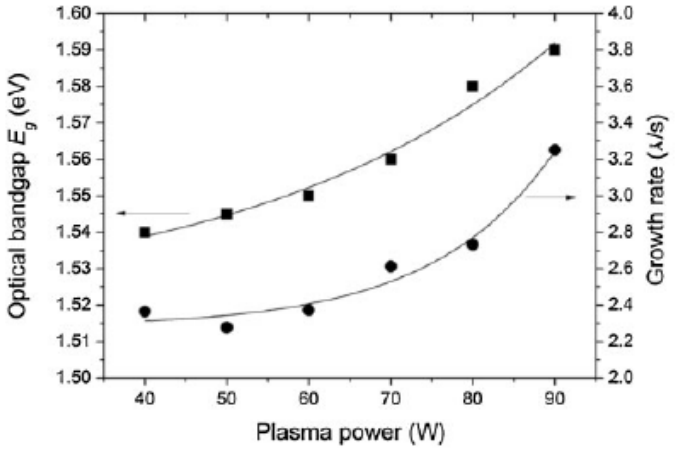

Figure 2.4: The deduced optical bandgap (Eg) and the growth rate of the above a-SiGe:H thin films. The solid lines are guides to the eye [13]

A similar behavior to the behavior observed by Mursal, S. et al. was reported by Baojun Yan et al. [13] as it is shown in Figure 2.4. The a-SiGe:H thin films prepared by Baojun Yan et al. were deposited in a multichamber 13.56-MHz PECVD reactor. During the deposition process, pure SiH_4 and 20% GeH_4 diluted by H_2 were utilized as Si and Ge sources, respectively. The deposition temperature was $T_d = 210 - 220$℃. The plasma power was varied in the range of $P_{out} = 40 - 90 Watts$ (the power density was $P_{out} = 130 - 290\, mW/cm^2$). The growth rate and optical bandgap of the a-SiGe:H thin films prepared by Baojun Yan et al. in function of the plasma power are presented in Figure 2.4. In this figure we can see that with the increase of the plasma power, the optical bandgap of the a-SiGe:H thin film increases monotonously from $E_{opt} = 1.54$ to $1.59eV$. On the other hand, the thin-film growth rate calculated by the thickness obtained via surface profiler increased from 2.3 to 3.3 $Å/s$ as the plasma power increases from $P_{out} = 40$ to $90W$. Baojun Yan et al. declare that during the a-SiGe:H deposition, Si-related and Ge-related precursors reaching the growing surface are adsorbed on the surface. Some of them diffuse on the surface and make chemical bonds at some sites forming amorphous network structure, while others desorb from the surface depending on their sticking coefficients. The increase of the plasma power increases the average energy of the electrons in the plasma and thus enhances the dissociation cross sections of silane and germane into neutral as well as ionic radicals. Besides, the increasing plasma power transfers high momentum and energy to the precursors in the growing surface, and promotes the surface diffusion of the reactive radicals. All these lead to the above growth-rate enhancement. Terakawa et al. [14] wrote that the alteration of germanium content might be affected by 1) the radical flux density ratio $[Ge\ radicals]:[Si\ radicals]:[H\ radicals]$ changes with RF power, because the decomposition efficiency of GeH_4 and SiH_4 is different from each other, 2) the incorporation probability ratio $p(Ge)/p(Si)$ depends on RF power. When RF power goes up, the time permitted for surface reaction, such as the hydrogen eliminating reaction on the growing surface become shorter, and this causes higher hydrogen content in the film.

2.2.1.2 **Absorption Coefficient**

The analysis of state-of-art presented in the previous section demonstrated that the incorporation of germanium into amorphous silicon leads to a reduction in the optical bandgap. A narrow optical bandgap enhances the absorption coefficient at longer wavelengths. By this reason, the amorphous silicon-germanium is one of the most promising thin film materials for photovoltaic, photo-detector and microelectronic applications. Figure 2.5 shows the spectral dependence of the absorption coefficient and the optical bandgap for a series of a-SiGe:H thin films deposited by Chao-ChunWang et al. [15] with different $[GeH_4]/([SiH_4]+[GeH_4])$ ratio. The SiGe films were deposited on glass using high-frequency ($27.12MHz$) plasma-enhanced chemical vapor deposition ($HF-PECVD$) in an ultrahigh-vacuum, single-chamber, loadlocked deposition system. The results obtained by Chao-ChunWang et al. show that the absorption coefficient increases from about $9x10^4$ to $13x10^4 cm^{-1}$ when the $[GeH_4]/([SiH_4]+[GeH_4])$ ratio increases to above 80%. In addition, the absorption edge of the SiGe film is shifted to long wavelength mainly due to a decrease in Tauc energy bandgap.

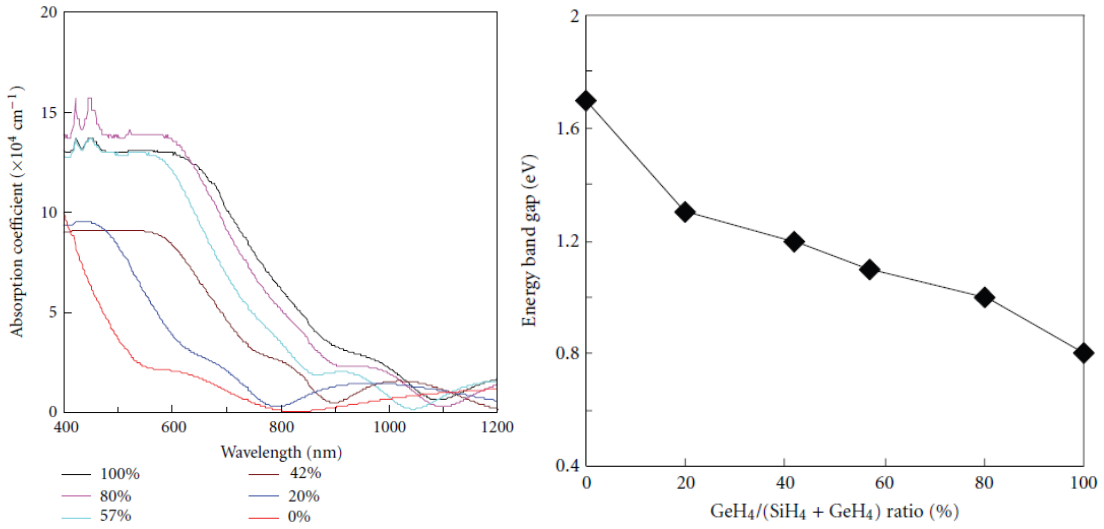

Figure 2.5: The spectral dependence of the absorption coefficient and the optical band gap for the SiGe films with different gas ratios [15]

Similar result has been observed by Gopal G. et al. [16] on a-SiGe film as it is shown in Figure 2.6. This Figure shows the calculated absorption coefficient of the $Si_{1-x}Ge_x$ film with $x = 0.22, 0.48$ and 0.94. Also it shows a comparison between the absorption coefficient of a-Si (solid circle) and $Si_{0.52}Ge_{0.48}$ (open circle) at $700nm$. It clearly shows that Ge incorporation systematically increases the absorption coefficient of the film. The absorption coefficient of a-SiGe is more than one order of magniture higher than a-Si film at $700nm$. As the Ge fraction increases, photosensitivity of a-SiGe film extends into IR band of solar spectrum.

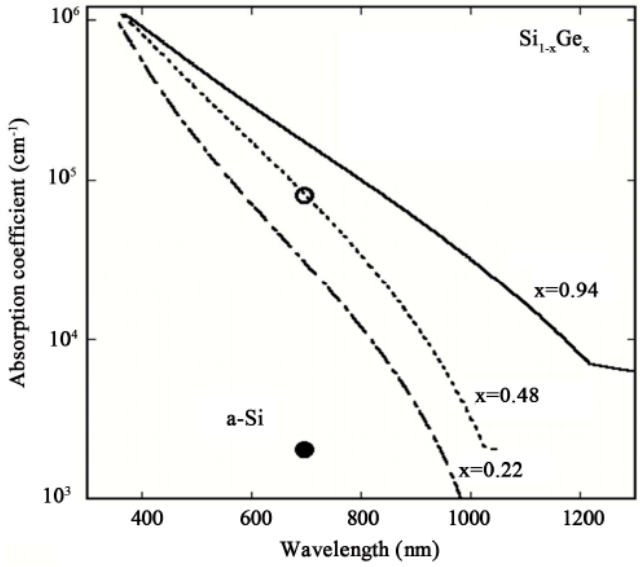

Figure 2.6: Absorption coefficient spectra of a-$Si_{1-x}Ge_x$ thin films with x = 0.22, 0.48 and 0.94. Absorption coefficient of a-Si (solid circle) is compared with a-$Si_{0.52}Ge_{0.48}$ (open circle) at wavelength 700nm. Ge incorporation increases the absorption coefficient and extends its photosensitivity towards longer wavelengths [16]

The absorption coefficient and the thickness of the intrinsic film are key parameters that can limit the performance of amorphous thin film p-i-n solar cells. For example, in amorphous thin film p-i-n solar cell a thick intrinsic film can absorb more light to generate carriers. Unfortunately, a thicker intrinsic film degrades the drift electric field for carrier transport. On the other hand, a thin intrinsic film cannot absorb enough light. In order to avoid drastic reduction of the short circuit current (J_{sc}) in a solar cell with small thickness, it is necessary to increase absorbance of the intrinsic film and optimize

the cell structure. Using a lower bandgap material such as a-SiGe.H in the active base region of the cell is a possible approach, owing to its compatibility with the mature Si-based cell process. An appreciable increase of photocurrent (J_{sc}) in the small optical bandgap a-SiGe:H material is highly expected, because of the increased absorption of photons.

2.2.1.3 **Density of deep defects**

Figure 2.7 shows the mobility-lifetime ($\eta\mu\tau$) product versus generation rate of majority carriers calculated from the photoconductivity (σ_{ph}) measurements for a-SiGe:H samples with varying germanium concentrations from 0 to 62%. The thin films of a-SiGe:H were deposited by M. Gunes et al. [17] by using Plasma Enhanced Chemical Vapor Deposition (PECVD) technique at a standard frequency of $f = 13.56MHz$ on glass substrates using $Si_2H_6 + GeH_4 + H_2$ gas mixture.

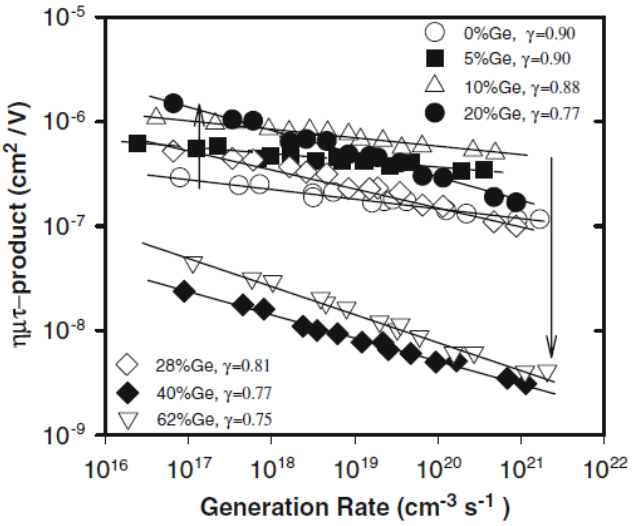

Figure 2.7: ημτ-Products versus generation rate of a-SiGe:H alloys with Ge content from 0 to 62% in the annealed state [17]

From Figure 2.7 we can see that the density of deep defects in the bandgap increases with increased germanium alloying which finally degrades photosensivity. For all the germanium concentrations, $\eta\mu\tau$-products exhibit the expected linear relation as a

function of generation rate. As the germanium content changes from 0% (pure a-Si:H) to 10%, the magnitude of $\eta\mu\tau$-products increase and the exponent γ stays around 0.90. Further increase in germanium concentration results in a decrease in photosensitivity. The photosensitivity of the a-SiGe:H thin films drops considerably when the germanium concentration increases from 40 to 62%. The exponent γ begins to decrease below 0.90. M. Gunes et al. declare that this behavior indicate that there exists a substantial change in the density and nature of native defects states present in the optical bandgap of the a-SiGe:H alloys as germanium concentration increases above 28%.

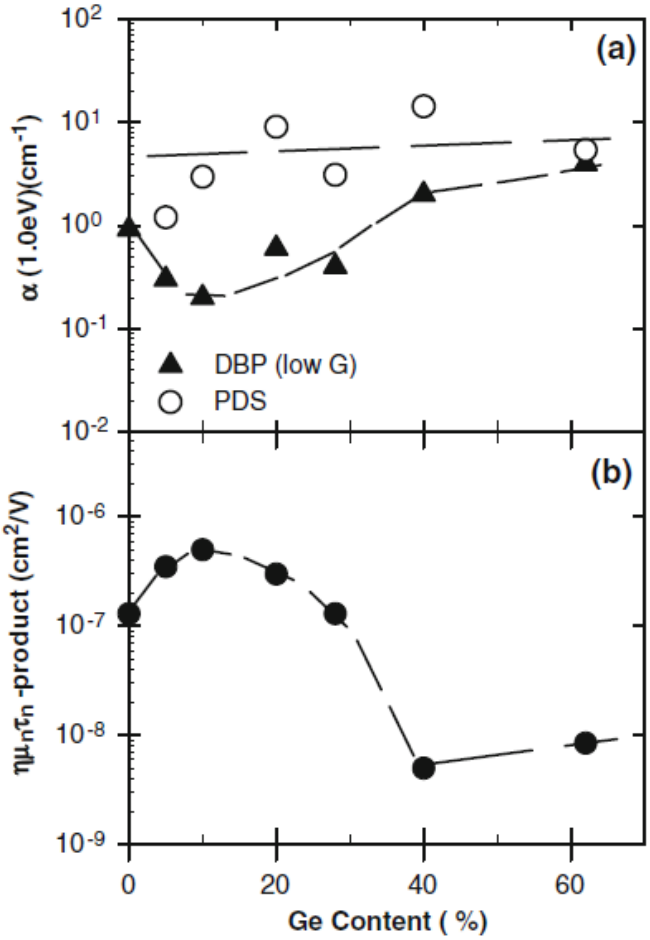

Figure 2.8: a) Sub-bandgap absorption coefficient at 1.0 eV versus Ge concentration obtained from PDS and DBP methods, b) ημτ-products measured at G = 1020 cm^{-3} s^{-1} versus Ge content in the annealed state. Lines are guide to eyes [17]

In order to compare the level of the density of defect states present in the a-SiGe:H thin films, M. Gunes et al. took the absorption coefficient at 1.0eV, $\alpha(1.0eV)$, as it is shown in Figure 2.8. In Figure 2.8(a) we can see that the $\alpha(1.0eV)$ measured using dual beam photoconductivity low generation rate decreases as germanium concentration increases from 0 to 10%. The alloy with 10% germanium content has the lowest $\alpha(1.0eV)$ which indicates the lowest defect density. This result is consistent with the highest $\eta\mu\tau$-products of the 10% germanium sample shown in Figure 2.8(b). Further increase in germanium content results in an increase in the defect states as $\alpha(1.0eV)$ increases. It causes more recombination and degrades the $\eta\mu\tau$-products as given in Figure 2.8(b). $\eta\mu\tau$-products decreases substantially for samples above 28% germanium concentration points out that there could be an important change in the nature of the defect states in the high germanium content alloys. In Figure 2.8(a) and Figure 2.8(b) we can see that there is a good agreement between the changes in $\alpha(1.0eV)$ obtained from dual beam photoconductivity low bias light and the changes in $\eta\mu\tau$-products as germanium concentration changes. However, such distinct functional dependence of $\alpha(1.0eV)$ cannot be seen from the photothermal deflection spectroscopy measurement as indicated in Figure 2.8.

2.2.2 Effect of Temperature Deposition Reduction on the Electronic Properties of the a-GeSi:H Thin Films

Although, the optoelectronic properties of a-SiGe:H is strongly dependent on the germanium content (see from Figure 2.3 to Figure 2.8), the deposition parameters such as substrate temperature and the deposition rate are also essential in determining hydrogen content and film properties. Figure 2.9 shows the absorption spectra for a series of the a-SiGe:H thin films deposited by Mursal et al. [18] at different substrate temperature. In Figure 2.9, the absorption edges of the a-SiGe:H thin films are observed to shift smoothly to higher photon energy and the sub bandgap absorption decreases with an increase in substrate temperature from 150 to 200℃.

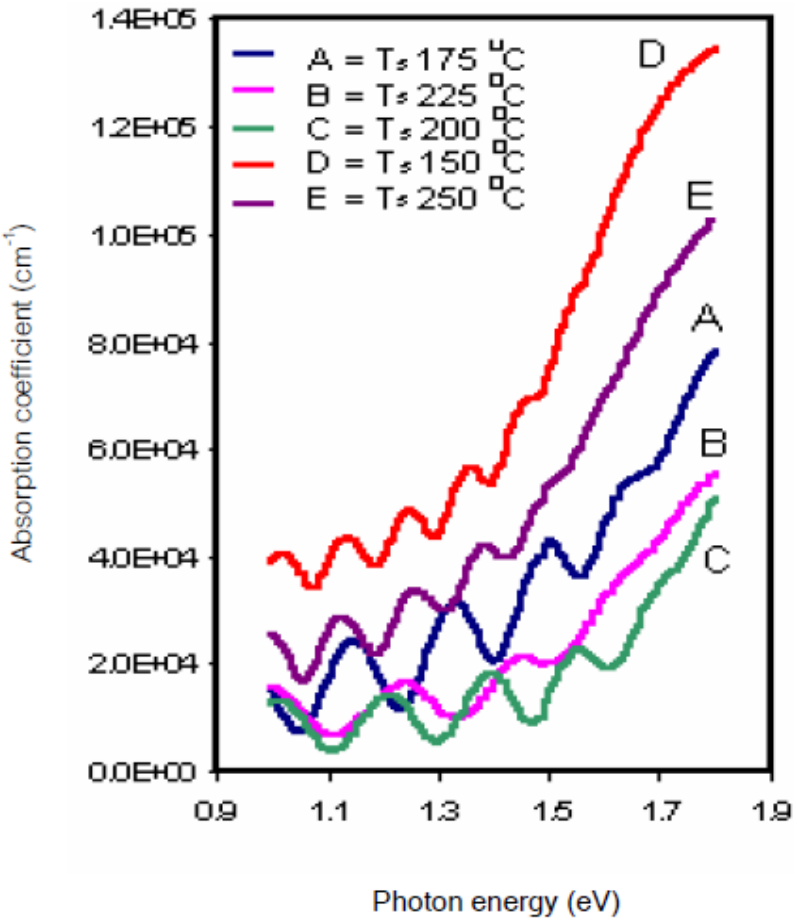

Figure 2.9: The absorption coefficient curve for a series of the a-SiGe:H films deposited at various substrate temperature [18]

For the films deposited at the substrate temperature from 200 to 250℃, the absorption edges shift smoothly to lower photon energy and the sub bandgap absorption increases. The optical band gap (E_{opt}) of the a-SiGe:H thin films deposited by Mursal et al. increased from $1.20eV$ to $1.39eV$ when the substrate temperature increased from 150 to 200℃ and decrease to $1.26eV$ at the substrate temperature of 250℃ as shown in Figure 2.10. Mursal et al. wrote that the E_{opt} of a-SiGe:H thin films does not have a linear relation to substrate temperature, because of the difference in incorporation of Si, Ge, and H atoms into the films. The increase in the E_{opt} at substrate temperature of 200℃ is probably due to decreasing germanium content or increasing hydrogen content.

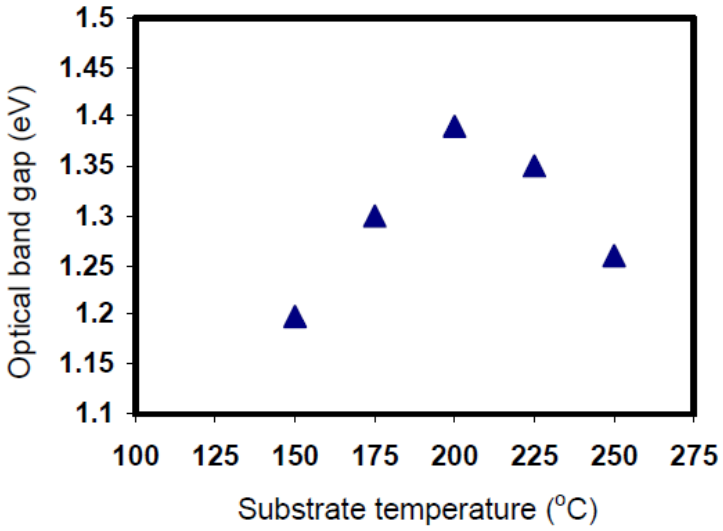

Figure 2.10: The optical band gap of the a-SiGe:H thin films as a function of the substrate temperature [18]

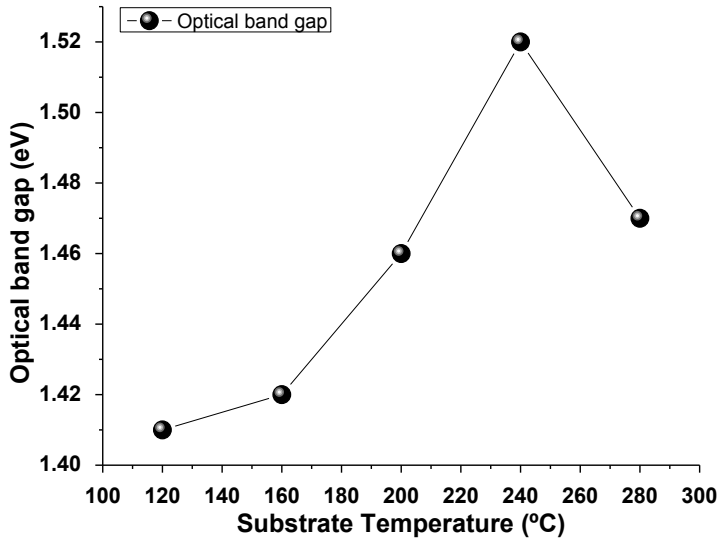

Figure 2.11: Optical band gap of silicon-germanium thin films [19]

This behavior (see Figure 2.11) was also reported by Long Gu et al. [19]. From the trend observed by Long Gu et al. it could be inferred that with the temperature increased, the optical bandgap increased first and then decreased. As the temperature decreased from 250 to 120℃, the optical bandgap decreased from $E_{opt} = 1.52$ to $1.41eV$. When the temperature was higher than 240℃, with the temperature increasing, the optical band gap became narrower. Lower the temperature would do

some help to make the optical band gap narrower, which is very useful in a-Si/a-SiGe/a-SiGe stacked solar cells. Moreover, the photosensitivity of the a-SiGe:H thin films increased first then decreased as it is shown in Figure 2.12. At the temperature deposition of 160℃, photosensitivity is the biggest.

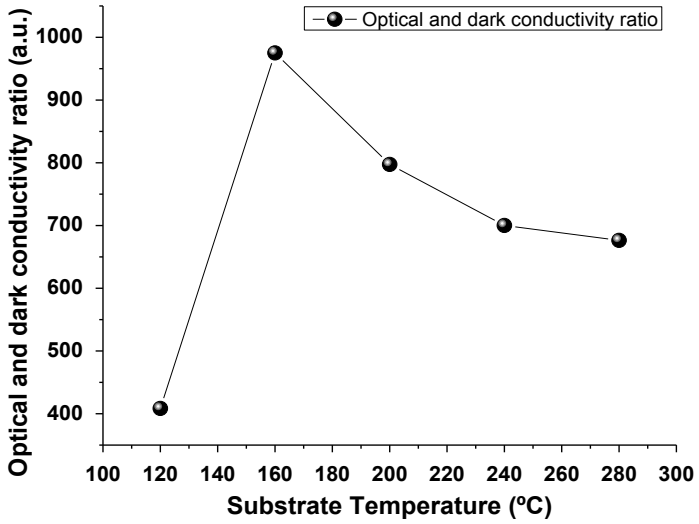

Figure 2.12: Photosensitivity of the a-SiGe:H thin films as a function of the substrate temperature [19]

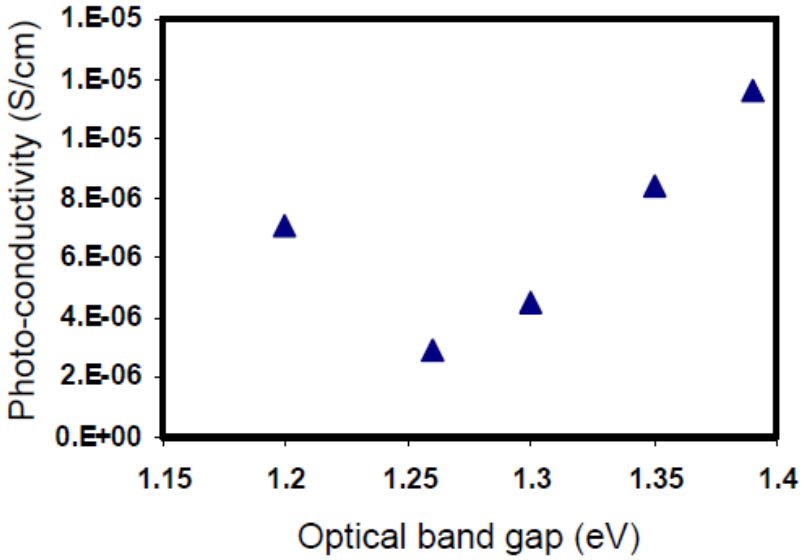

Figure 2.13: Photoconductivity of the a-SiGe:H thin films as a function of the optical bandgap [18]

Mursal et al. [18] did not report the photosensitivity of a-SiGe:H thin films as a function of substrate temperature as Long Gu et al. reported. Mursal et al. reported the photoconductivity of a-SiGe:H thin films as a function of deposition temperature as it is shown in Figure 2.13. In these results the highest photoconductivity was obtained at the wider E_{opt}, where the wider E_{opt} has a strong correlation with the lowest germanium content. The improvement of photoconductivity might be due to a low defect density in the material. Results shown in Figure 2.10 and Figure 2.13 demonstrated that the photosensitivity and the optical band gap are the biggest at the temperature deposition of 200℃. This temperature deposition is slightly higher than the one reported by Long Gu et al. in Figure 2.12.

2.2.3 **Staebler-Wronski Effect in a-GeSi:H Thin Films**

In the last thirty years, various groups have work extensively to obtain a fundamental understanding of light-induced degradation and also to develop materials and devices that are resistant to this degradation process [17, 20-23]. The observation of metastable changes in a-Si:H goes back to the work of Staebler and Wronski [20]. Staebler and Wronski found in 1977 that the dark conductivity and photoconductivity of glow-discharge deposited amorphous silicon can be reduced significantly by prolonged illumination with intense light. The observed changes were found to be reversible by annealing of the a-Si:H samples at elevated temperatures (≥ 150℃), and were attributed to a reversible increase in density of gap states acting as recombination centres for photoexcited carriers and leading to a shift of the dark Fermi level E_F toward midgap. Since this first report, light-induced metastable changes in the properties of hydrogenated amorphous silicon are referred to as the Staebler-Wronski effect (SWE).

Staebler–Wronski effect is an intrinsic property of hydrogenated amorphous silicon thin films. Nevertheless, a-SiGe:H alloys also exhibit a similar Staebler–Wronski effect when they are exposed to sun light as it is shown in Figure 2.15. The steady-state defect density (N_s) of a-SiGe:H alloys is determined by a balance among the following four

processes: light-induced creation (LIC), light-induced annealing (LIA), thermally induced creation (TIC), and thermally induced annealing (TIA) [24, 25]. Thus, to design stable a-SiGe:H alloys, not only the light-induced processes but also the thermally induced processes should be understood. Furthermore, the cell stability and N_s also depend on the operating temperature, because the recovery process is thermally activated as it is shown in Figure 2.14. Figure 2.14 shows the normalized defect density (N/N_{BA}) of a-SiGe:H i-layers deposited by Akira Terakawa et al. [26] ($E_{opt} = 1.32 - 1.58eV$) during annealing at 70 to 150℃ in air.

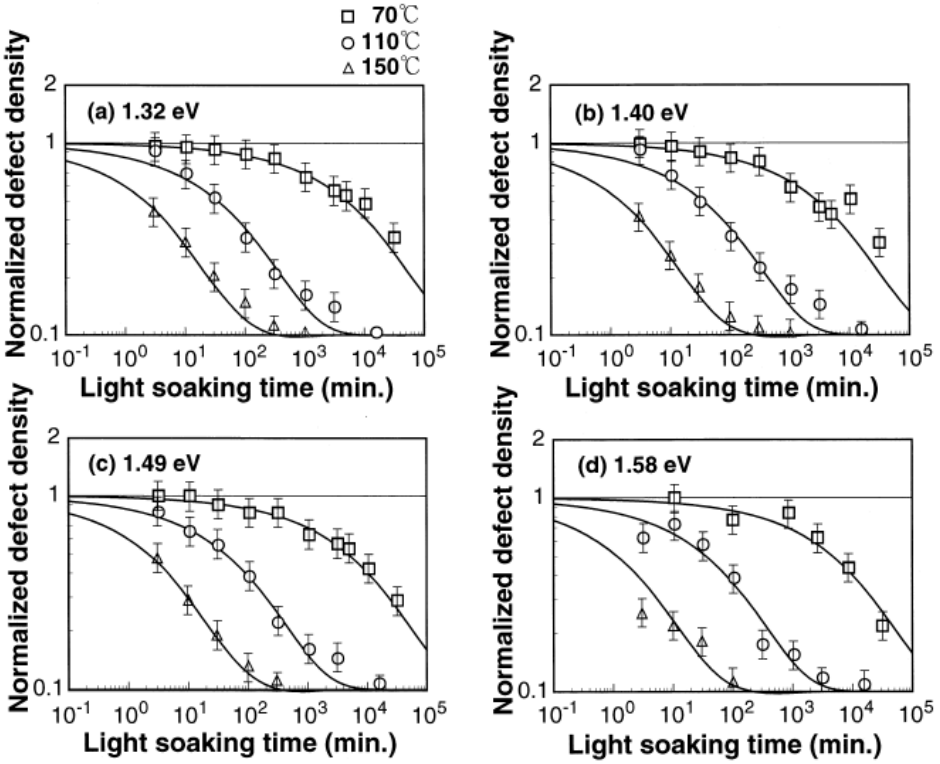

Figure 2.14: The normal defect density (N/NBA) of a-SiGe:H, evaluated from the recovery in the conversion efficiency of solar cells, during annealing at 70–150ºC in air. i-layers Eopt; a) 1.32 eV, b) 1.40 eV, c) 1.49 eV, d) 1.58 eV [26]

In Figure 2.14 we can see that the saturated defect density (N_s) of the smaller E_{opt} alloys exhibit a greater temperature dependence than that of the wider E_{opt} alloys because of the E_{opt} dependence of the LIC process and the independence of the TIA process. Results obtained by Akira Terakawa et al. demonstrate that although a-SiGe:H

alloys have considerable potential for improving the initial conversion efficiency, a-SiGe cells have unfortunately shown relatively large degradation. However, it was suggested that solar cells with a-SiGe:H offer a greater advantage in operation at high temperature than cells with a-Si:H. The operating conditions should thus be considered in the design of high-efficiency solar cell submodules. A similar behaviour was reported by M. Gunes et al. [17] as it is shown in Figure 2.15. In the inset of Figure 2.15, steady-state photoconductivity versus generation rate measured after different light soaking periods is presented for the a-SiGe:H alloy with 20% germanium concentration.

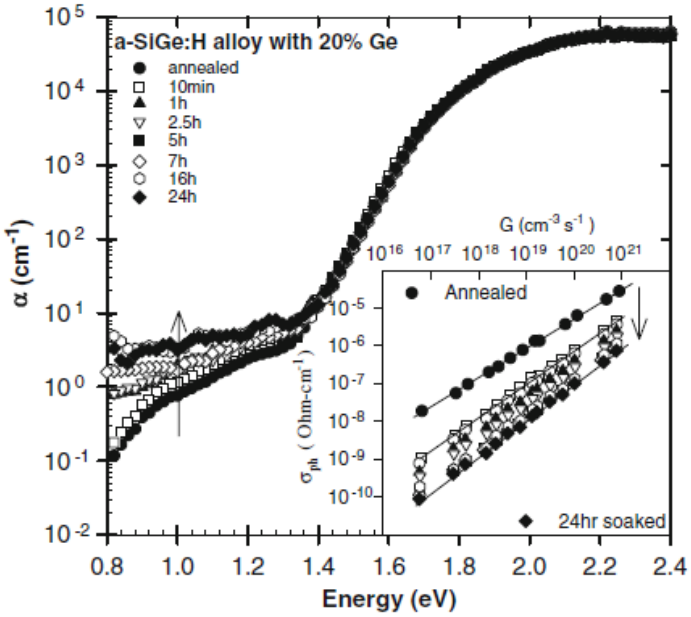

Figure 2.15: The changes in the sub-bandgap absorption coefficient spectra with extended light soaking for the a-SiGe:H alloy with 20% Ge. In the inset corresponding steady-state photoconductivity versus generation rate data is shown for different periods of light soaking [17]

From the inset of Figure 2.15 we can see that the magnitude of σ_{ph} decreases more than two orders of magnitude when sample reached to stabilized steady-state and the exponent γ increases from its annealed state value to 0.85. M. Gunes et al. declare that a similar degradation kinetics were also obtained for other a-SiGe:H alloy thin films as germanium content changes from 0 to 28%. However, degradation becomes less

significant for samples with 40 and 62% germanium concentration. Degradation of σ_{ph} seen in the inset of Figure 2.15 is attributed to the creation of light induced defect states in the optical bandgap of a-SiGe:H alloy, which decrease the majority carrier lifetime through increased recombination kinetics.

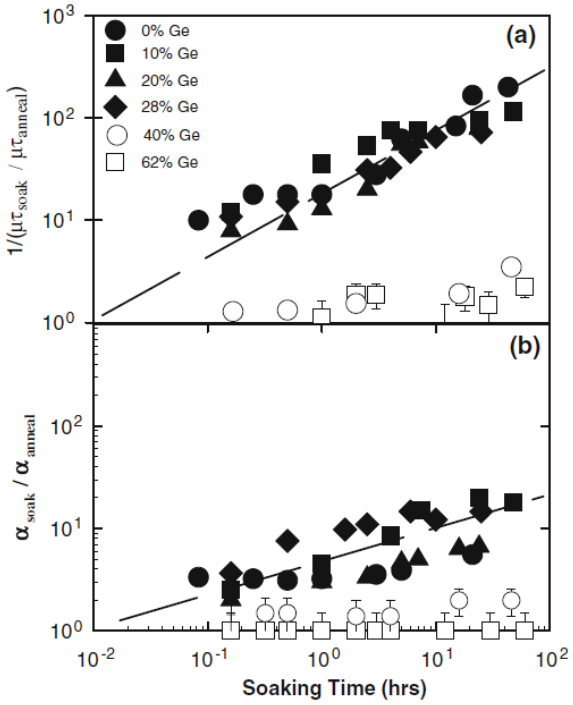

Figure 2.16: a) $1/(\mu\tau_{soak}/\mu\tau_{anneal})$ versus soaking time, b) $\alpha_{soak}/\alpha_{anneal}$ versus soaking time for the a-SiGe:H alloys with Ge concentration from 0 to 62% [17]

Similar experimental results have been obtained by M. Gunes et al. for the degradation of photoconductivity and the changes in the sub-bandgap absorption coefficients for other a-SiGe:H alloy thin films as it is shown in Figure 2.16. Both parameters are equal to unity in the annealed state and increase as light soaking time increases. In Figure 2.16 an approximate solid line in each figure was drawn for a guide to eye, which also points the annealed state values of both parameters. M. Gunes et al. declare that the changes in both parameters are due to creation of new light induced defect states which affect directly both experimental steady-state photoconductivity and sub-band gap absorption measurements. In Figure 2.16 we can see that the

degradation of a-SiGe:H alloys with germanium concentration from 0% to 28% exhibit similar functional dependence on time for both parameters. Nevertheless, a-SiGe:H alloys with 40 and 62% germanium concentration do not show a significant degradation in both parameters. An important difference between these two figures is that the slope of $[\mu\tau_{soak}/\mu\tau_{anneal}]^{-1}$ is approximately two times higher than that of $[\alpha(1.0eV)_{soak}/\alpha(1.0eV)_{anneal}]$, which indicates that the defects causing the degradation of $\eta\mu\tau$-products and increase of sub-bandgap absorption coefficient, $\alpha(1.0eV)$, are not the same type of defects. These results indicate that the degradation kinetics in a-Si:H and a-SiGe:H alloys with germanium concentration up to 28% are similar in nature. However, detailed nature of defect creation in these alloys, especially the ratio of native silicon and germanium related defects and the ratio of light induced creation of silicon and germanium related defects in a-SiGe:H alloys with different germanium concentrations, cannot be directly understood from these results alone. Insignificant degradation kinetics of high germanium concentration alloys were also reported in previous investigations [27-29].

2.3 **Performance Characteristics**

The performance characteristics (open circuit voltage, short-circuit current, fill factor and power conversion efficiency) are a very useful tool for the development and manufacture of solar cells. Since this tool will provide comprehensive information about the performance of photovoltaic devices and also allows us to compare the performance of our devices with the operation of the devices manufactured around the world. However, the performance characteristics do not provide information about the physical mechanisms that govern the operation of photovoltaic devices and technological issues that affect the proper operation thereof (i.e., quality of the junctions, quality of the intrinsic film, metal-semiconductor contanct, density of the defect states, surface recombination, leakage current, etc.). Currently, there are several electric models and measurement methodologies that allow us to obtain more detailed

information about the performance and technological issues of photovoltaic devices. Figure 2.17 presents the equivalent diagram (model) of photovoltaic devices used in this thesis work to study the performance characteristics of a p-i-n solar cell. The model consists of a series resistance, R_s[1], shunt resistance, R_{Sh}[1], a source of photogenerated current, I_{ph}, and an ideal diode, I_d. R_L represents the load resistance. The model is commonly used for performance analysis of photovoltaic devices.

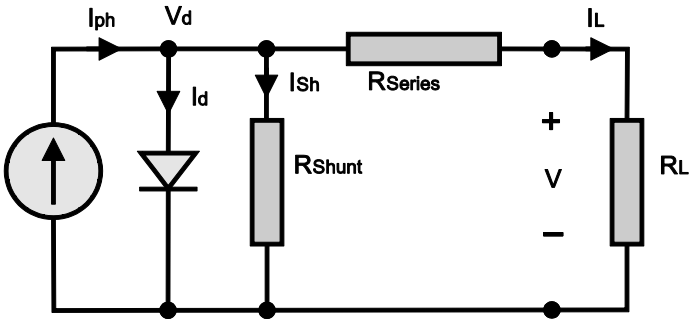

Figure 2.17: Basic electrical model used to represent the photovoltaic properties of p-i-n structures

The equation used to describe the behavior of the current-voltage characteristics of the electrical model shown in Figure 2.17 is:

$$I_L = I_{ph} - I_0 \exp\left[\frac{q\left(V - I_L R_s\right)}{nkT}\right] - \frac{V + I_L R_s}{R_{Sh}} \qquad [2.1]$$

Where I_{ph} represents the current photogenerated within the device, I_L and V represents the current and voltage provide to the load resistance. By varying the value of the load resistance we can change the operating point of the solar cell as shown in Figure 2.18. If the value of the load resistance is zero, the current delivered by the device obtains its highest value and it is ideally equals to the value of the current

[1] In general, the elements denoted as R_s and R_{Sh} are not resistances and can be described as two elements with dependence of $I \sim V^{\beta}$ (where β is a factor different for R_s and R_{Sh})

photogenerated within the device. Under conditions of zero load resistance, the power supplied by the device is zero since the voltage provided by the device to the load resistance is zero. At this operating point the current provided by the device is referred as the short-circuit current (I_{sc}). If we increase the value of the load resistance, the current provided by the device slightly decreases and the voltage provided by the device begins to increase until reach the point named as effective load resistance (operating point marked as the fill factor point in Figure 2.18). Under these conditions of load resistance the power provided by the device obtains its highest value. The current provided by the device is less than the short circuit current and voltage provided for the device has not obtained its highest value. At this operating point the characteristic named fill factor (FF) and power conversion efficiency (η) have obtained their highest value. If we continue increasing the value of the load resistance to infinity, the voltage provided by the device increases to the operating point named open-circuit voltage (V_{oc}). At this operating point the voltage provided by the device obtains its maximum value and the power delivered by the device is zero because the current provided by the device reduces to zero.

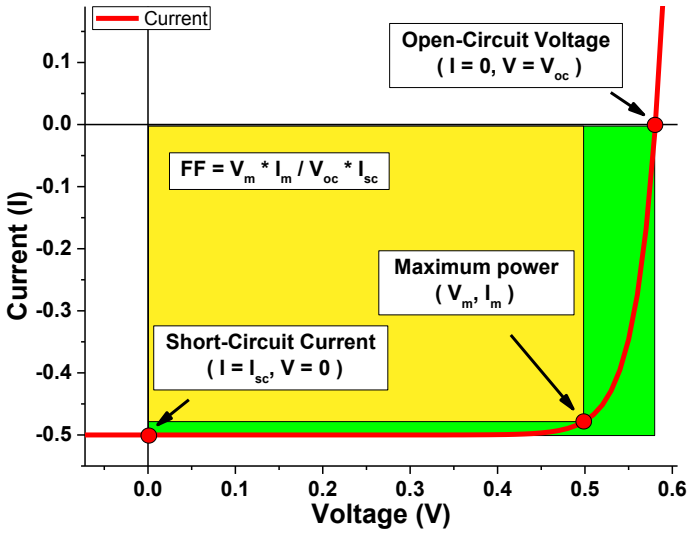

Figure 2.18: Load Current-voltage characteristics under illumination showing the short circuit current, open circuit voltage and fill factor

In Figure 2.17 and Figure 2.18 we can see that the performance of the solar cell drastically depend on the quality and value of all its elements. That is, if the value of the shunt resistance is small the current provided by the device reduces. If the value of the series resistance is high, the voltage provided by the device also reduces. If the quality of the junctions of the diode are not adequate the performance of the device also reduces. Therefore, it is necessary to optimize the quality and value of all its elements. Unfortunately, this task is not easy since each element depends on many physical mechanisms of operation or problems related to manufacturing technology as it is explained more detailed in the following sections.

2.3.1 **Short-Circuit Current**

The short-circuit current, usually written as I_{sc}, is the electric current supplied by the solar cell under short-circuit conditions (i.e., when the value of the load resistance is zero). Under short-circuit conditions, the voltage available from the solar cell is zero and the electric current obtains its highest value as it is shown in Figure 2.18. Therefore, the short-circuit current is the largest current which may be drawn from the solar cell. The short-circuit current is due to the generation and collection of light-generated carriers. For an ideal solar cell at most moderate resistive loss mechanisms or without resistive loss mechanisms, the short-circuit current and the light-generated current are identical. The short-circuit current depends on a number of factors which are enumetared below:

1. The spectrum of the incident light. For most solar cell measurement, the spectrum is standardized to the AM1.5 spectrum.
2. The optical properties (absorption and reflection) of the solar cell.
3. The number of photons (i.e., the power of the incident light source). The short-circuit current (I_{sc}) from a solar cell is directly dependent on the light intensity.
4. The collection probability of the solar cell, which depends chiefly on the surface passivation and the minority carrier lifetime in the base.

5. The optical band gap, in an ideal device every photon above the optical band gap gives one charge carrier in the external circuit so the highest current is for the lowest optical band gap.
6. The operation temperature. In terrestrial applications, the operation temperature can change over a range from 0 to 50℃.
7. The area of the solar cell. To remove the dependence of the solar cell area, it is more common to list the short-circuit current density (J_{sc} in mA/cm^2) rather than the short-circuit current.

2.3.2 **Open-Circuit Voltage**

The open-circuit voltage, usually written as V_{oc}, is the maximum voltage available from a solar cell under open-circuit conditions (i.e., when the value of the load resistance is infinite). Under open-circuit conditions, the electric current supplied by the solar cell is zero as it is shown in Figure 2.18. The open-circuit voltage corresponds to the amount of forward bias on the solar cell due to the bias of the solar cell junction with the light-generated current. Neglecting Shunt current which was shown in Figure 2.17, the open-circuit voltage depends on the saturation current of the solar cell and the light-generated current as it is shown in Equation (2.2).

$$V_{OC} = \frac{nkT}{q} \ln\left(\frac{I_{ph}}{I_0} + 1\right) \qquad [2.2]$$

While I_{ph} typically has a small variation, the key effect is the saturation current, since this may vary by orders of magnitude. The saturation current (I_0) depends on recombination in the solar cell. Open-circuit voltage is then a measure of the amount of recombination in the device. The short-circuit current (I_{sc}) decreases with increasing optical band gap but the open-circuit voltage increases as the optical band gap increases.

2.3.3 **Fill Factor**

As mentioned previously, the short-circuit current and the open-circuit voltage are the maximum current and voltage respectively from a solar cell. However, at both of these operating points, the power from the solar cell is zero. The fill factor, usually written as FF, is a parameter which, in conjunction with V_{oc} and I_{sc}, determines the maximum power from a solar cell. The fill factor is defined as the ratio of the maximum power from the solar cell to the product of V_{oc} and I_{sc}. Graphically, the fill factor is a measure of the "squareness" of the solar cell and is also the area of the largest rectangle which will fit in the current-voltage curve as it is shown in Figure 2.18. In practice the fill factor will be lower due to the presence of parasitic resistive losses.

2.3.4 **Efficiency**

The efficiency is the most commonly used parameter to compare the performance of one solar cell to another. Efficiency is defined as the ratio of energy output from the solar cell to input energy from the sun. In addition to reflecting the performance of the solar cell itself, the efficiency depends on the spectrum and intensity of the incident sunlight and the temperature of the solar cell. Therefore, conditions under which efficiency is measured must be carefully controlled in order to compare the performance of one device to another. The efficiency of a solar cell is determined as the fraction of incident power which is converted to electricity and is defined as:

$$\eta = \frac{V_{oc} I_{sc} FF}{P_{in}} \qquad [2.3]$$

Where V_{oc} is the open-circuit voltage; I_{sc} is the short-circuit current; FF is the fill factor; and P_{in} is the input energy of the sun. Equation (2.3) assumes that the photon impingememt are and the area generating the current are the same. For solar cells collecting light over a larger area than generating the current (i.e., for concentrator solar cells), this expression is remplaced by:

$$\eta = \frac{A_S}{A_C}\frac{V_{oc} I_{sc} FF}{P_{in}} \qquad [2.4]$$

Where A_s is the solar cell area generating current and A_c is the area collecting the photons. The advantage of a concentrator configuration lies in its being able to harvest more incoming solar power with a given cell size.

2.3.5 **Series Resistance**

Resistive effects in solar cells reduce the efficiency of the solar cell by dissipating power in the resistances. The most common parasitic resistances are series resistance and shunt resistance. The key impact of parasitic resistance is to reduce the fill factor. Both the magnitude and impact of series and shunt resistance depend on the geometry of the solar cell, at the operating point of the solar cell. Series resistance in a solar cell has three causes: firstly, the movement of current through the emitter and base of the solar cell; secondly, the contact resistance between the metal contact and the semiconductor; and finally the resistance of the top and rear metal contacts.

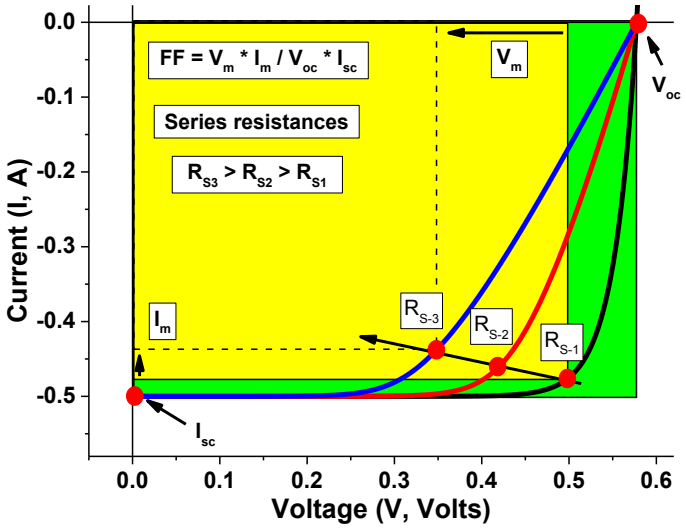

Figure 2.19: The effect of series resistance on fill factor. The short-circuit current (I_{SC}) is unaffected by the series resistance until it is very large

The main impact of series resistance is to reduce the fill factor as it is shown in Figure 2.19, although excessively high values may also reduce the short-circuit current. Series resistance does not affect the solar cell at open-circuit voltage since the overall current flow through the solar cell, and therefore through the series resistance is zero. However, near the open-circuit voltage, the current-voltage characteristic is strongly affected by the series resistance.

2.3.6 **Shunt leakage Current (Shunt Resistances)**

Significant power losses caused by the presence of a shunt resistance are typically due to manufacturing defects, rather than poor solar cell design. Low shunt resistance causes power losses in solar cells by providing an alternate current path (shunt leakage current) for the light-generated current. Such a diversion reduces the amount of current flowing through the solar cell junction and reduces the voltage from the solar cell as it is shown in Figure 2.20. The effect of a shunt resistance is particularly severe at low light levels, since there will be less light-generated current. The loss of this current to the shunt therefore has a larger impact. In addition, at lower voltages where the effective resistance of the solar cell is high, the impact of a resistance in parallel is large.

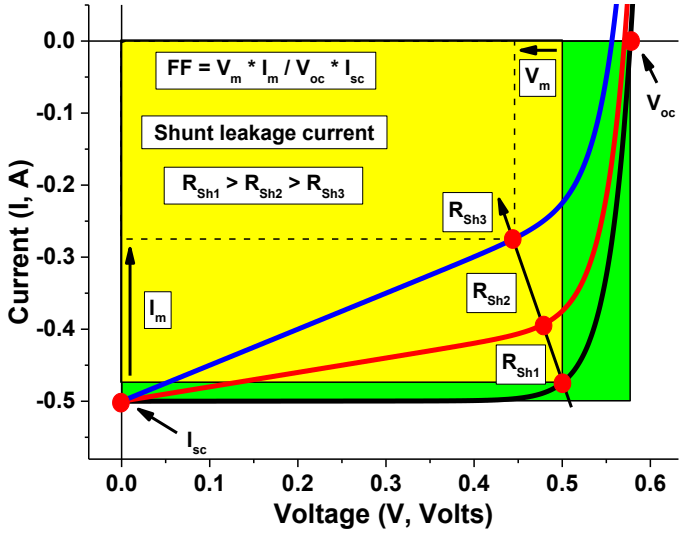

Figure 2.20: The effect of shunt resistance on fill factor in a solar cell

In the literature there is considerable evidence from thermography [30, 31] and luminescence [32] experiments demonstrating the localized nature of dark current conduction. Moreover, this localized conduction has also been correlated with the random shunt currents in the solar cell [32]. These localized shunts arise primarily because in these cells, thin films of material ($\approx 100nm$) must be deposited over large areas ($\approx cm^2$) using low temperature processes. This means that any small variation in substrate surface, dust particles, or any other small localized materials property fluctuation can create possible shunt paths at those locations. Despite these similarities in electrical characteristics, the exact nature of shunt path responsible for a shunt leakage current is expected to be quite different in each PV technology, depending on the cell structure and the materials used. For example, for a-Si:H p-i-n solar cells the p and n layers are only $\approx 10nm$ thick each. This means that substrate roughness, local doping inhomogeneities, or metal/contact material diffusion into a-Si:H can create a structure which might result in a shunt leakage current. The most likely way such a shunt path can form, is through a localized Al incursion into the n layer from the top AZO contact. Al is known to diffuse into a-Si:H matrix at high temperatures, which can eventually destroy the n-i junction in p-i-n solar cells. This Al can counter-dope a-Si:H as p-type and induce crystallization.

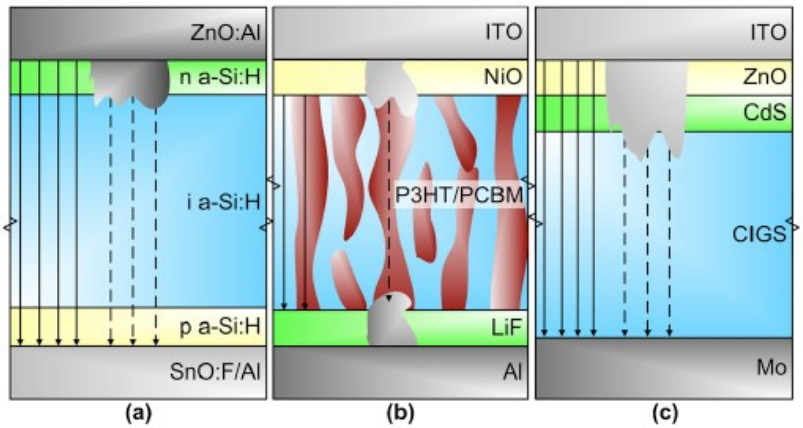

Figure 2.21: (Color online) Schematics showing the possible localized shunt structures in (a) a-Si:H cells, (b) OPV cells, and (c) CIGS cells. The dashed lines show the SCL shunt leakage current (I_{sh}) through these structures, which are in parallel to the ideal exponential diode current I_d (solid lines) [33]

S. Dongaonkar et al. [33] propose that during deposition of the AZO layer, local variations in deposition conditions such as temperature, microvoids in a-Si:H, etc. can cause Al incursions. This could result in the counter-doping, resulting in formation of localized symmetric a p-i-p structures instead of the ideal p-i-n as it is shown in Figure 2.21. Evidence from a-Si:H-based resistive switching memories also supports this Al incursion hypothesis [34, 35].

An easy method to eliminate the effect of the shunt leakage current from the current-voltage characteristics of a solar cell was suggested by S. Dongaonkar et al. The method is based on the symmetry of the shunt current about $V = 0$ as it is shown in Figure 2.22. This Figure shows the absolute value of the current-voltage plots (i.e., |I| vs |V|) for two samples of each cell type (squares and circles) where the forward and reverse currents overlap for ($V = 0.4 - 0.5V$). In the literature is well known that the measured forward current ($I_{dark,f}$) is a sum of the exponential ideal diode current component ($I_{d,f}$) and the shunt leakage current ($I_{Sh,f}$). In order to determine the actual exponential diode current it is necessary to subtract out the shunt current, i.e., $I_{d,f} = I_{dark,f} - I_{Sh,f}$. Now, we can use the symmetry of the shunt current ($I_{Sh,f} = I_{Sh,r}$) to determine the exponential diode forward current by simply subtracting the absolute value of the reverse current from the forward current ($I_{d,f} = I_{dark,f} - I_{Sh,r}$).

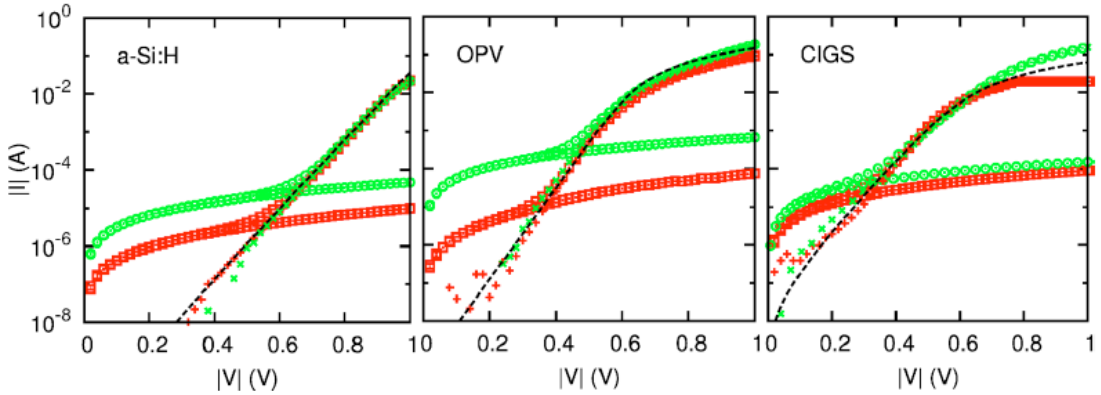

Figure 2.22: (Color online) Experimental dark current plotted in absolute value terms; i.e., |I| vs |V|, for two samples (shown as squares and circles) each from the three PV technologies discussed, highlighting the voltage symmetry in the shut current (I_{sh}) dominated regime. The "cleaned" current (pluses and crosses) is much closer to the diode model (dashed line) [33]

As it is shown in Figure 2.22, the “cleaned” forward current thus obtained (pluses and crosses), follows the expected exponential diode current (dashed lines). This cleaned forward current is consistent with the simulations of the idealized solar cell structure and follows the exponential current relation $I_d = I_0 * exp(qV/nk_BT)$. The noise at the lower current values in this cleaned currect-voltage characteristics reflects the limitations of the measurement instruments.

2.3.7 **Losses caused by the recombination effect**

Recombination losses affect both the current collection (and therefore the short-circuit current) as well as the forward bias injection current (and therefore the open-circuit voltage). Recombination is frequently classified according to the region of the cell in which it occurs. Recombination at the surface (surface recombination) or in the bulk of the solar cell (bulk recombination) are the main areas of recombination. The depletion region is another area in which recombination can occur (depletion region recombination). Surface recombination can have a major impact both on the short-circuit current and on the open-circuit voltage. High recombination rates at the top surface have a particularly detrimental impact on the short-circuit current since top surface also corresponds to the highest generation region of carriers in the solar cell. Lowering the high top surface recombination is typically accomplished by reducing the number of dangling silicon bonds at the top surface by using "passivating" layer on the top surface.

2.3.7.1 **Losses of current caused by the recombination effect**

In order for the p-i-n junction to be able to collect all of the light-generated carriers, both surface and bulk recombination must be minimised. In silicon solar cells, the two conditions commonly required for such current collection are:

1. The carrier must be generated within a diffusion length of the junction, so that it will be able to diffuse to the junction before recombining.

2. In the case of a localized high recombination site (such as at an unpassivated surface or at a grain boundary in multicrystalline devices), the carrier must be generated closer to the junction than to the recombination site. For less severe localised recombination sites, (such as a passivated surface), carriers can be generated closer to the recombination site while still being able to diffuse to the junction and be collected without recombining.

The presence of localized recombination sites at both the front and the rear surfaces of a silicon solar cell means that photons of different energy will have different collection probabilities. Since blue light has a high absorption coefficient and is absorbed very close to the front surface, it is not likely to generate minority carriers that can be collected by the junction if the front surface is a site of high recombination. Similarly, a high rear surface recombination will primarily affect carriers generated by infrared light, which can generate carriers deep in the device. The quantum efficiency of a solar cell quantifies the effect of recombination on the light generation current.

2.3.7.2 **Losses of voltage caused by the recombination effect**

The open-circuit voltage is the voltage at which the forward bias diffusion current is exactly equal to the short circuit current. The forward bias diffusion current is dependent on the amount recombination in a p-n junction and increasing the recombination increases the forward bias current. Consequently, high recombination increases the forward bias diffusion current, which in turn reduces the open-circuit voltage. The material parameter which gives the recombination in forward bias is the diode saturation current. The recombination is controlled by the number of minority carriers at the junction edge, how fast they move away from the junction and how quickly they recombine. Consequently, the dark forward bias current, and hence the open-circuit voltage is affected by the following parameters:

1. The number of minority carriers at the junction edge. The number of minority carriers injected from the other side is simply the number of minority carriers

in equilibrium multiplied by an exponential factor which depends on the voltage and the temperature. Therefore, minimising the equilibrium minority carrier concentration reduces recombination. Minimizing the equilibrium carrier concentration is achieved by increasing the doping.

2. The diffusion length in the material. A low diffusion length means that minority carriers disappear from the junction edge quickly due to recombination, thus allowing more carriers to cross and increasing the forward bias current. Consequently, to minimise recombination and achieve a high voltage, a high diffusion length is required. The diffusion length depends on the types of material, the processing history of the wafer and the doping in the wafer. High doping reduces the diffusion length, thus introducing a trade-off between maintaining a high diffusion length (which affects both the current and voltage) and achieving a high voltage.
3. The presence of localised recombination sources within a diffusion length of the junction. A high recombination source close to the junction (usually a surface or a grain boundary) will allow carriers to move to this recombination source very quickly and recombine, thus dramatically increasing the recombination current. The impact of surface recombination is reduced by passivating the surfaces.

2.4 Hydrogenated Amorphous Silicon Germanium Thin Film Photovoltaic Devices

Until this moment, we have seen that by increasing the germanium content in the silicon-germanium alloy, the optical band gap of the alloy is reduced, the coefficient absorption is enhanced and is shifted to lower energies, the density of defect states is increased and hence the transport properties are deteriorated. On the other hand, we have also seen that the efficiency the solar cells is determined by the values of the open-circuit voltage and the short-circuit current. The open-circuit voltage and the short-

circuit current depends on the value of the optical band gap and hence the energy conversion efficiency of the solar cell also depends on the value of the optical band gap. The basic limits of the energy conversion efficiency of single-junction and tandem p-n and p-i-n diodes in function of the optical bandgap were established by F. Meillaud et al. [36] as it is shown in Figure 2.23 from thermodynamical considerations on radiative recombination and semi-empirical considerations on the classical diode equations. The peak efficiency occurs for a band gap in the range $E_{opt} = 1.4$ to $1.6eV$. The optical band gap of a-Si:H ($E_{opt} \approx 1.7eV$) is higher than optimum and the optical band gap of a-Ge:H ($E_{opt} \approx 1.1eV$) is lower than optimum. By changing the germanium content in the silicon-germanium alloys we can modify the optical band gap and obtain the optimal value of the band gap.

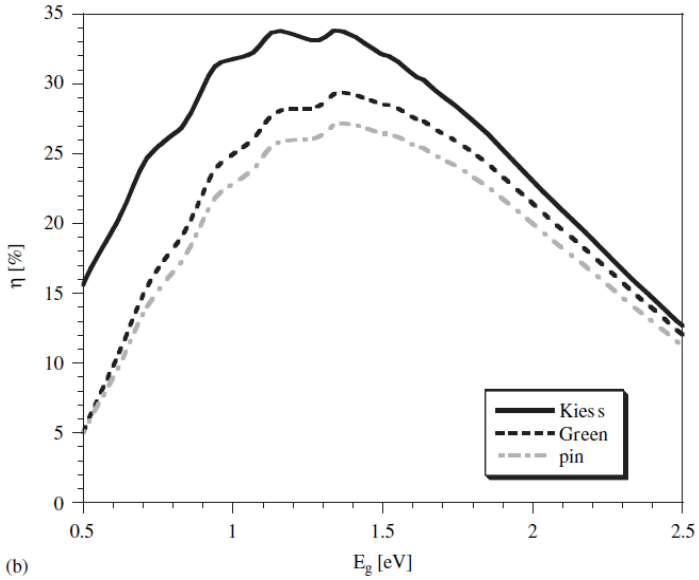

Figure 2.23: Upper limits of the energy conversion efficiency for solar cells as a function of the bangap energy Eg: thermodynamical limit, semi-empirical limit and p–i–n diode junction limit [36]

Currently, the a-SiGe:H alloys are widely used as the red absorber for a-Si:H based stacked solar cells or as a p-i-n botton cell for a-Si:H based tandem solar cells [37-39]. These solar cells in p-i-n or n-i-p configuration usually contain a-Si:H p- and n layers. Therefore, there is an optical band gap discontinuity at the p/i- and i/n interface. The

distribution of these discontinuities between conduction and valence band is not very well understood. In section 2.2.1.3 it was shown that the defect density of the a-SiGe:H thin films increases with decreasing of the optical band gap. In consequence, we have to expect a high-defect density at the p/i- and i/n interfaces which will adversely affect the internal electric field and the carrier collection and which results in poor open circuit voltages V_{oc} and FFs. In order to avoid bandgap discontinuities and high-defect densities at the p/i- and i/n interface, profiled a-SiGe:H-buffer layers between the doped and the absorption layers of amorphous silicon germanium (a-SiGe:H) solar cells are routinely used.

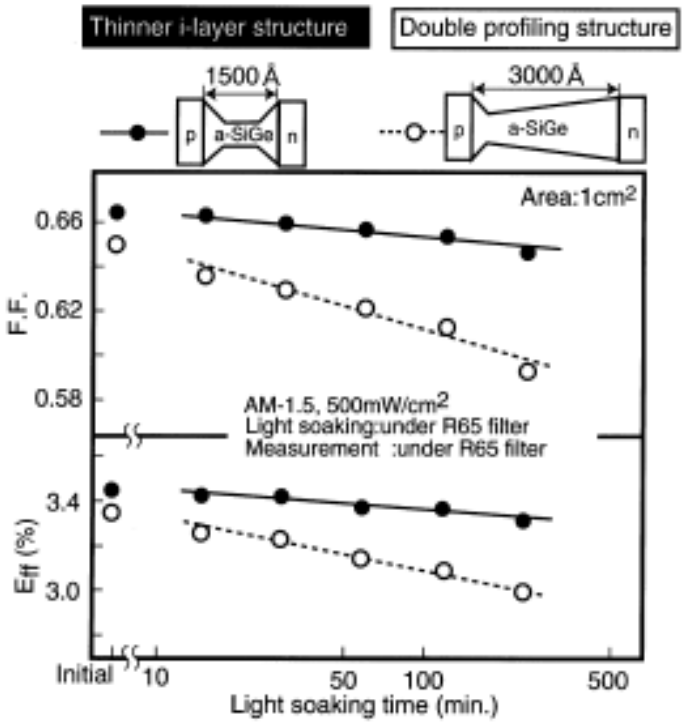

Figure 2.24: Light-induced degradation of a-SiGe single-junction cells using an accelerated test method under red light (>650 nm) [40]

The study conducted by E. Maruyama et al. [40] shows that the light-induced degradation of a-SiGe:H single-junction cells with profiled a-SiGe:H buffer layers can be improved using a thinner i-layer structure with high internal electric field as it is shown in Figure 2.24. This figure shows the light induced degradation of a-SiGe single-

junction cells with the thinner i-layer structure as compared to those with the double profiling structure using an accelerated test method (AM1.5, $500\,mW/cm^2$ light through an R65 filter which allows passage of longer wavelength ($> 650nm$) light, open circuit). Here, the i-layer thickness of the thinner i-layer structure and that of the double profiling structure was 1500 and 3000Å, respectively. This figure clearly indicates that not only the initial efficiency but also the stability against light soaking can be improved by using the thinner i-layer structure.

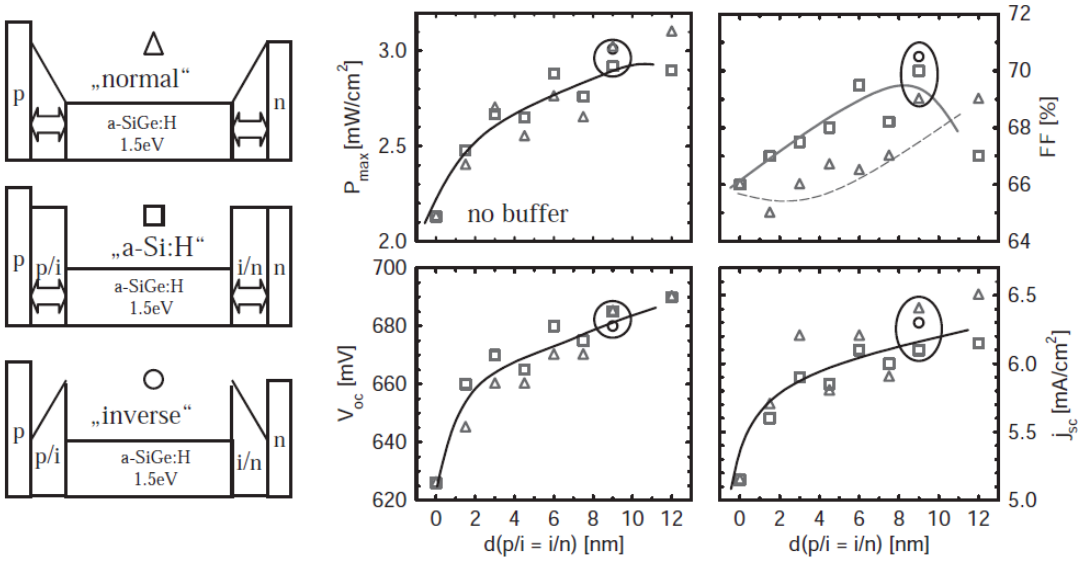

Figure 2.25: Comparison between a-SiGe:H solar cells with a-Si:H-buffer layers and profiled a-SiGe:H buffer at the p/i- and i/n interface. The values for FF and V_{OC} are measured as a function of the thickness d of the buffer layer. $d(p/i) = d(i/n)$. (■) Cells with a-Si:H buffer, (Δ) cells with profiled a-SiGe:H buffer, (O) cell with inverse profiled a-SiGe:H buffer [41]

The results reported by D. Lundszien et al. [41] show that profiled a-SiGe:H buffer can be replaced by a-Si:H buffer layers without any losses in FF and V_{oc}: A buffer layer of a certain thickness ($10nm$) is needed to obtain high V_{oc} and FF, but apparently a profiled a-SiGe:H buffer is not necessary. Figure 2.25 shows the performance characteristics obtained in three p-i-n solar cells with profiled a-SiGe:H buffer and non-profiled a-Si:H buffer layers at the p/i- and i/n interfaces. In these solar cells the buffer layer thickness is $9nm$. The thickness of the a-SiGe:H absorber layer was kept constant at $54nm$.

In Figure 2.25 it is shown that the open circuit voltage (V_{oc}) shows no difference between profiled and non-profiled buffer shape upon changing the buffer thickness. V_{oc} increases from $625mV$ (without buffer) to $690mV$ using a buffer thickness of about $12nm$. On the other hand, FF increases for a-Si:H-buffer layer thickness up to p/i = i/n = $10nm$, but for the profiled a-SiGe:H buffer shape the FF first remains at a low level up to $3nm$ buffer thickness. Between 3 and $10nm$ the FF is nearly 2% (absolute) higher for the a-Si:H buffer compared to the profiled a-SiGe:H buffer. The performance of an ‘‘inverse’’ profiled structure is also presented in Figure 2.25. In this structure the ‘‘worst case’’ is realized by applying two optical band gap steps, a small optical band gap (1.5 eV) and an enhanced defect density at both interfaces. Surprisingly, it turns out that the optical band gap profiling at the p/i- and i/n interface can be even inverted without any loss in FF and V_{oc}.

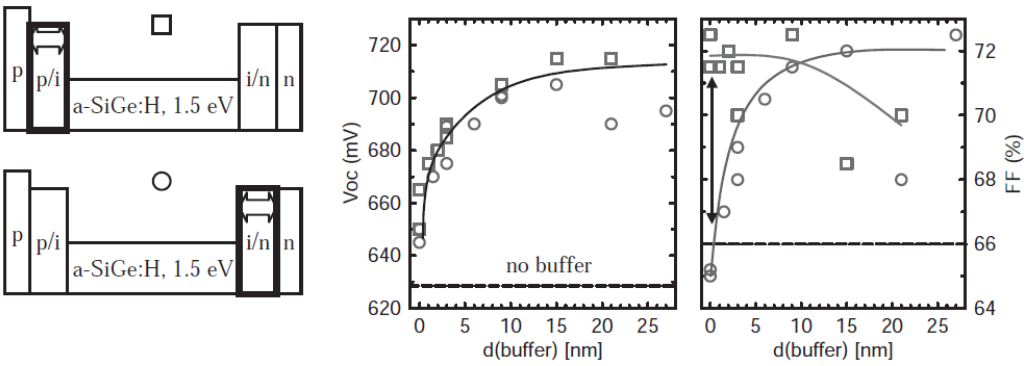

Figure 2.26: Comparison between a-Si:H-buffer layer at the p/i- and i/n interface. The values for FF and VOC are measured as a function of the thickness d of the buffer layer. (■) p/i interface, (O) i/n interface. The dashed line indicates the values for a cell without buffer layers [41]

The values for FF and V_{oc} as a function of the thickness of the buffer layer are plotted in Figure 2.26. For the V_{oc} nearly the same behavior upon increasing the a-Si:H buffer thickness is observed for both interfaces. Up to a buffer layer thickness of $5nm$ V_{oc} increases strongly and saturates above $15nm$. To obtain a high V_{oc} a buffer at each interface is necessary—a single buffer ($d = 0nm$) shows only small increase as compared to the V_{oc} level for a cell with no buffer layer (dashed line). The FF exhibits

different trends upon varying the buffer thickness. The FF remains nearly unaffected at high values upon changes of buffer thickness at the p/i interface. On the other hand, the FF is very sensitive to changes of the a-Si:H buffer thickness at the i/n interface. Starting at low FF values (no buffer = dashed line) the FF increases strongly with buffer thickness and saturates above $10nm$.

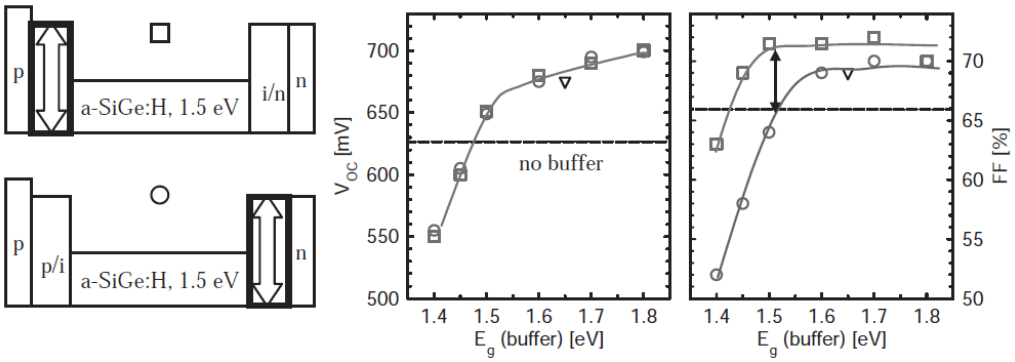

Figure 2.27: Comparison between buffer layers (9 nm) of different optical bandgap EG at the p/i- and i/n buffer. The values for FF and VOC are measured as a function of the optical bandgap of the buffer layer. (■) p/I interface, (O) i/n interface, (Δ) cell with $E_G = 1.65eV$ for both buffers. The dashed line indicates the values for a cell without buffer layers [41]

To investigate the influence of the optical band gap of the buffer layer on the solar cell performance, the optical band gap of the buffer layer at the p/i–i/n interface was varied keeping the optical band gap of the buffer at the i/n–p/i interface constant at $E_G = 1.8eV$ (a-Si:H). The thickness of the buffers at both interfaces is $9nm$. The values for FF and V_{oc} as a function of the optical band gap of the buffer layer are plotted in Figure 2.27. For V_{oc} the same trend upon decreasing the optical band gap of the buffer at the p/i- and i/n interface was observed by D. Lundszien et al. A small decrease in V_{oc} occurs for $E_G > 1.5eV$ for the buffer followed by a strong decease for $E_G < 1.5eV$. The FF remains unchanged down to E_G values of $1.5eV$ $(1.6eV)$ for the buffer at the p/i–i/n interface, respectively. Below these optical band gaps the FF decreases. For changes at the i/n interface the decrease in FF is more pronounced and occurs already at higher optical band gaps. So the FF is more sensitive upon changes of the optical band gap at the i/n interface than at the p/i interface.

2.5 Work done previously in INAOE

The literature analysis performed in the previous section shows that by reducing the temperature of deposition or by changing the germanium concentration, we can significantly modify the optical and electronic properties of silicon-germanium. However in these results, the germanium concentration was only changed over a range from $C_{Ge} = 0$ to 60%. Results about silicon-germanium thin films with germanium concentration higher than $C_{Ge} = 60\%$ are not reported commonly. In contrast to the works reported in literature, this section shows that the optical and electrical properties of germanium thin films can be improved by adding a small concentration of silicon ($C_{Si} = 0.03\%$).

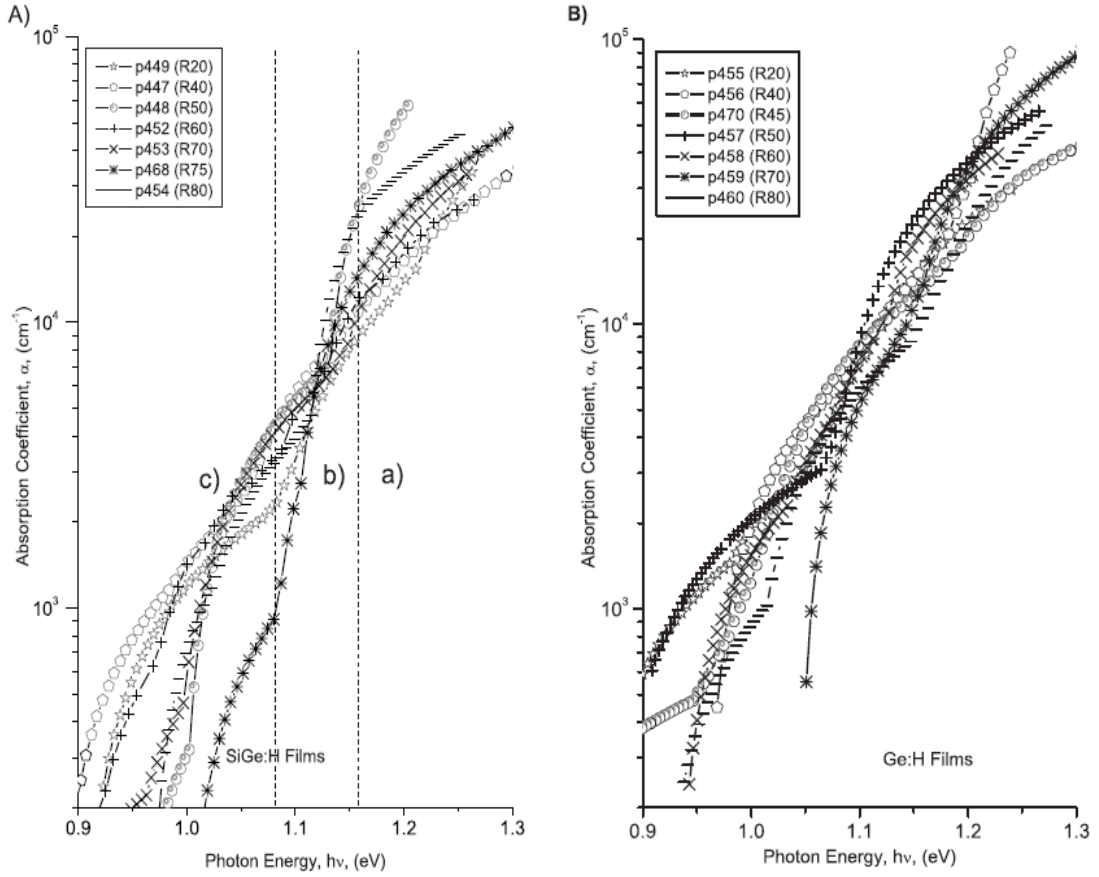

Figure 2.28: Spectral dependence of optical absorption coefficient for different hydrogen dilution, R, for a) SiGe:H and b) Ge:H films [42]

Figure 2.28 shows the spectral dependence of optical absorption coefficient for different hydrogen dilution, R_H, for a) silicon-germanium and b) germanium thin films. Figure 2.29 shows the temperature dependence of the dark conductivity for a) silicon-germanium and b) germanium thin films deposited at various hydrogen dilution rates $R_H = 20 - 80$. The thin films of silicon-germanium and germanium were deposited by Sanchez et al. [42] in the laboratories of the National Institute of Astrophysics, Optics and Electronics (INAOE).

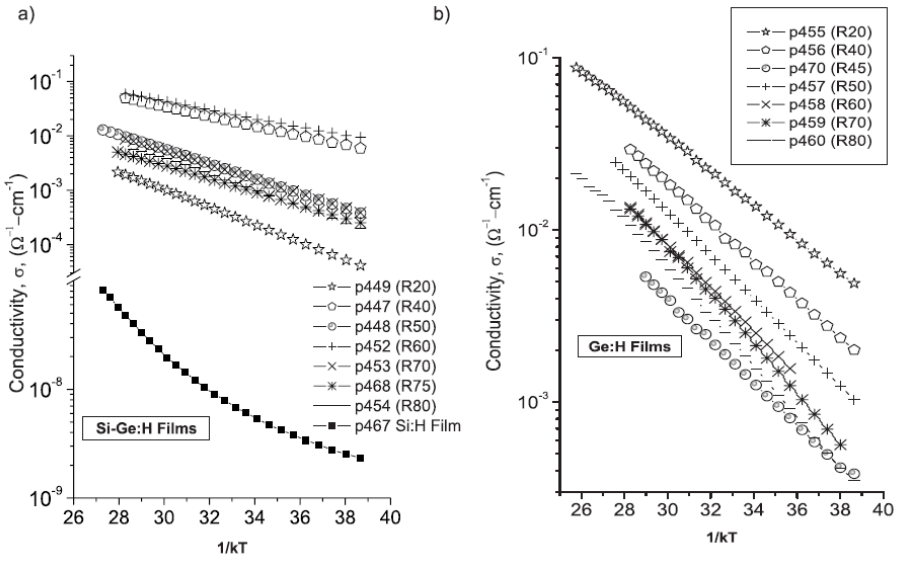

Figure 2.29: Temperature dependence of the dark conductivity for a) SiGe:H and b) Ge:H samples deposited at various hydrogen dilution rates R = 20-80 [42]

From Figure 2.29 we can observe that the dark conductivities of the samples are between $\approx 5x10^{-5}$ and $\approx 5x10^{-3}\Omega^{-1} * cm^{-1}$ as hydrogen dilution was increased from $R_H = 20$ to 80. The transport properties are influenced by the interaction of the charge carriers with the localized tail defect states. This interaction can cause an increase in the transit time of the carrier, because these tail defect states act as traps. Moreover, the mid-gap defect states are playing the role of recombination centers, which degrade the transport properties. Therefore, a reduction in the tail defect density and mid-gap defect states will result in the improvement of the transport properties of the material. The density of the tail states is proportional to the Urbach energy (E_u).

The Urbach energy was determined in the region $hv \leq E_g$, where absorption can be described as $\alpha(hv) = \alpha_g exp\big((hv - E_g)/E_u\big)$ where α_g is the absorption coefficient at $hv = E_g$. These characteristics are shown in Figure 2.28. As the value of E_u is smaller, the material has lower density of tail defects and the film quality improves.

Table 2.1: Optical and electrical properties for nc-Si, a-Ge and nanostructured silicon.

Material	$\sigma_{RT}(\Omega^{-1}cm^{-1})$	$E_a(eV)$	$E_{04}(eV)$	$E_u(eV)$	Ref.
a-Ge:H	$4x10^{-5}$	0.49	1.22	52	[43]
a-Ge:H	$5.3x10^{-5}$	0.43	1.20	65	[44]
nc-Ge:H	$1x10^{-4}$	0.40	1.22	---	[55]
nm-Ge:H	---	---	---	42	[46]
nm-SiGe	$2.5x10^{-4}$	0.28	1.14	30	[42]

Some of the published values of E_u are shown in Table 2.1. It is noticed that, the Urbach energy is larger for a-Ge ($E_u = 50 - 60meV$) [47], [48] than for the nanostructured silicon films ($E_u = 42meV$) [49]. For the nanostructured SiGe:H films shown in Figure 2.28 and Figure 2.29 an Urbach energy $E_u = 30meV$ at $R_H = 75$ has been achieved. It is suspected that silicon atoms play a key role in the reduction of dangling bonds and the defect state density. As a consequence, the morphology resulting on this film together with the small amount of silicon atoms, both result in germanium films with improved electronic properties.

Drawing on the results obtained by Sanchez et al. [42], the next step was reduce the deposition temperature of silicon-germanium thin films in order to use them in flexible photovoltaic applications. The development of the photovoltaic devices presented in this thesis was divided into two parts: the first part is related to the manufacture and technological characterization performed by Dr. I. Cosme [50] (results shown below), the second part is related to the opto-electronics characterization of photovoltaic devices. The opto-electronics characterization is presented in the following chapters of this thesis. In Figure 2.30 it is shown the FTIR absorption spectra for silicon-germanium thin films deposited by PECVD at deposition temperature range from $T_d =$ 70 to 300℃ by Cosme et al. [50]. The study of hydrogen bonding by FTIR is used to

calculate the relative hydrogen contentment in the temperature series samples. The spectra show main peaks for germanium-hydrogen bounding; bending mode ($k = 565cm^{-1}$) and stretching mode ($k = 1880cm^{-1}$). Not absorption peaks in relation with silicon-hydrogen absorption is observed, stretching mode Si-H $k = 2000cm^{-1}$ and bending mode $k = 630cm^{-1}$. This is because of the high concentration of germanium, which is more than 95% of the composition of the films and low concentration of silicon in solid phase.

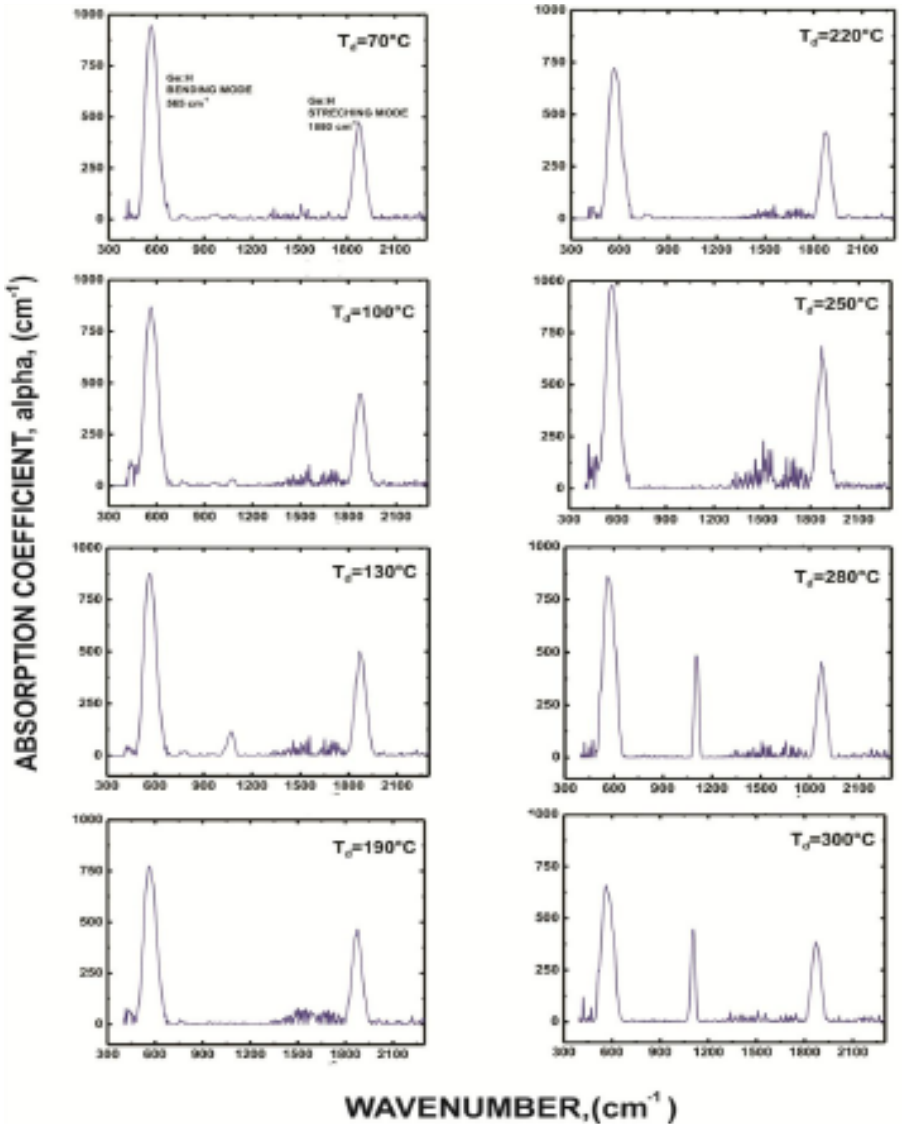

Figure 2.30: FTIR absorption spectra for GeSi:H films deposited by PECVD at deposition temperature range from T_d = 70°C to 300°C [50]

An absorption peak is observed at deposition temperatures of $T_d = 130℃$, 280℃ and 300℃, this peak corresponds to O-H stretching mode ($k \approx 1100cm^{-1}$). The measurements of absorption show clear spectra with dominant peaks of monohydrate germanium-hydrogen that is characteristic of good quality films. The Figure 2.31(a) shows the germanium-hydrogen stretching mode peaks at $T_d = 70℃$ and $T_d = 300℃$ in the selected region $k = 1800$ to $2000cm^{-1}$ and Figure 2.31(b) shows hydrogen content C_H as a function of deposition temperature. The Figure 2.31(a) shows IR spectrum for the film deposited at $T_d = 70℃$ with higher concentration of germanium-hydrogen bonds (i.e. hydrogen content) in comparison with sample deposited at $T_d = 300℃$. The Figure 2.31(b) demonstrates that in general the increases of temperature results in decrease of bound hydrogen content. Except for the sample at deposition temperature $T_d = 250℃$ that shows abrupt increase in hydrogen content.

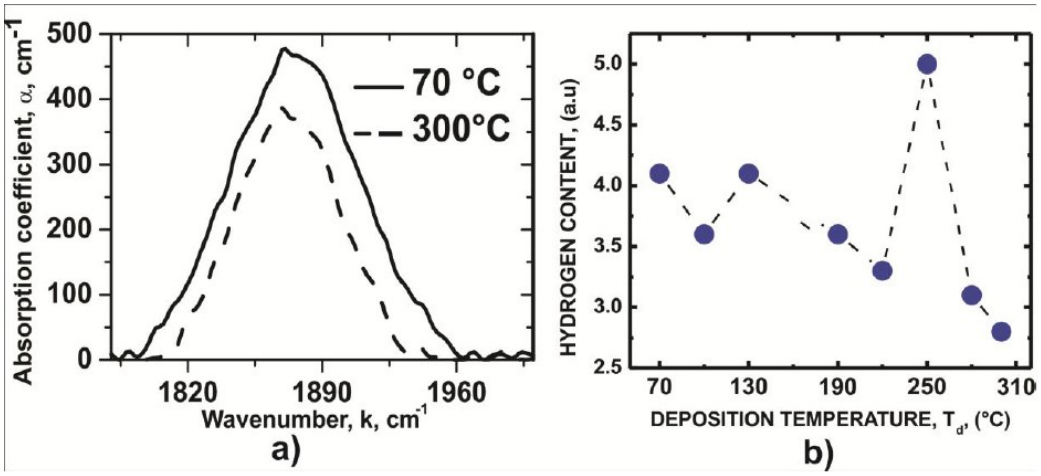

Figure 2.31: Hydrogen content calculated by FTIR a) Ge-H stretching mode peaks for GeSi:H films at deposition temperatures 70°C and 300°C, b) relative hydrogen bounding content versus deposition temperature [50]

Figure 2.32 shows the optical band gap which is characterized by the E_{04} and E_g^{TAUC} in function of deposition temperature. E_{04} and E_{03} energies correspond to absorption coefficients $\alpha = 10^{-4}cm^{-1}$ and $\alpha = 10^{-3}cm^{-1}$, respectively. The energies characteristic for localized states are: $\Delta E = E_{04} - E_{03}$ is the energy that describes with the slope of $\alpha(hv)$, and Urbach energy E_u that describe the exponentially decreasing

tails of states near the valence band and conduction band edges. The energy E_{04} and E_g^{TAUC} shows no continuous changes with increases of deposition temperature and show a similar behavior as it is shown in Figure 2.32. Energy E_{04} changed over a range from $E_{04} = 1.11$ to $1.19eV$. The minimum value of energy E_{04} was obtained at a temperature deposition of $T_d = 190$℃. The minimum value of the Tauc optical band gap also was obtained at a deposition temperature of $T_d = 190$℃. The Urbach energy E_u and ΔE characteristic energy are shown in Figure 2.33 as function of deposition temperature.

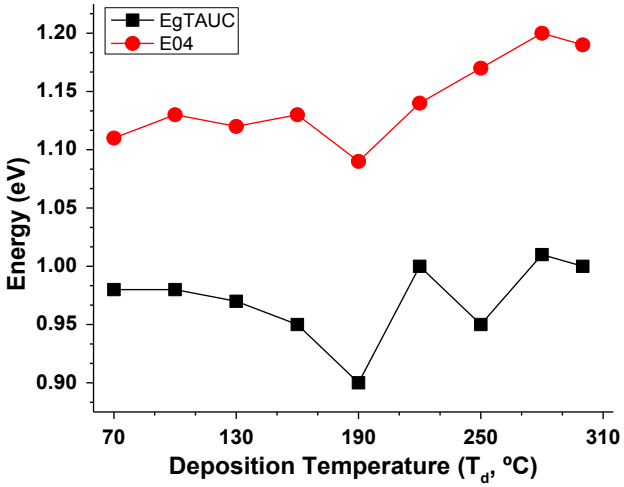

Figure 2.32: Optical gap characterized by E_{04} and E_g^{TAUC} energies as function of deposition temperature for GeSi:H films. Solid lines are guide to the eyes [50]

The Urbach energy is plotted in Figure 2.32(a) as function of deposition temperature T_d. Lower values of Urbach energy has relation with good electronic properties of the film. The lowest value $E_u = 33meV$ is obtained at deposition temperature $T_d = 160$℃. Best values are obtained at deposition temperature range from $T_d = 160$ to 220℃. An interesting result is that the highest values of Urbach energy are not obtained at lower deposition temperatures. The tendency of Urbach energy is not continuous with the decrease of deposition temperature. The ΔE characteristic energy has relation with the slope in the distribution of states in the optical gap. Low ΔE energy has relation with low density of states (DOS). The energy ΔE is shown in Figure 2.32(b) as function

of deposition temperatures. Minimum value $\Delta E = 50meV$ is obtained at deposition temperature $T_d = 190$℃. Lower values are obtained in the region from $T_d = 160$ to 220℃ in correlation with Urbach energy data. The data of ΔE shows a change not continuous with deposition temperature and maximum value is obtained at lower temperature deposition $T_d = 70$℃.

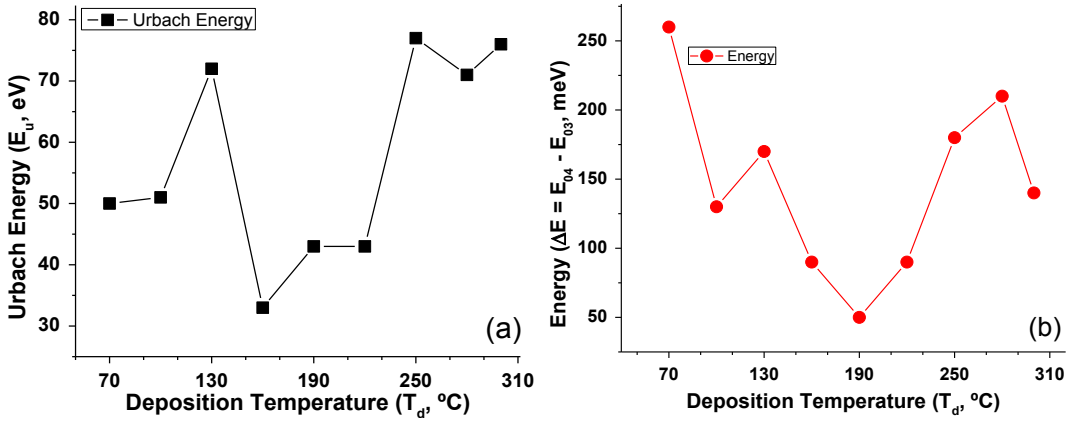

Figure 2.33: a) Urbach energy E_u and b) characteristic energy $\Delta E = E_{04} - E_{03}$ as function of deposition temperature for GeSi:H films [50]

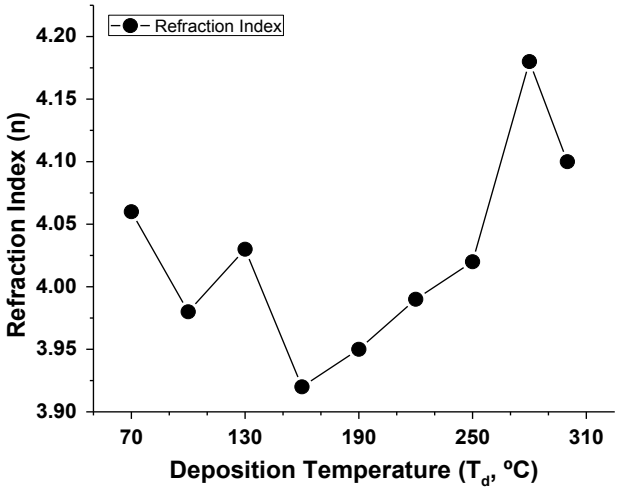

Figure 2.34: Refractive index n_∞ as function of deposition temperature [50]

Refraction index n_∞ is calculated and plotted as a function of deposition temperature in Figure 2.34. This parameter reveals information of the density of the films. Maximum value is obtained at deposition temperature $T_d = 280$℃ and

minimum value of refraction index is obtained at deposition temperature $T_d = 160$℃. Decrease of refraction index is observed from deposition temperatures $T_d = 300$ to 160℃ then change of trend for lower temperatures from $n_\infty = 3.92$ to 4.1. The variation of refraction index in the range of $n_\infty = 3.92$ to 4.18 reveals a strong effect of deposition temperature on the films structure.

In Figure 2.35 it is shown the dark conductivity at room temperature as a function of deposition temperature. The minimum value of dark conductivity $\sigma_{Dark} = 1.3x10^{-5}\Omega^{-1} * cm^{-1}$ was obtained at a temperature of $T_d = 190$℃. The maximum value of dark conductivity $\sigma_{Dark} = 9.6x10^{-4}\Omega^{-1} * cm^{-1}$ was obtained at a temperature of $T_d = 300$℃. The ratio of maximum and minimum values obtained is about one order of magnitude.

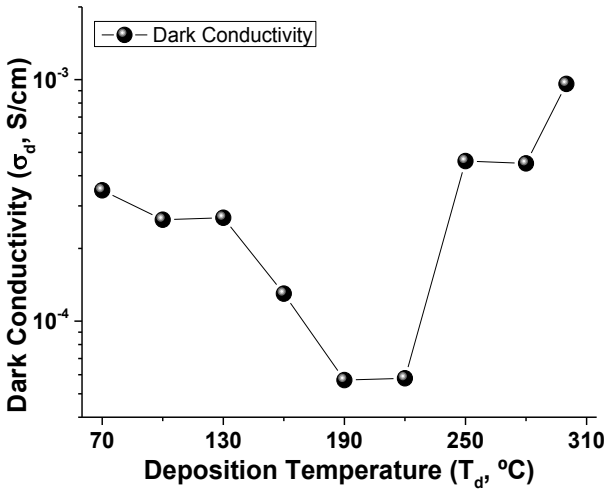

Figure 2.35: Dark conductivity as a function of deposition temperature [50]

Thermal activation energy E_a and Fermi Energy level E_F are plotted as a function of deposition temperature in Figure 2.36. Figure 2.36 shows the maximum values of activation energy $E_a = 0.38eV$ and Fermy level $E_F = 0.37eV$ at a temperature deposition of $T_d = 220$℃. For a temperature deposition higher than $T_d > 160$℃, the activation energy and Fermi level are more sensitive without continuous change.

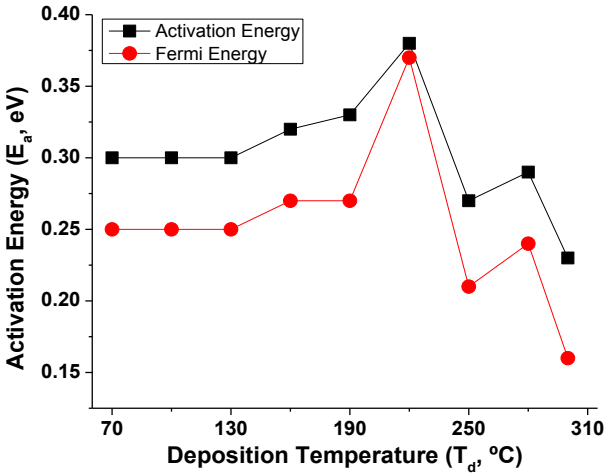

Figure 2.36: Activation energy, E_a, and Fermi Energy, E_F, as a function of deposition temperature T_d [50]

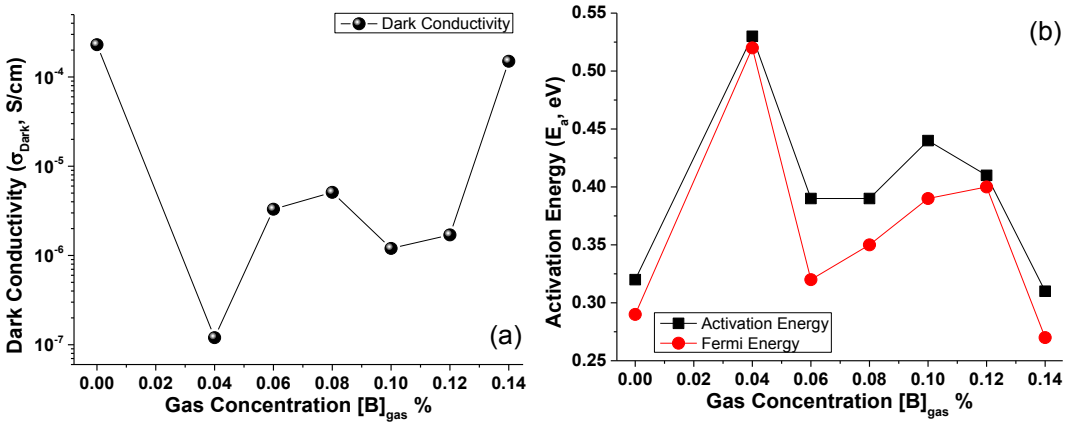

Figure 2.37: Electronic properties as a function of boron concentration in gas phase for a) dark conductivity and b) activation energy and Fermi energy level for GeSi:H films deposited at low deposition temperature $T_d = 160$℃ [50]

Figure 2.37 shows the electronic properties results as a function of gas concentration for boron doping. The dark conductivity σ_{Dark} for boron doped films are shown in Figure 2.37(a). The changes in orders of magnitude of the dark conductivity demonstrate doping and the changes in activation energy demonstrates the control of doping in films deposited at low deposition temperature $T_d = 160$℃. The dark conductivity σ_{Dark} shows a drastically reduction with increase of boron from $[B]_{gas} =$ 0 to 0.04%, this effect suggest a compensation of electron conductivity in non-doped

film and further increases from $[B]_{gas} = 0.04$ to 0.14% results in increase of conductivity. The Figure 2.37(b) shows not continuous change in activation energy and Fermi level position. The compensation effect has correlation with the activation energy maximum $E_a = 52meV$ and the lowest value for dark conductivity $\sigma_{Dark} = 10^{-7}\Omega^{-1}cm^{-1}$ for $[B]_{gas} = 0.04\%$ [50].

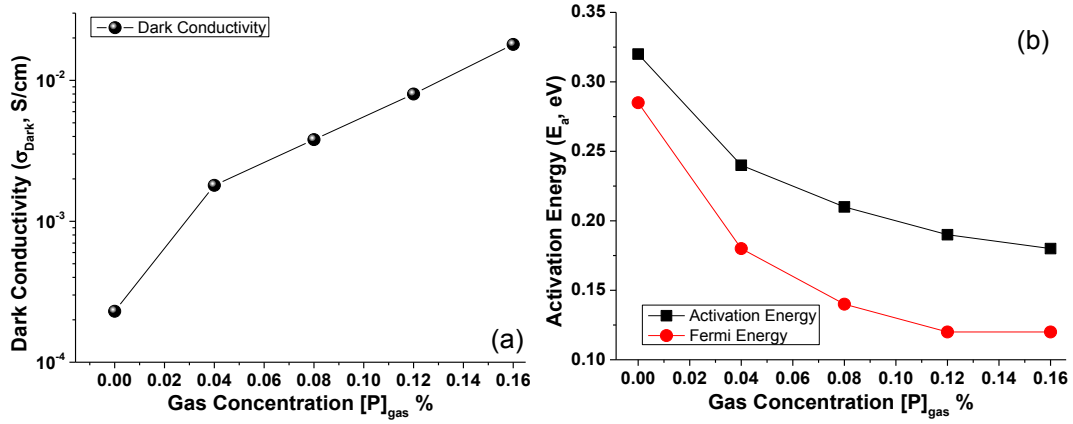

Figure 2.38: Electronic properties as a function of phosphorus concentration in gas phase for a) dark conductivity and b) activation energy and Fermi energy level for GeSi:H films deposited at low deposition temperature $T_d = 160$℃ [50]

For n-type films study the Figure 2.38 shows electronic characterization for phosphorus series. Dark conductivity σ_{Dark} for phosphorus doping is shown in the Figure 2.38(a). The films demonstrated saturation of conductivity with change in one order of magnitude. The changes in orders of magnitude demonstrate doping and control of electronic characteristics for phosphorous doping at low deposition temperature $T_d = 160$℃.

2.6 Conclusion

As it was mentioned above, the silicon-germanium thin films are commonly used in solar cell technology to absorb longer wavelengths of the solar spectrum. However, the optic and electronic properties of the thin films of silicon-germanium deteriorate with increasing germanium content in the alloy. This behavior may explain why in the state-

of-art there are only few studies on the optic and electronic characteristics of silicon-germanium thin films with high germanium content ($C_{Ge} > 70\%$) and germanium thin films compared with studies in silicon-germanium thin films with low germanium content ($C_{Ge} < 60$) and silicon thin films for example [1-67]. Furthermore, most of the studies performed to the silicon-germanium thin films and photovoltaic devices are mainly dedicated to the study of structural properties and their relationship to the deposition conditions. In other words, in the state-of-art usually are not performed systematic studies of the optical and electronic properties of photovoltaic devices.

Table 2.2: Review of material properties and performance characteristics of photovoltaic devices reported in the literature. Nomenclature utilized: ■ parameters reported, □ parameters no reported, and ■ parameters no obtained in this work.

Parameter	References														
	51	52	53	54	55	56	57	58	59	60	61	62	63	64	65
Performance characteristics															
J_{SC}	■	■	■	■		■	■	■	■		■	■	■	■	■
V_{OC}	■	■	■			■	■	■	■	■	■	■	■	■	■
FF (structure)	■	■	■			■	■	■	■	■	■	■	■	■	■
FF (diode)															
η (structure)			■			■	■	■	■		■	■	■	■	■
η (diode)															
I_0			■					■				■		■	
Illumination			■	■			■	■	■	■	■	■		■	■
Spectral response						■			■				■		■
Stability						■		■					■	■	
Dark I-V							■		■						
Light I-V						■	■	■	■		■	■	■	■	■
Quantum efficiency							■	■			■			■	■
Properties of the intrinsic material and his interfaces															
Urbach Energy															
Mobility – h					■										
Mobility – e					■										
Series resistance															
Shunt resistance															
Activation Energy									■						
Surface recombination										■					
Ideality factor															

Table 2.2 shows the parameters reported in a set of articles related to the study of electronic and optical characteristics of thin film photovoltaic devices for amorphous, polymorphous, and microcrystalline silicon and silicon-germanium thin films. The white boxes represent the parameters not reported in our analysis performed to the state-of-art. The yellow boxes represent parameters not studied in this work and colored boxes represent the parameters reported. In this table we can see that the performance characteristics (i.e., the open circuit voltage, V_{oc}, short circuit current, J_{sc}, fill factor, FF, and power-conversion efficiency, η) are commonly reported in the literature. Studies on the stability of the photovoltaic devices (Staebler-Wronski Effect) are not commonly reported. In some works, the current-voltage characteristics in dark and under illumination are mentioned but a systematic analysis of the I-V characteristics is not performed in these works. The quantum efficiency and the spectral response of photovoltaic devices is not commonly reported. Knowledge about performance characteristics is not enough to analyze physical processes and technological problems in photovoltaic device structures. It is necessary to have diagnostic methods (parameters). In Table 2.2 we can also observe that in the photovoltaic devices, very limited data related to diagnostic characteristics are reported (i.e., mobility of electrons and holes of the active layer, Urbach energy, surface recombination, bulk recombination, activation energy, metal-contact resistance, contact resistance, spreading resistance in the top layer, resistance of the active layer, etc.).

Chapter 3

Methodology and Characterization Techniques

3.1 Introduction

The main electrical parameters of the solar cell - such as the short-circuit current, the open-circuit voltage, the maximum power, the fill factor, and the maximum conversion efficiency - are functions of the resistance of solar cells, i.e., the series resistance and the shunt resistance. This is what causes low energy-conversion efficiency in the photovoltaic modules. Hence, it is worth paying more attention to how to efficiently control the operation of photovoltaic modules at maximum power output to the extent possible. Section 3.2 presents a description of the plasma deposition system, deposition conditions and description of thin film photovoltaic devices. In section 3.3 are described the characterization methods used to diagnose and develop the performance of thin film photovoltaic devices. Characterization methods such as current-voltage characteristics under dark and illumination conditions, temperature dependence of current-voltage characteristics under dark and illumination conditions, spectral response of performance characteristics, temperature dependence of spectral response of performance characteristics, spectral response of sub-gap absorption.

3.2 Fabrication of Photovoltaic Devices by PECVD Technique

Plasma-Enhanced Chemical Vapor Deposition (PECVD) is a process by which thin films of various materials can be deposited from a gas state to a solid state on heated substrates. The deposition process is achieved by introducing the reactant gases between two parallel electrodes — an RF energized electrode and a grounded electrode as is shown in Figure 3.1.

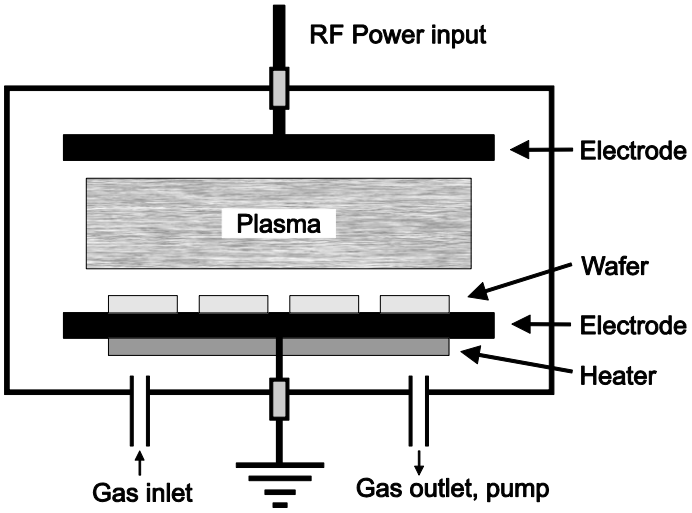

Figure 3.1: Experimental setup of the PECVD deposition system

The capacitive coupling between the two electrodes excites the reactant gases into a plasma state which induces the physical interactions and chemical reaction between the gases resulting in the product of the reaction being deposited on the substrate. The substrate, which is placed on the grounded electrode, is typically heated to $250℃ - 350℃$ depending on the specific film requirements.

A plasma is any gas which consists of neutral radicals and molecules, positive as well as negative ions, and electrons. The plasma is generally created by RF (AC) frequency or DC discharge between the two electrodes. Processing plasmas are typically operated at pressures of a few $mTorr$ to a few $Torr$, although arc discharges and inductive plasmas can be ignited at atmospheric pressure.

3.2.1 Experimental Setup of the Plasma Deposition System

In Figure 3.2 is shown the plasma deposition system (Model AMP 3300) from "Applied Materials Inc." utilized to deposit the a-Si:H/a-$Ge_{0.97}Si_{0.03}$:H thin film photovoltaic devices. The plasma deposition system consists of a reactor system were the gases are excited to generate the plasma, an RF power source to energize the reactor electrodes, temperature controllers to maintain the substrate temperature deposition, a gas control system and a pressure controller system.

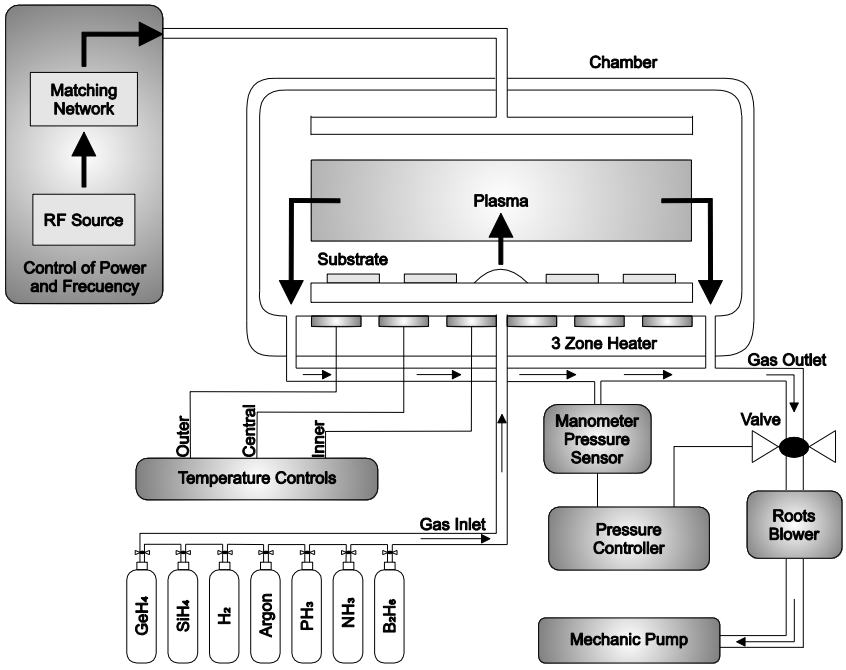

Figure 3.2: Scheme view of the plasma deposition system used for film deposition

The central part of the deposition system is the reactor system. In this part of the system the molecules are dissociated and the products are deposited on heated substrates to form a layer. The reactor has a capacitor electrode configuration with $26\ inches$ plate diameter and a separating distance of $2\ inches$. The RF source operates in the range of frequencies from $f = 90\ KHz$ to $f = 460\ KHz$ with an error of 0.1% and power range from 0 to $500\ Watts$. The power and ground are connected

to the top and down electrodes as is shown in Figure 3.1, respectively. The samples are loaded in the down electrode; which, can be heated from room temperature to 400℃. The temperature is supplied by the 3-zone heater and controlled by the temperature controllers. The gas control system includes mass flow controllers to measure and control the different gases (GeH_4, SiH_4, NH_3, Argon, H_2, PH_3, B_2H_6) supplied to the chamber. The vacuum system comprises the mechanic pump and the pressure controller. The deposition pressure can be controlled from 0.3 to 4 $Torrs$ [42].

3.2.2 Configuration and Fabrication of the Thin Film Photovoltaic Devices utilized in this study

In order to study the opto-electronic characteristics of photovoltaic devices deposited by Low Frequency Plasma-Enhanced Chemical Vapor Deposition (LF-PECVD) were utilized photovoltaic devices fabricated at installations of National Institute of Astrophysics, Optics and Electronics (INAOE) from Mexico and photovoltaic devices fabricated in Ecole-Polytechnique from France. The photovoltaic devices prepared at INAOE were deposited on glass (Corning 1737) substrate. The gases, flow and deposition parameters are summarized in Table 3.1. The deposition parameters were: pressure, $P = 0.6\,Torr$ for the films of a-$Ge_{0.97}Si_{0.03}$:H and $P = 1.4\,Torrs$ for the films of a-Si:H; power, $P_{out} = 300Watts$, substrate temperature $T_s = 160$℃; and frequency $f = 110kHz$. For the films of a-$Ge_{0.97}Si_{0.03}$:H the gas flow of Silane and Germane were $Q_{SiH_4} = 500\ sccm$ and $Q_{GeH_4} = 500\ sccm$, respectively. For the films of a-Si:H the gas flow of Silane was $Q_{SiH_4} = 500\ sccm$.

Table 3.1: Deposition parameters used in the fabrication of photovoltaic devices provided by National Institute of Astrophysics, Optics and Electronics

Film	$P_{out} = 300W$ $T_s = 160$℃ $f = 110kHz$	Q_{SiH_4} sccm	Q_{GeH_4} sccm	Q_{H_2} sccm	Q_{PH_3} sccm	$Q_{B_2H_6}$ sccm
p-type (a-$Ge_{0.97}Si_{0.03}$:H)	$P = 0.6\,Torrs$		500	3300		34 - 37
intrinsic (a-Si:H)	$P = 1.4\,Torrs$			550		
intrinsic (a-$Ge_{0.97}Si_{0.03}$:H)	$P = 0.6\,Torrs$	500	500	3300		
intrinsic (a-Si:H)	$P = 1.4\,Torrs$			550		
n-type (a-$Ge_{0.97}Si_{0.03}$:H)	$P = 0.6\,Torrs$		500	3300	22 - 23	

The gasses used for the deposition of a-$Ge_{0.97}Si_{0.03}$:H and a-Si:H thin films were diluted with a gas flow of hydrogen of $Q_{H_2} = 3300$ and $Q_{H_2} = 550$, respectively. The gas flow of diborane and phosphine were $Q_{PH_3} = 22\ sccm$ and $Q_{B_2H_6} = 34\ sccm$ for the process 1075, $Q_{PH_3} = 23\ sccm$ and $Q_{B_2H_6} = 35\ sccm$ for the processes 1076, 1078, 1079, and $Q_{PH_3} = 23\ sccm$ and $Q_{B_2H_6} = 37\ sccm$ for the process 1089 as is shown in Table 3.2.

Table 3.2: Gas flow of diborane and phosphine on each deposition process

Process	Q_{PH_3} $sccm$	$Q_{B_2H_6}$ $sccm$
1075	22	34
1076	23	35
1078		
1079		
1086		37

The photovoltaic devices of a-$Ge_{0.97}Si_{0.03}$:H were fabricated in $p_{GeSi} - i_{Si} - i_{GeSi} - i_{Si} - n_{GeSi}$ sequence on Ti-coated glass substrate. Initial configuration of photovoltaic devices is similar to the conventional configuration of a p-i-n device. The principal difference between the configuration of the photovoltaic devices of a-$Ge_{0.97}Si_{0.03}$:H and the configuration of a p-i-n device are the a-Si:H thin films deposited between the p-i and i-n interfaces as is shown in Figure 3.3a.

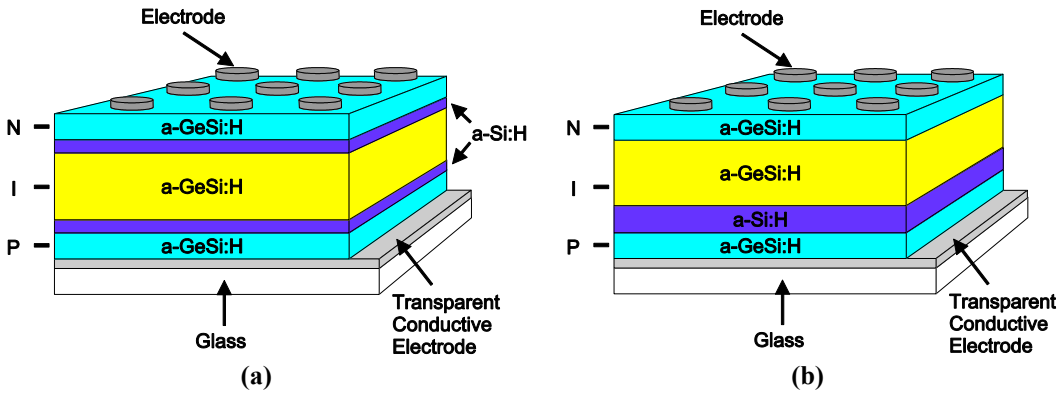

Figure 3.3: Configuration of photovoltaic devices deposited at INAOE installations. (a) Initial and (b) final configuration used for photovoltaic devices

The main function of the a-Si:H film is avoid the diffusion of boron and phosphorous from the p- and n-type films into the intrinsic film of a-$Ge_{0.97}Si_{0.03}$:H. Results obtained in this work proved that the a-Si:H films play a very important role in the performance of the photovoltaic devices. Therefore, the configuration of the photovoltaic devices was modified so that it was possible to reach a better performance of the photovoltaic devices (see Figure 3.3b). The changes done in the configuration of the photovoltaic devices are shown in Table 3.1. To understand why these changes were necessary the reader must analyze the data reported in chapter 4: Experimental Results.

Table 3.3: Thicknesses (Å) of the films that constitute the photovoltaic devices fabricated at installations of National Institute of Astrophysics, Optics and Electronics

Process	Substrate	Contact	p-type GeSi:H	intrinsic a-Si:H	intrinsic GeSi:H	intrinsic a-Si:H	n-type GeSi:H	Contact
1075				500				
1076				350		500		
1078				630	9200			
1079			160	715		107	240	
1086				1071				
1115				1070		0		
1114					6100			
1109				1300	7300			

On the other hand, the photovoltaic devices provided by the Ecole-Polytechnique installations are conventional pin structure of polymorphous (pm-Si:H) and microcrystalline (μc-Si:H) silicon thin films as is shown in Figure 3.4. The devices based on pm-Si:H were fabricated in p-i-n sequence by conventional RF Plasma-Enhanced Chemical Vapor Deposition (RF-PECVD) at $f = 13.56\,MHz$ on glass substrates coated with ASAHI U-type textured thin-oxide. The $10\,nm$ thin P-layer made of an a-SiC:H alloy in order to increase the optical gap and allow more photons to be absorbed. The i-layer was deposited either from pure Silane (standard a-Si:H) or from Silane–hydrogen or Silane–helium mixtures under conditions close to powder formation that yield polymorphous films. The collection area defined by Ag contact back is $3.14x10^{-2}cm^2$[63].

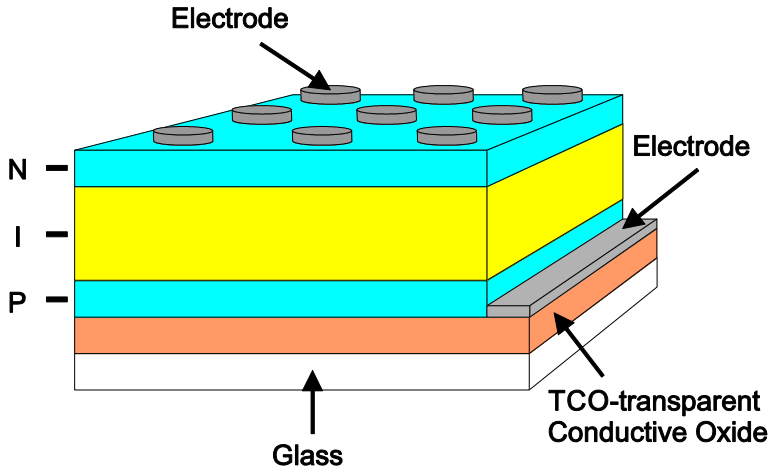

Figure 3.4: Configuration of the pm-Si:H and µc-Si:H p-i-n structures provided by the LPICM, Ecole-Polytechnique

The devices based on µc-Si:H were fabricated in p-i-n sequence by conventional RF-PECVD on 2.5 x 2.5 cm^2 texture-etched ZnO: Al-coated glass substrates. Active layer deposition and H_2 plasma treatment were performed by standard RF-PECVD at $f = 13.56\ MHz$. The i-layer µc-Si:F:H was deposited from a SiF_4, H_2 and Ar gas mixture in a single chamber system using an inter-electrode distance of 3 cm. The Q_{SiF_4}, Q_{H_2} and Q_{H_2} flow rates used were 3, 3 and 70 $sccm$, respectively, and no inline gas purifiers were used. A deposition pressure of $P = 2.7\ Torr$, an RF power of $P_{out} = 440\ mW/cm^2$, and a substrate temperature of $T_s = 200$°C were used, resulting in a deposition rate R_D of ~ 2.5 A/s. The µc-Si:H p-layer and a-Si:H n-layer were deposited in a second, multi-chamber reactor, using TMB and PH_3 as dopant sources, and necessitating a vacuum break between the deposition of the doped and intrinsic layers. A 75 nm intrinsic µc-Si:H buffer layer (before air break) and a hydrogen plasma pre-treatment (after both air breaks) were therefore independently applied towards passivation of the p-i and i-n interfaces. All the solar cells are ≈ 1.5 μm thick and have a collection area defined by Ag contact back of 0.126 cm^2 [65].

3.3 Characterization Techniques used to Diagnose and Develop the Performance of Photovoltaic Devices

In this section are described the methodologies and characterization techniques used to study, reveal and understand some of the problems related to the performance and fabrication technology of photovoltaic devices. For each characterization technique are depicted the experimental setup of the measurement equipment and the data processing performed to extract the performance and diagnosis characteristics. The methodologies and characterization techniques described in this section are: current-voltage characteristics under dark and illumination conditions, temperature dependence of current-voltage characteristics, spectral response of performance characteristics, temperature dependence of spectral response of performance characteristics, spectral response of sub-gap absorption, current extraction by a linear increasing voltage, etc.

3.3.1 Current-Voltage Characteristics under Illumination Conditions

The current-voltage characteristics under illumination are usually used for analysis of performance of the PV devices. From these measurements we can obtain information related with the open-circuit voltage (V_{oc}), short-circuit current (I_{sc}), fill factor (FF), and of course power efficiency (η). These parameters are commonly utilized to analyze and compare the performance of different PV devices. From I-V characteristics under illumination we can also obtain information related with some diagnostic characteristics: shunt ($R_{Sh-Light}$) and series ($R_{S-Light}$) resistances under illumination.

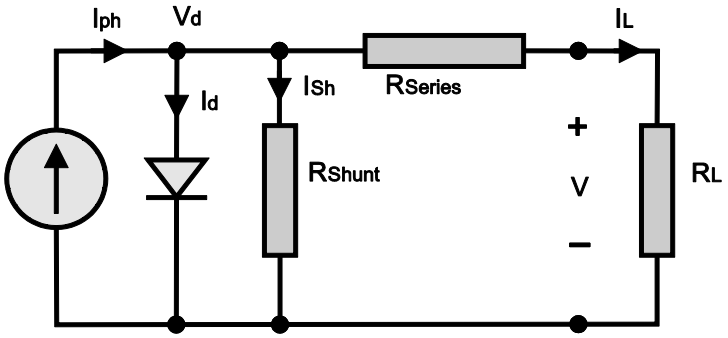

Figure 3.5: Electrical model used to represent the photovoltaic pin structures

In order to evaluate a real solar cell, in this work it was used the equivalent circuit model shown in Figure 3.5. The equivalent circuit model consists of a photocurrent generator, a diode, a shunt resistance, and a series resistance. Physically, series resistance provides us information related with the contact resistance or non-ohmic contacts, the bulk resistivity of the base layer, and spreading resistance in the thin front face layer. The shunt resistance provides us information related with shorts in the contact metallization around the junction, direct electrical short which arise at pinholes or micro cracks in the junction-forming layer. The diode provides us information related with the quality of the junctions. The current generator represents the current photo-generated in the bulk of the base layer.

3.3.1.1 Experimental Setup used in the Measurements of Current-Voltage Characteristics

The experimental setup used to perform the measurements of the current-voltage characteristics under illumination conditions is shown in Figure 3.6. The experimental setup consists of an electrometer (Model 6517A) from "Keithley Instrument Inc.", a light source with his respective source of voltage, a computer with their GPIB interface to control the electrometer, and a Low Temperature Micro Probe System (LTMP-2) from "MMR Technologies Inc." to place the sample.

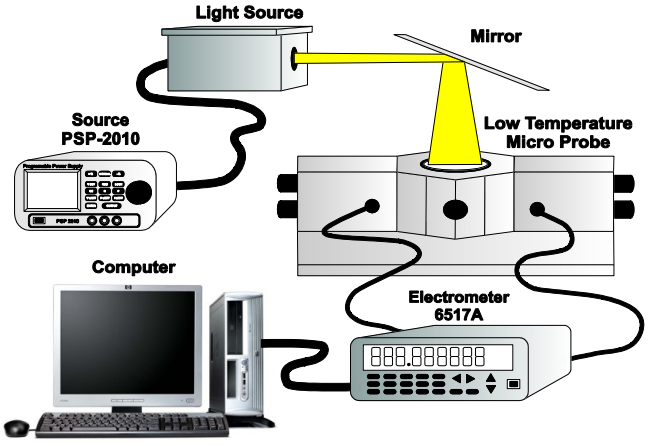

Figure 3.6: Experimental setup for the I-V characteristics under illumination conditions

The electrometer Keithley was configured as source of voltage and meter of current. The source of voltage can be varied from 0 to $\pm\ 100V$, with an accuracy of $\pm$ (0.15% setting $+\ 10mV$), and/or from 0 to $\pm\ 1000V$, with an accuracy of $\pm$ (0.15% setting $+\ 100mV$). The meter of current has a sensibility over a range from $20pA$ to $20mA$.

3.3.1.2 **Data Processing**

The current-Voltage characteristics under illumination conditions were measured at room temperature in the DC regime. The current-voltage characteristic measured under illumination conditions in the pm-Si:H pin structure is shown in Figure 3.7. From this current-voltage characteristic is possible to obtain the open-circuit voltage (V_{oc}) when $I = 0$ and the short-circuit current (I_{sc}) when $V = 0$ as is shown in Figure 3.7.

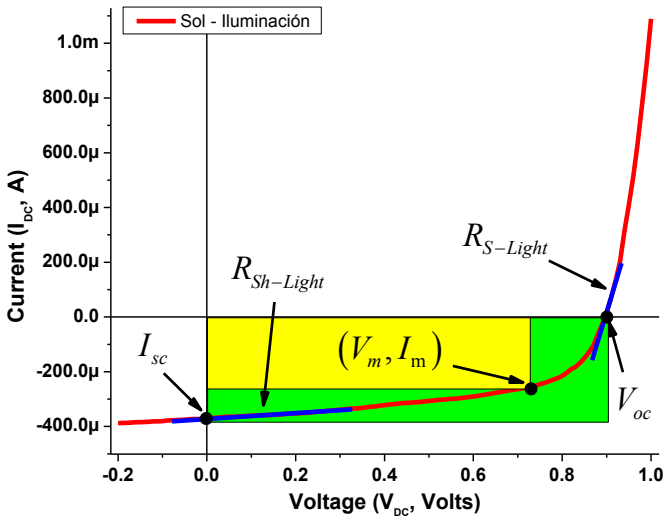

Figure 3.7: I-V characteristics measured under illumination conditions

The fill factor (FF) represents the ratio of the largest area rectangular that can be inscribed in the fourth quadrant of the I-V curve obtained under illumination to the area of the rectangle delimited by I_{sc}, V_{oc} and the I and V axes as shown in Figure 3.7. The value of the fill factor is calculated using the Equation (3.1).

$$FF = \frac{V_m I_m}{V_{oc} I_{sc}} \qquad [3.1]$$

The energy-conversion efficiency represents the ratio of the maximum power obtained from the photovoltaic device to the total power in the light incident on the photovoltaic device and is calculated using the Equation (3.2).

$$\eta = \frac{V_m I_m}{P_{in}} = \frac{V_{oc} I_{sc} FF}{P_{in}} \qquad [3.2]$$

In Equation (3.2) P_{in} is the total power in the light incident on the photovoltaic device. $V_m I_m$ is the maximum power obtained from the photovoltaic device.

$$R_{S-Light} = -\frac{dV}{dI} \quad at \quad I = 0 \qquad [3.3]$$

Using the equivalent circuit model shown in Figure 3.5 and the data of the current-voltage characteristics shown in Figure 3.7, the series resistance ($R_{S-Light}$) under illumination can be obtained using the Equation (3.3).

$$R_{Sh-Light} = -\frac{dV}{dI} \quad at \quad V = 0 \qquad [3.4]$$

In the same way, the shunt resistance ($R_{Sh-Light}$) under illumination can be obtained using the Equation (3.4).

3.3.2 Temperature Dependence of Current-Voltage Characteristics under Illumination Conditions

At present it is well know that the operation temperature of thin film solar cells can vary over wide extremes depending of the operation conditions. In terrestrial applications, they are generally exposed to temperatures ranging from 15℃ ($288K$) to 50℃ ($323K$) and to even higher temperatures in space and concentrator-systems. By this reason it is very important to understand the temperature dependence of current-voltage characteristics under illumination in photovoltaic devices. For example in crystalline solar cells it is observed commonly that the open-circuit voltage

approximately linearly decrease with increasing temperature due to the increasing recombination rate in the devices. On the other hand the short-circuit current is not strongly temperature-dependent but increase slightly with the increasing temperature. The fill factor depends on the value of the open-circuit voltage and decreases with increasing temperature. Therefore the energy-conversion efficiency of solar cells depends on the value of the fill factor and also decreases with increasing temperature. In non-crystalline solar cells the situation is more complex than in crystalline solar cells but the energy-conversion efficiency also decrease with the increasing temperature.

3.3.2.1 Experimental Setup used in the Measurements of Temperature Dependence of Current-Voltage Characteristics under Illumination

In Figure 3.8 is shown the experimental setup to measure the current-voltage characteristics under illumination at different temperatures. The experimental setup consists of a light source with his respective source of voltage, an electrometer (Model 6517A) from "Keithley Instruments Inc.", a Joule-Thompson refrigerator, a K-20 Programmable Temperature Controller, a computer with their GPIB interfaces to control the electrometer, and a Low Temperature Micro Probe System (LTMP-2) from "MMR Technologies Inc." to place the sample.

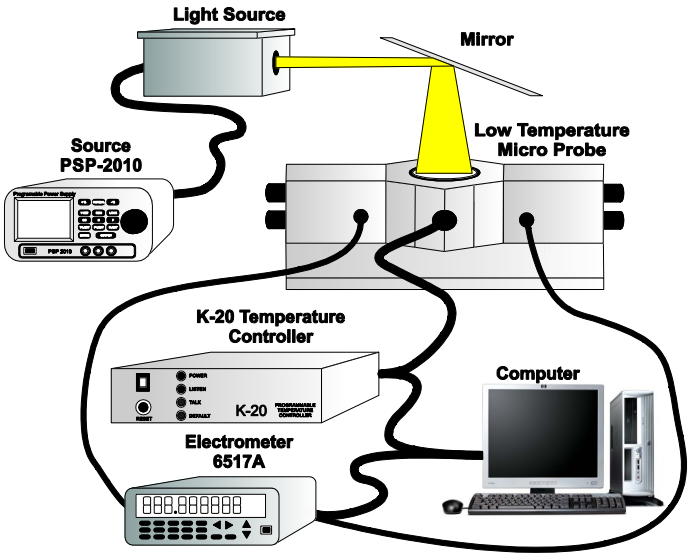

Figure 3.8: Experimental setup for the I-V characteristics with variable temperature

The K-20 Programmable Temperature Controller, when used MMR micro miniature refrigerators, provides controlled cycling and temperature measurement over a range from 20 to $400K$, with an accuracy of $\pm 0.5K$ and a stability of $\pm 0.05K$. In order to perform the experimental measurements, the sample was set in the vacuum chamber on the MMR´s micro refrigerator as is shown in Figure 3.9.

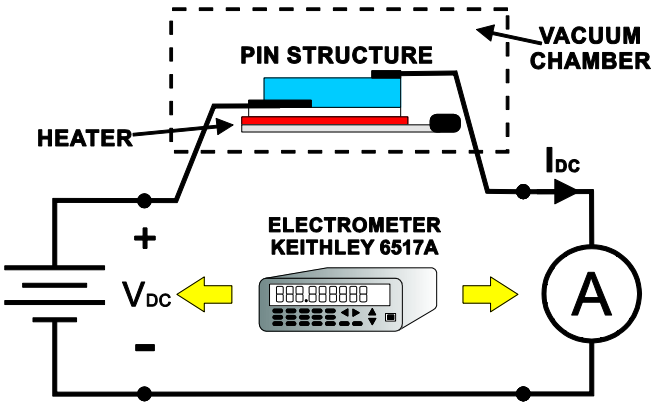

Figure 3.9: Electrical connection for the dark I-V measurements with various temperatures

In these measurements the electrometer Keithley was configured as source of voltage and meter of current. Before beginning the temperature dependence of current-voltage characteristics under illumination measurements the light source must have a space of 15 min to become stable.

3.3.2.2 **Data Processing**

In a solar cell, the parameter most affected by an increase in temperature is the open-circuit voltage. Figure 3.10 shows the characteristic behavior of the current-voltage characteristics in function of the operating temperature. This figure shows that the open-circuit voltage decreases with the increase of the operating temperature and short-circuit current increases with the increase of the operating temperature. From these current-voltage characteristics we can obtain information related to the performance characteristics: open-circuit voltage, short-circuit current, fill factor, and energy-conversion efficiency for each temperature as it was explained in section 3.3.1.2.

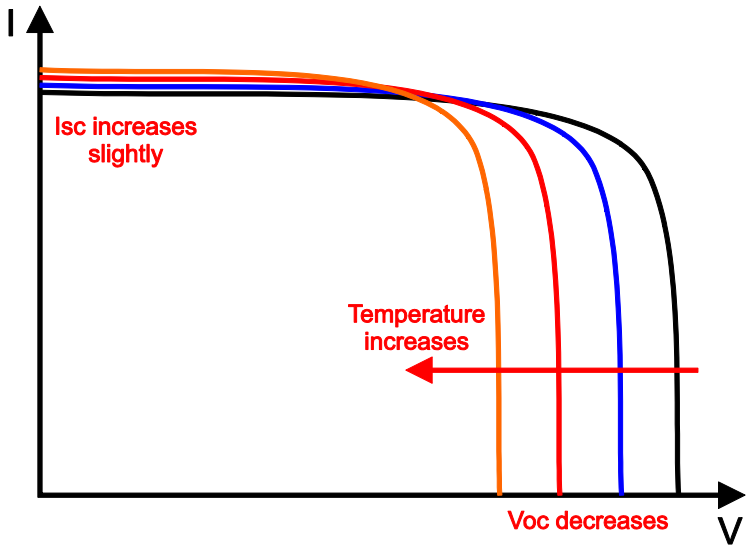

Figure 3.10: I-V characteristics under illumination as a function of operating temperature

Figure 3.11 shows the characteristic behavior of the (a) open-circuit voltage and (b) short-circuit current as a function of the operating temperature. In crystalline materials, the open-circuit voltage decreases with the increase of the operating temperature because the optical bandgap of semiconductor materials reduces with the increase of the operating temperature. The variation of the open-circuit voltage as a function of the operating temperature can be represented using the Equation (3.5).

$$\frac{dV_{oc}}{dT} = -\frac{V_{g0} - V_{oc} + \gamma\left(kT/q\right)}{T} \qquad [3.5]$$

Where $V_{g0} = E_{g0}/q$, E_{g0} is the value of the band gap of the semiconductor making up the solar cell linearly extrapolated at a zero temperature, and γ includes the temperature dependencies of the remaining parameters determining $I_0 = AT^{\gamma}e^{-E_{g0}/kT}$.

$$V_{oc} \approx \frac{E_{g0}}{q} + \frac{dV_{oc}}{dT} * T \quad for \quad \frac{E_{g0}}{q} >> \frac{kT}{q} \qquad [3.6]$$

From Equation (3.5) we can obtain an approximate value of E_{g0} taking into account that the value of $E_{g0} \gg kT$ as is shown in Equation (3.6).

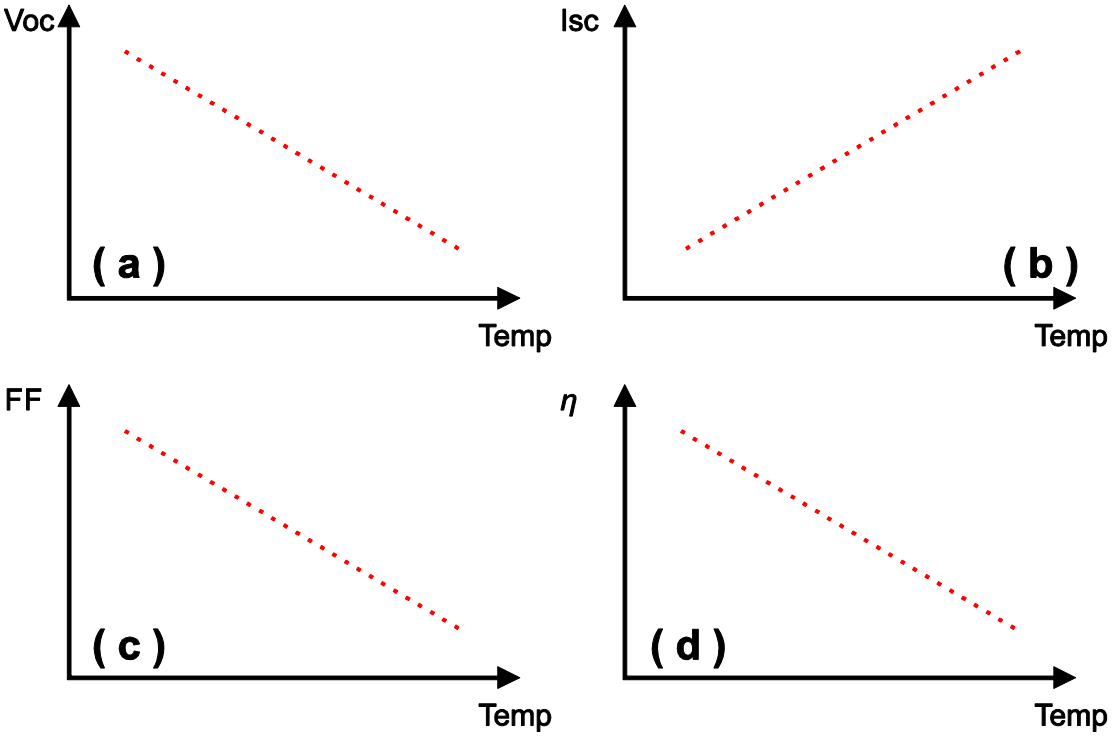

Figure 3.11: Shows the (a) open circuit voltage, (b) short-circuit current, (c) fill factor, and (d) energy conversion efficiency behavior as a function of the operating temperature

The short-circuit current of solar cells is not strongly temperature-dependent but increases with the increase of the operating temperature because the optical bandgap decreases with the increase of temperature. A smaller optical bandgap enhances the absorption coefficient and increases the current in solar cells. Figure 3.11(c) shows the characteristic behavior of the fill factor as a function of the operating temperature. In crystalline materials, the variation of the fill factor as a function of the operating temperature can be represented using the Equation (3.7).

$$FF = \frac{u_{oc} - \ln\left(u_{oc} - 0.72\right)}{u_{oc} + 1} \qquad [3.7]$$

Where $u_{oc} = V_{oc}/(nkT/q)$. In the Equations (3.5), (3.6), and (3.7) is considered that in a solar cell the shunt and series resistances do not vary strongly with the temperature and that only the recombination in the depletion region reduces the open-

circuit voltage, the short-circuit current, the fill factor, and of course energy-conversion efficiency. Finally, in Figure 3.11(d) is shown the characteristic behavior of the energy-conversion efficiency as a function of the operating temperature.

3.3.3 **Spectral Response of Short-Circuit Current**

Spectral characteristics are very important to develop the performance and technology of solar cells. By means of the relative spectral response measurements we can obtain information about the quality of the intrinsic bulk semiconductor region in which the light absorption and photo-generation of free charge carriers takes place, information related with the density of the states, information related with the interfaces of the intrinsic semiconductor region, etc. In a solar cell, we can measure the spectral response of the short-circuit current, the spectral response of the open-circuit voltage, or the spectral response at the maximum power delivered by the solar cell and obtain different information on each spectral measurement. In this thesis was used the spectral response of the short-circuit current due to the short-circuit current has an approximately linear dependence with the intensity of the light beam used in the spectral measurements. The spectral response of short-circuit current is not very complex experimentally but it is a powerful tool to development the PV devices performance. By changing the energy of the photons that make up the light beam we can control the region where the photon absorption takes place. For example, if the photon energy (E_{photon}) is higher than the optical gap (E_{opt}) the absorption takes place near to the interface of the intrinsic region but if the photon energy is $E_{photon} \approx E_{opt}$ the absorption takes place in the bulk of the intrinsic semiconductor.

$$SR = \frac{q\lambda}{hc} QE \qquad [3.8]$$

The spectral response is conceptually similar to the quantum efficiency. The quantum efficiency gives the number of electrons output by the solar cell compared to the number of photons incident on the device, while the spectral response is the ratio

of the current generated by the solar cell to the power incident on the solar cell. The quantum efficiency can be determined from the spectral response by replacing the power of the light at a particular wavelength with the photon flux for that wavelength as is shown in Equation (3.8).

3.3.3.1 Experimental Setup used in the Measurements of the Spectral Response of Short-Cicuit Current

The experimental setup used in the measurements of the spectral response of short-circuit current technique is shown in Figure 3.12. The spectral measurements were performed in the DC regime. The experimental setup consists of a programmable power supply from "Good Will Instrument Co., Ltd.", a xenon lamp and a halogen lamp from "Jovin Yvon Inc.", a monochromator (Model TRIAX320) from "Jovin Yvon Inc.", an electrometer (Model 6517A) from "Keithley Instruments Inc.", a thermopile sensor (Model 71938) from "Thermo Oriel Instruments Inc.", and a Low Temperature Micro Probe System (LTMP-2) from "MMR Technologies Inc." to set the sample.

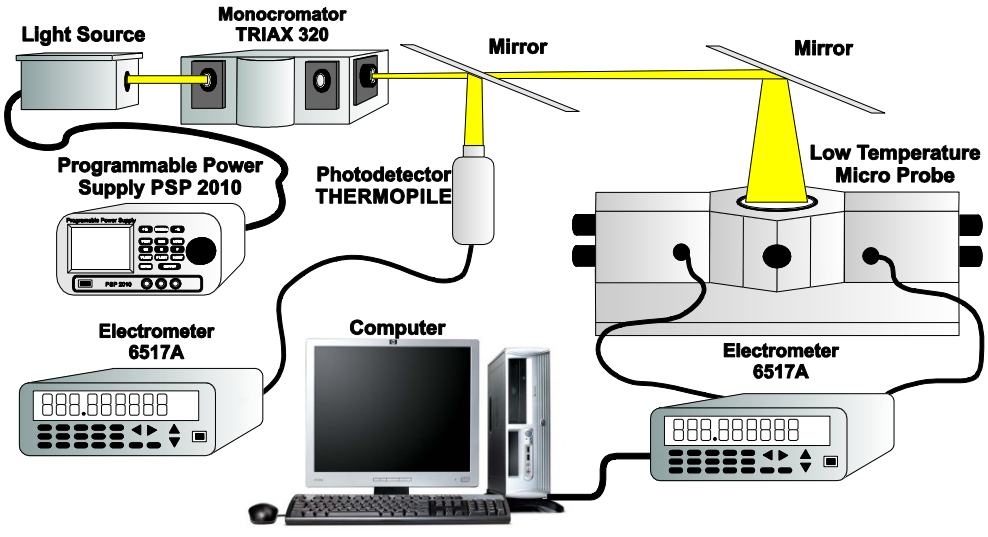

Figure 3.12: Experimental setup used in the measurements of the spectral characteristics technique

The experimental setup of the spectral measurements allows us to measure the spectral characteristics over a range from $\lambda = 0.31\ \mu m$ $(hv \approx 4eV)$ to $\lambda = 2.5\ \mu m$ $(hv \approx 0.49eV)$ with a resolution of $\Delta\lambda = 0.01\ \mu m$. In Figure 3.13 is shown the electrical connection of the experimental setup. In order to measure the spectral characteristics of short-circuit current the electrometer Keithley 6517A must be configured as a meter of current (see Figure 3.12 and Figure 3.13). In order to measure the spectral characteristics of the open circuit voltage the electrometer must be configured as a meter of voltage. In order to measure the spectral characteristics of fill factor and energy-conversion efficiency the electrometer must be configured as a source of voltage and meter of current.

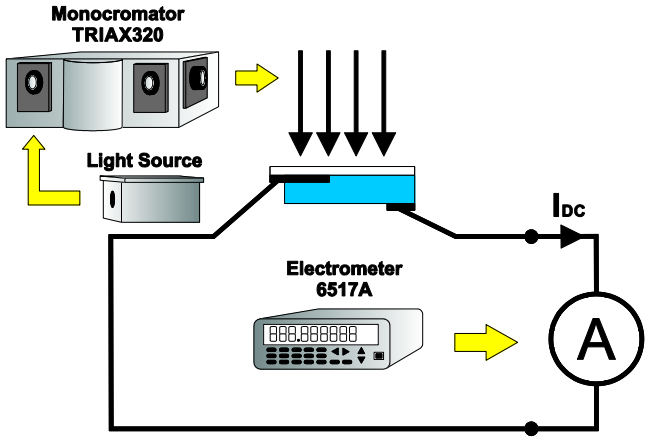

Figure 3.13: Electrical connection of the experimental setup of the spectral measurements technique

The xenon lamp is a polychromatic light source with an integral power of $300W$. Using this light source is possible to obtain a monochromatic light beam with an intensity of $I_0 = 30\ mW/cm^2$ and a dispersion of $\Delta\lambda = 5.28\ nm$. The intensity of the monochromatic light beam was measured with the thermopile sensor. The thermopile 71938 has a sensibility of $S = 260\ \mu A/W$ and an active area of $A_{Th} = 2.8x10^{-3}\ cm^2$. The monochromator was utilized to select the wavelength of the monochromatic light beam. The measurements were done in dark conditions on an optical table with vibration protection.

3.3.3.2 **Data Processing**

During the spectral measurements the wavelength of the monochromatic light beam was varied from $\lambda = 0.33$ to $1.2\,\mu m$ with a resolution of $\lambda = 0.01\,\mu m$. The measurements were done in the DC regime at room temperature. Before beginning the spectral measurements, the light source must have a space of $15\,min$ to become stable. In Figure 3.14 is shown the spectral response measured on a pm-Si:H PIN structure. This spectral response is composed by two components: the first one is the spectral characteristic of the sample and the second one is the spectral response of the optical part of the experimental setup. The optical part of the experimental setup consists of a halogen lamp ($P_{out} = 100W$), mirrors, lens and a monochromator TRIAX320 with its respective filter wheel and gratings.

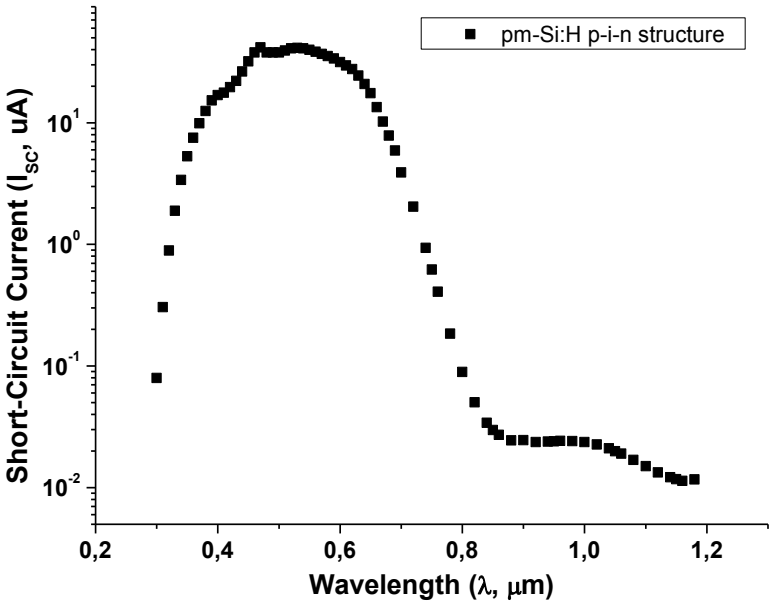

Figure 3.14: Spectral response measured on pm-Si:H PIN structure

In Figure 3.15 is shown the spectral response radiated by the optical part of the experimental setup utilizing a (a) xenon and a (b) halogen lamp for visible and near infrared region, respectively. The light beam intensity was measured for each wavelength using the thermopile sensor from "Thermo Oriel Instruments Inc.".

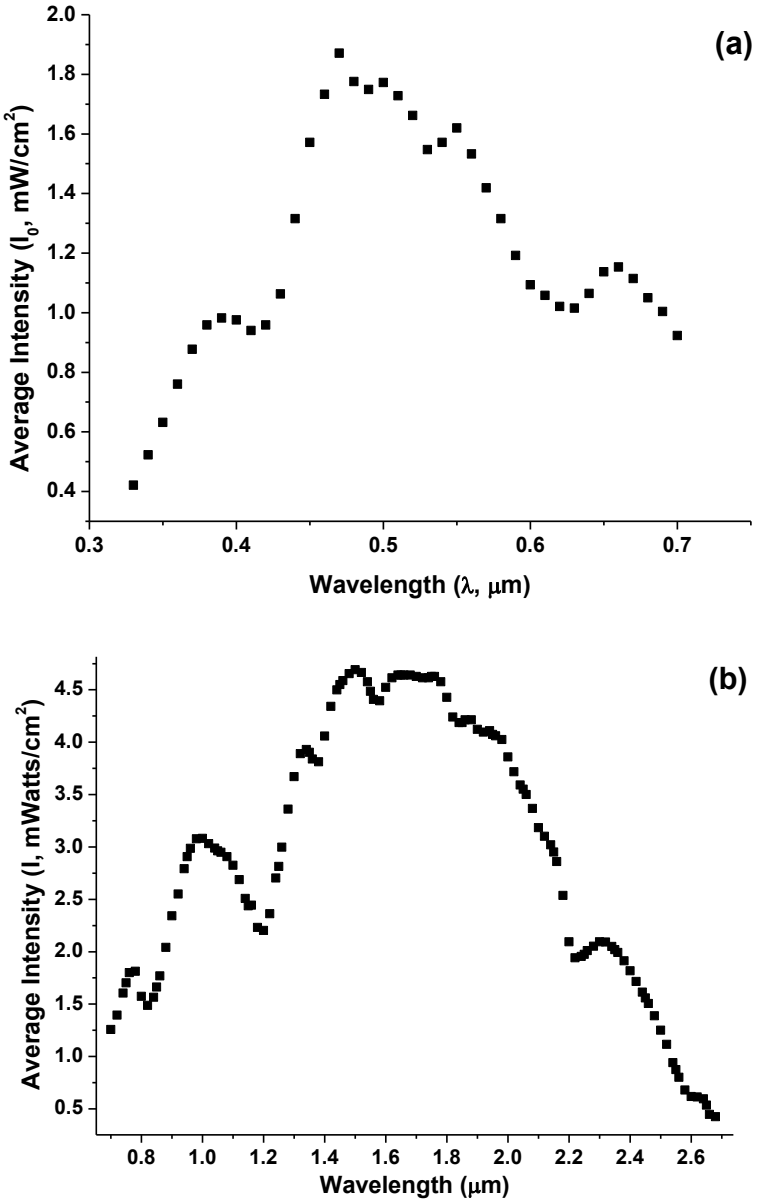

Figure 3.15: Spectral response of the experimental setup measured for (a) visible and (b) near infrared region

Before obtaining the spectral characteristics of the photovoltaic device it is necessary to check if the short-circuit current has a linear dependence with the intensity ($I_{sc}(\lambda) \propto I_0^{\gamma}(\lambda), \gamma = 1$) for each wavelength over a range from $\lambda = 0.33$ to $1.2\ \mu m$. If there is a linear dependence with the intensity ($\gamma \approx 1$), the spectral characteristics can be obtained using the Equation (3.9).

$$I_{sc}(\lambda)_{I_0=Cte} = \frac{I_{sc-Primary\_data}(\lambda)}{S^{I_0}_{Experimental\_Setup}(\lambda)} \quad [3.9]$$

In Equation (3.9), $S^{I_0}_{Experimental\_Setup}(\lambda)$ represents the spectral response of the optical part of the experimental setup (see Figure 3.15) and $I_{sc-Primary\_data}(\lambda)$ represents the spectral response measured in the sample (see Figure 3.14). In Figure 3.16 is shown the spectral response of short-circuit current measured in a pm-Si:H PIN structure. The spectral characteristic of short-circuit current is normalized to a constant intensity of $I_0 \approx 1.6\, mW/cm^2$.

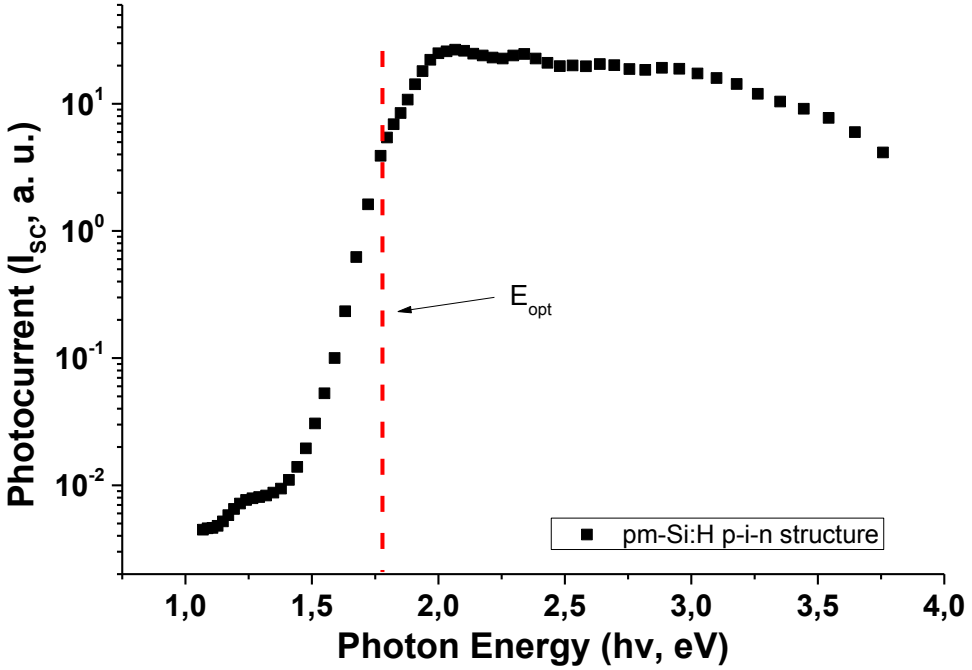

Figure 3.16: Spectral characteristics of Short-Circuit Current normalized to a constant intensity of $I_0 = (1.64 \pm 0.01) * 10^{-3} W/cm^2$)

The dash line in Figure 3.16 represents hypothetically the value of the optical bandgap of the pm-Si:H Thin Films which constitute the photovoltaic device.

$$E_{photon}[h\nu,\ eV] = \frac{1.24}{\lambda[\mu m]} \quad [3.10]$$

The photon energy was calculated from wavelength using the Equation (3.10) in which $\lambda[\mu m]$ represents the value of the wavelength shown in Figure 3.14.

$$SR = \frac{I_{sc}(hv_1)}{I_{sc}(hv_2)} \quad where \quad hv_1 < hv_2 \qquad [3.11]$$

From the spectral response of the short-circuit current (see Figure 3.16), we can obtain information related to the diagnostic ($hv < E_{opt}$) and performance ($hv \geq E_{opt}$) characteristics. The information related to the diagnostic characteristics will be described in Section 3.3.6. The ratio of surface recombination (diagnostic characteristic) was extracted using the Equation (3.11). The ratio of surface recombination (S_r) gives us information related with the photon absorption near to the interfaces of the photovoltaic device ($hv_2 \approx 3.8eV$).

3.3.4 Temperature Dependence of Spectral Response of Short-Circuit Current

As it was mentioned in the previous section, the spectral response of short-circuit current is a very important tool to develop the performance characteristics of photovoltaic. By changing the operating temperature of photovoltaic devices, the spectral response of the short-circuit current allows us to obtain information about the quality of the intrinsic bulk semiconductor region, information about the density of the states, and information related with the interfaces of the intrinsic bulk semiconductor region in function of the operating temperature.

3.3.4.1 Experimental Setup used in the Measurements of Temperature Dependence of Spectral Response Short-Circuit Current

The experimental setup used in the measurements of the temperature dependence of performance characteristics is shown in Figure 3.17. The experimental setup consists of a programmable power supply from "Good Will Instrument Co., Ltd.", a xenon and a halogen lamp from "Jovin Yvon Inc.", a monochromator (Model TRIAX320) from "Jovin Yvon Inc.", an electrometer (Model 6517A) from "Keithley Instruments Inc.",

a thermopile sensor (Model 71938) from "Thermo Oriel Instruments Inc.", , a Joule-Thompson refrigerator, K-20 Programmable Temperature Controller and a Low Temperature Micro Probe System (LTMP-2) from "MMR Technologies Inc." to set the sample.

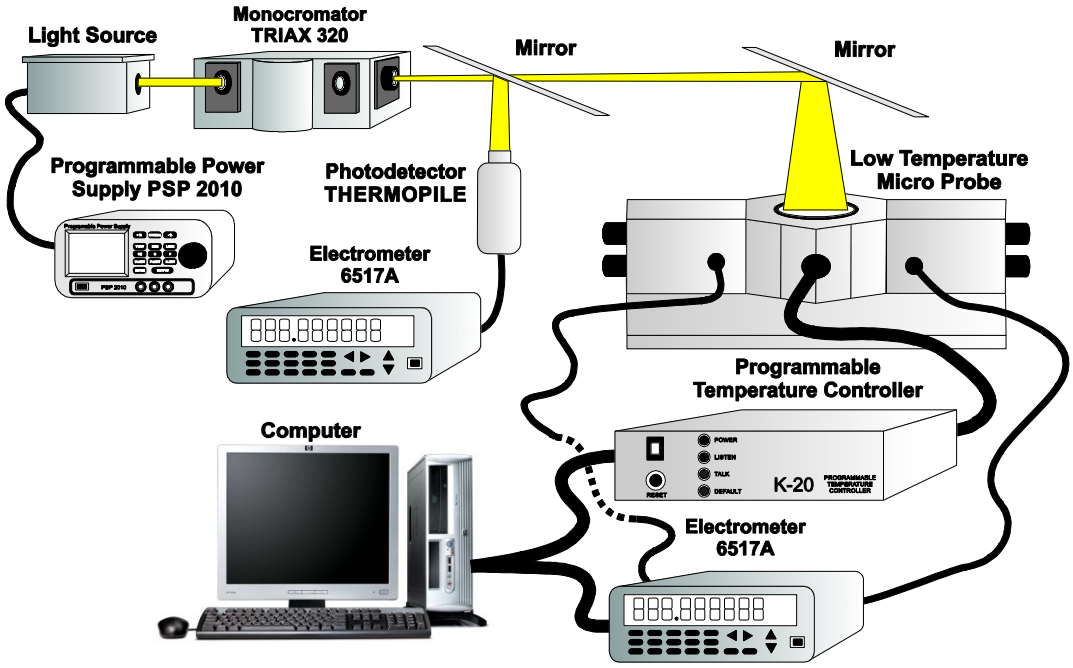

Figure 3.17: Experimental Setup used in the measurements of the Temperature Dependence of Performance Characteristics

The experimental setup of the temperature dependence of performance characteristics allows us to vary the operation temperature of the devices over a range from 20 to $400K$ and measure the spectral characteristics over a range from $\lambda = 0.31\,\mu m$ $(hv \approx 4eV)$ to $\lambda = 2.5\,\mu m$ $(hv \approx 0.49eV)$ with a resolution of $\Delta\lambda = 0.01\,\mu m$. In the temperature dependence of spectral characteristics measurements the electrometer 6517A is configured as meter of current. The optoelectronic characteristics as a function of the operating temperature were extracted using the methodologies described in Sections 3.3.3 and 3.3.6.

3.3.5 **Dark Current-Voltage Characteristics**

Dark current-voltage characteristics are not complex but they are a very important tool that help us to identify and understand some problems related with the fabrication technology. For example, problems related with the quiality of the junctions, non-ohmic contacts metal-semiconductor, spreading resistance in the thin front face layer, the bulk resistivity of the base layer, shorts in the contact metallization and direct electrical shorts as it was explained in the section 2.3.6. Problems which are very common in junctions with non-crystalline semiconductors.

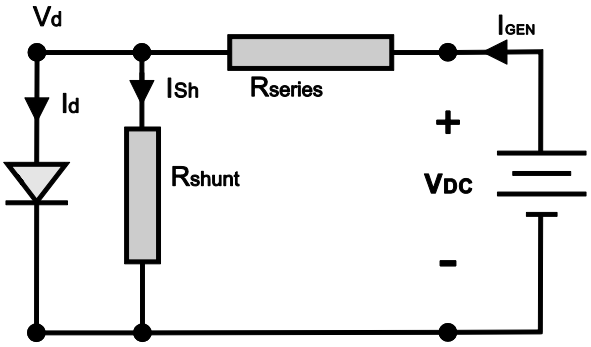

Figure 3.18: Electrical model used to represents the photvoltaic PIN structure without illumination

In order to study and analyze the problems related to the fabrication technology of photovoltaic devices, it was used the electrical model shown in Figure 3.18. The electrical model consists of an ideal diode (n_d), a shunt (R_{Sh}) and a series (R_s) resistance (diagnostic characteristics). This model is very single but give us information related with the problems mentioned above.

$$I_{GEN} = I_0 \exp\left[\frac{q\left(V - I_{GEN}R_s\right)}{nkT}\right] + \frac{V + I_{GEN}R_s}{R_{Sh}} \qquad [3.12]$$

Equation (3.12) shows the analytic expression used to describe the behavior of the current-voltage characteristics of the electrical model shown in Figure 3.18. R_s and R_{Sh} represent the series and Shunt resistances, and n represents the diode ideality factor of the photovotaic device.

3.3.5.1 Experimental Setup used in the Measurements of the Dark Current-Voltage Characteristics

The experimental setup used to perform the measurements of the dark current-voltage characteristics is shown in Figure 3.19. The experimental setup consists of an electrometer (Model 6517A) from "Keithley Instrument Inc.", a computer with their GPIB interface to control the electrometer, and a Low Temperature Micro Probe System (LTMP-2) from "MMR Technologies Inc." to place the sample.

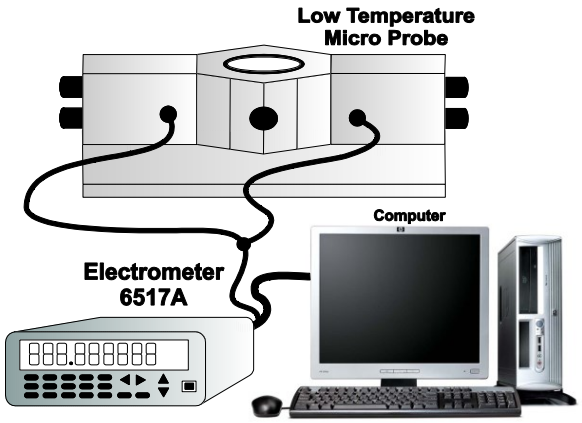

Figure 3.19: Experimental setup used for the Dark Current-Voltage characteristics

To control the equipment of measurements it is used a graphical interface developed in LabWiew programming software.

3.3.5.2 Data Processing

In Figure 3.20 is shown the dark current-voltage characteristics measured at room temperature on the pm-Si:H photovoltaic PIN structure. The dark current-voltage characteristics are conformed by two regions: the first one (black squares) related to the data measured with forward bias polarization and the second one (red circles) related to the data measured with reverse bias polarization. For the study of the current-voltage characteristics, in this thesis work only be considered the forward polarization region.

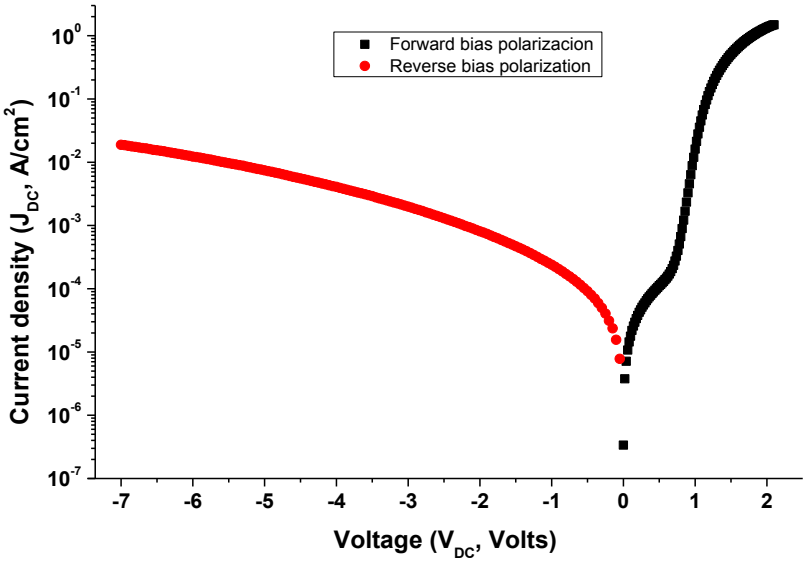

Figure 3.20: Dark current-voltage characteristics measured in the pm-Si:H PIN photovoltaic structure at room temperature

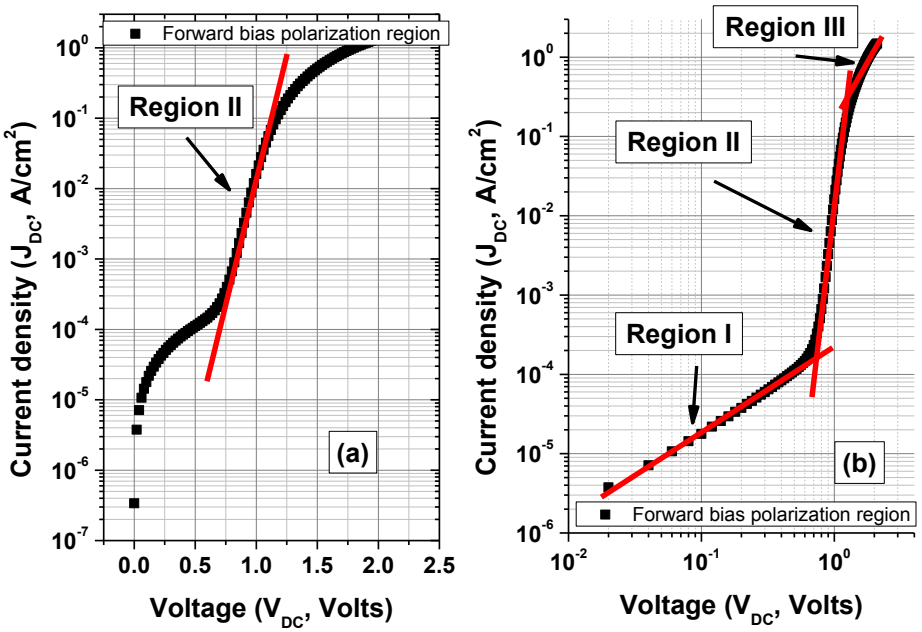

Figure 3.21: Presentation of primary data for the analysis of the 3 regions

In Figure 3.20 and Figure 3.21, we can see that in the forward bias region there are three main regions. Figure 3.21(a) shows the region II, which corresponds to the characteristic curve of an ideal diode (dark I-V characteristics) with forward bias. In this region, the current-voltage characteristics can be modeled using Equation (3.13).

$$J(V) \approx J_S \left[\exp\left(\frac{qV}{nkT}\right) - 1 \right] \approx J_S \exp\left(\frac{qV}{nkT}\right) \qquad [3.13]$$

In Equation (3.13) n represents the diode ideality factor and J_s represents the saturation current density of the diode. Figure 3.21(b) shows the current-voltage characteristics of the photovoltaic p-i-n structure plotted on $\log(I)\ vs\ \log(V)$ scale. In Figure 3.21(b) is shown that the behavior of the current-voltage characteristics in Region I is similar to the behavior observed in a resistor (Shunt resistance). Region III in Figure 3.21(b) shows the influence caused by the series resistance of the photovoltaic p-i-n structure.

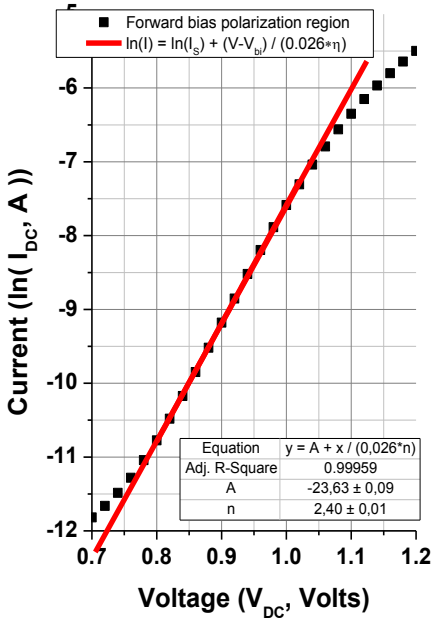

Figure 3.22: Analysis of data from the region II

To perform the data analysis of the region II of the current-voltage characteristics, the raw data were plotted on $\ln(I)\ vs\ V$ scale. Later, using the Equation (3.14) it was performed the analys is shown in Figure 3.22. At room temperature ($T = 300°K$) the constants kT/q has a value of $kT/q \approx 0.026eV$.

$$\ln(J) = \ln(J_s) + \frac{q(V - V_{bi})}{nkT} \qquad [3.14]$$

The results of the data analysis indicated that the diode has an ideality factor of $n = 2.4 \pm 0.1$ and the density of the saturation current has a value of $J_s = (1.7 \pm 0.4) * 10^{-9}[A/cm^2]$.

$$(a) \quad \ln(I_{DC}) = \ln(R_{Sh}) + b * \ln(V_{DC})$$
$$(b) \quad I_{DC} = \frac{V_{DC}}{R_{Sh}} \qquad [3.15]$$

To analyze the region I, first it was checked if this region can be modeled using the Ohm's law. To check the Ohm's Law the raw data were plotted on $\ln(I)$ vs $\ln(V)$ scale. After, it was performed the data analysis using the Equation (3.15)-(a) as is shown in Figure 3.23(a). The results obtained in this data analysis indicated that this region satisfies the requirements of the Ohm's law ($b = 1.09 \pm 0.01$).

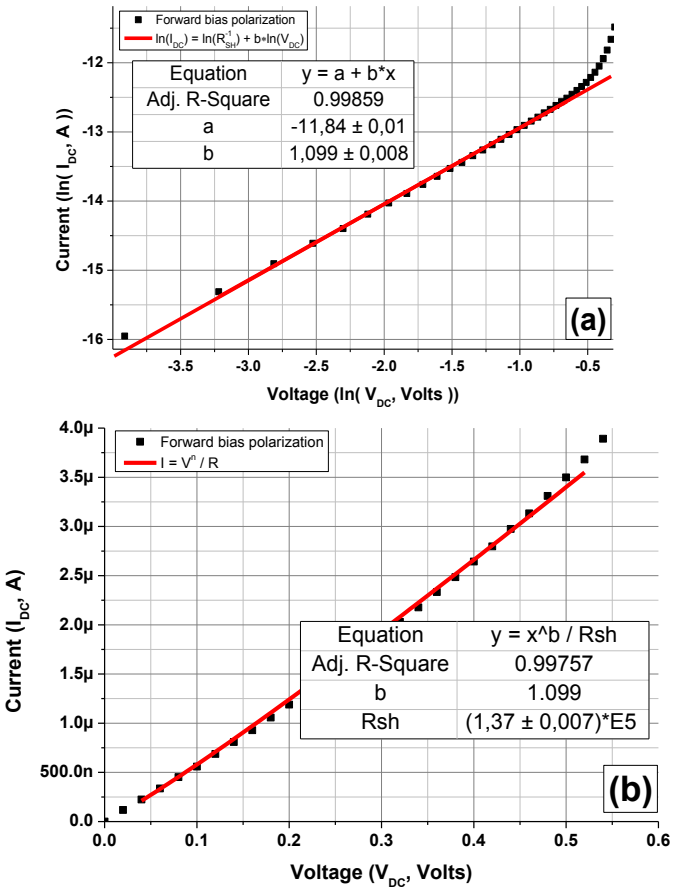

Figure 3.23: Analysis of data from the region I

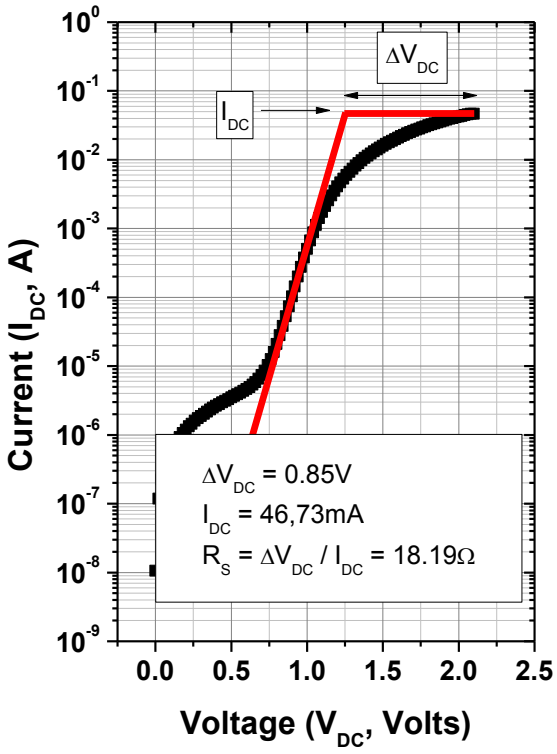

Figure 3.24: Analysis of data from the región III

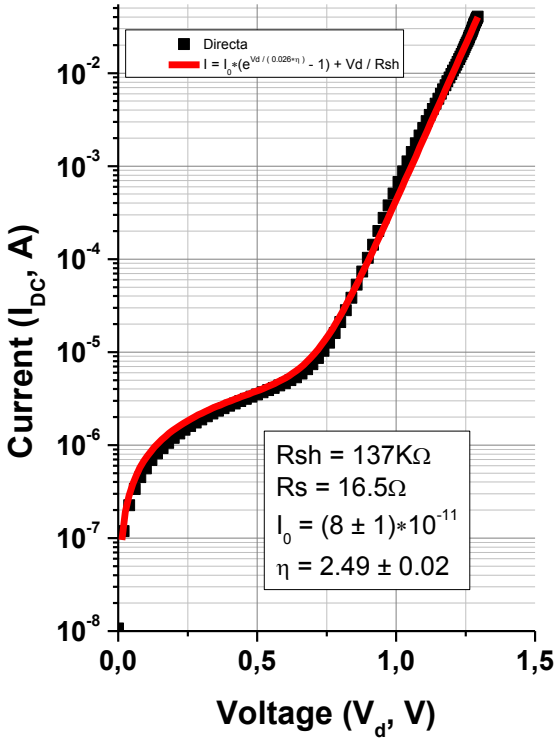

Figure 3.25: Processing of data to check if the values of the R_{Sh}, R_s, I_0, and n are corrects

After verifying the Ohm's law, it was obtained the value of the shunt resistance using the Equation (3.15)-(b). The results shown that the shunt resistance has a value of $R_{Sh} = (1.373 \pm 0.007) * 10^5[\Omega]$ as is shown in Figure 3.23.

To analyze the region III, it was calculated the deviation caused by the series resistance of the device. To calculate the deviation, the raw data were plotted on $ln(I)\ vs\ V$ scale and then two lines were drawn as is shown in Figure 3.24. This line over the region II represents the behavior of the device without the effect of the series resistance and the line parallel to the voltage axis represents the deviation generated by the series resistance. Using the Equation (3.16) was obtained a value for the series resistance of $R_s = 18.19\Omega$ as is shown in Figure 3.24.

$$R_S = \frac{\Delta V_{DC}}{I} \qquad [3.16]$$

Finally, in order to check if the parameters obtained were correctly adjusted was performed the adjustment of data showed in Figure 3.25. Equation (3.17) describes the behavior of the model of Figure 3.18 and the adjustment of Figure 3.25.

$$I = I_0\left(\exp\left(\frac{V_d}{nkT}\right)-1\right)+\frac{V_d}{R_{sh}} \quad donde \quad V_d = V - IR_s \qquad [3.17]$$

To perform the adjustment of data shown in Figure 3.25 was fixed the value of Shunt resistance and the value of the series resistance was changed till obtain the best fit.

3.3.6 **Spectral Response of Sub-gap Absorption**

In Figure 3.16 (see section 3.3.3) is possible to observe that the spectral characteristics of short-circuit current can be divided in two section. The first one is due to band-to band transitions that correspond to the transitions from valence to conduction band. In this region the photon energy is higher than the optical bandgap ($hv > E_{opt}$). The second one (sub-gap absorption) is due to transitions related to valence and conduction band tails and defect related transitions. In this region the photon energy is lower than

the optical bandgap ($hv < E_{opt}$). In this section we will emphasize on the second section which is used to characterize the structural disorder in non-crystalline materials by means of the parameters E_{Upc} and R_{def}. In Figure 3.26 is shown the data related to sub-gap absorption region. In sub-gap absorption region (see Figure 3.26) two regions with different behavior can be distinguished: the first one (Region A) related to transitions between band tails and the second one (Region B) related to transitions from defect states.

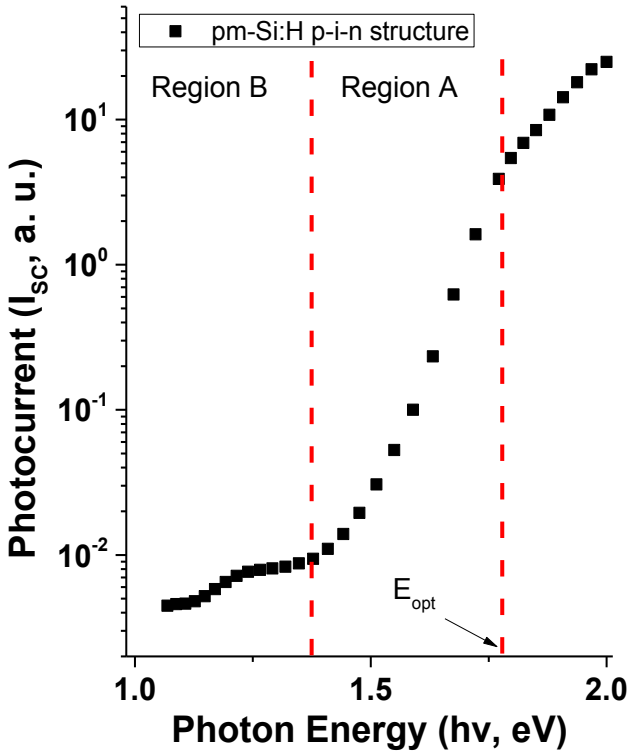

Figure 3.26: Sub-gap absorption region of the spectral characteristics measured on the pm-Si:H PIN photovoltaic structure

The parameter E_{Upc} (diagnostic characteristic) is extracted from the spectral response of sub-gap photoconductivity (Region A) using the Equation (3.18). This Equation is similar to the Equation used to extract the Urbach Energy E_U from the optical absorption spectra $\alpha(hv)$. The parameter E_{Upc} give us information related to the density of states in the valence-band tail.

$$I_{ph}(h\nu) = I_{ph_0} \exp\left(\frac{h\nu - E_{opt}}{E_{Upc}}\right) \quad [3.18]$$

In Equation (3.18) E_{opt} represents the optical bandgap, I_{ph_0} represents the photocurrent at $h\nu = E_{opt}$ and $h\nu$ is the photon energy.

$$R_{def} = \frac{I_{ph}(\mathrm{hv} = 0.8\,\mathrm{eV})}{I_{ph}(\mathrm{hv} = \mathrm{E_{opt}})} \quad [3.19]$$

The defects ratio (diagnostic characteristic) was calculated from the spectral response of sub-gap photoconductivity (Region B) as the ratio of photoconductivity at $h\nu = E_{opt}$ to photoconductivity at $h\nu = 0.8eV$ that corresponds to deep defects R_{def}.

Chapter 4

Experimental Results

4.1 Introduction

In order to show the study of the optoelectronic properties of photovoltaic devices, the results obtained in this study were grouped into three different sections. The first section shows the study of the a-$Ge_{0.97}Si_{0.03}$:H intrinsic film. In this study the deposition temperature was reduced from $T_s = 300$ to 70℃. The RF power, operating frequency, pressure, gas composition, magnitude and pattern of the gas flow remained constant. The results obtained in this section showed that is possible to reduce the deposition temperature from $T_s = 300$ to 70℃ and obtain intrinsic films of a-$Ge_{0.97}Si_{0.03}$:H with similar electronic properties. The second section shows the development of the photovoltaic devices fabricated at the installations of INAOE. The performance characteristics considered in development of the photovoltaic devices were: the energy-conversion efficiency of the photovoltaic device (η), the fill factor (FF), the open circuit voltage (V_{oc}), the short circuit current (I_{sc}), and the spectral response of short-circuit current $I_{sc}(hv > E_{opt})$. The diagnostic characteristics considered in the development of the photovoltaic devices were: the shunt ($R_{Sh-Light}$) and series ($R_{S-Light}$) resistance under illumination conditions, the surface recombination (S_r) in p-i interface, the spectral response of short-circuit current ($I_{sc}(hv < E_{opt})$), the diode

ideality factor (n), the saturation current (I_s), the shunt ($R_{Sh-Dark}$) and series (R_{S-Dark}) resistance under dark conditions, the parameter E_{Upc}, and the defect ratio (R_{def}). The third section shows a comparison and diagnostic of the photovoltaic devices fabricated with different semiconducting materials. In order to obtain information about data processing and the methodologies used to extract the parameters mentioned above, the reader should review Chapter 3: Methodologies and Characterization techniques.

4.2 Effect of the Deposition Temperature on the Electronic Characteristics of Sub-gap photoconductivity of the Intrinsic $Ge_{0.97}Si_{0.03}$:H Thin Films

Spectral responses of photoconductivity for $Ge_{0.97}Si_{0.03}$:H thin films deposited by LF PECVD at different substrate temperature are shown in Figure 4.1. Spectral responses were measured at the same light intensity. In these graphs we can distinguish two different regions: the first one (Region I) from $hv = 1.2$ to $1.77eV$ which is related to transitions between extended states (band-to-band transitions) and the second one (Region II) from $hv = 0.82$ to $1.2eV$ which is related to transitions between localized and extended states (sub-gap absorption). The optical gap of these $Ge_{0.97}Si_{0.03}$:H thin films ($E_g \approx 1.2eV$) could be deduced from the transition between Region I and Region II as is shown in Figure 4.1.

As we can see in region I and region II the spectral response of photoconductivity changes significantly (about one order of magnitude) in the samples deposited at different substrate temperatures T_s. The changes observed in these spectral responses do not demonstrate monotonous correlations. Region II (sub-gap absorption) is shown in Figure 4.2.

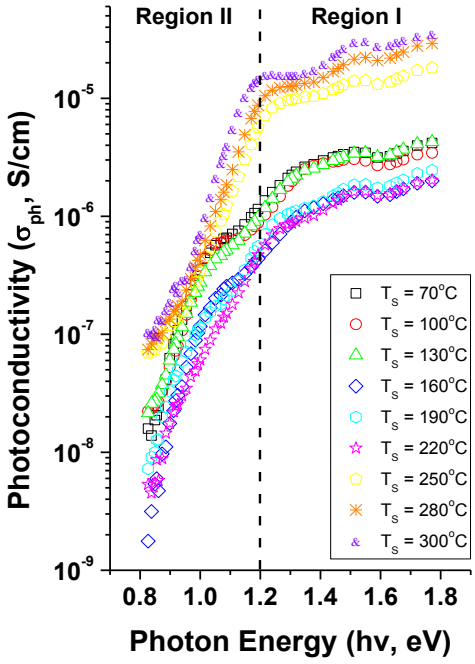

Figure 4.1: Spectral response of photoconductivity for a-$Ge_{0.97}Si_{0.03}$:H films deposited by LF PECVD at different substrate temperatures (Ts). Regions I and II are related to extended and localized states, respectively

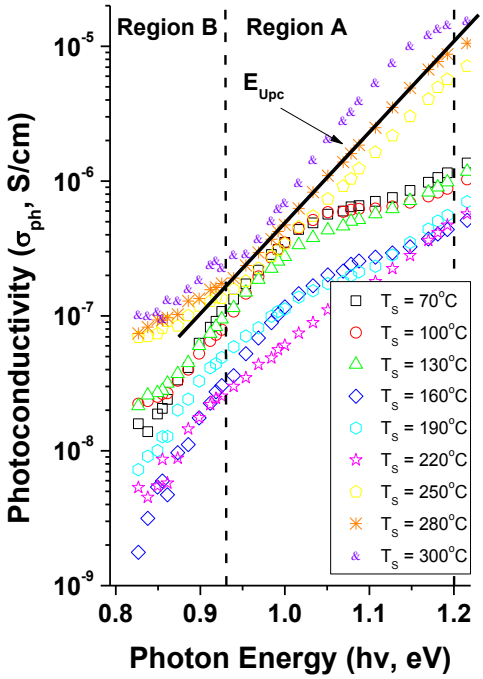

Figure 4.2: Sub-gap photoconductivity spectra for a-$Ge_{0.97}Si_{0.03}$:H films deposited by LF PECVD at different substrate temperatures (Ts). Regions "A" and "B" are related to band tail, and defect absorption, respectively

In sub-gap absorption in region II two regions with different behavior can be distinguished: the first one (Region A) related to transitions between band tails and the second one (Region B) related to transitions from defect states. In order to characterize the spectral response of sub-gap photoconductivity we used the slope E_{Upc} of the curves near to the optical gap energy (region A) which was determined in a similar way as Urbach energy E_U for optical absorption spectra $\alpha(hv)$ and the defect ratio of photoconductivity (Region B) which was calculated as the ratio of photoconductivity at $hv = E_g$ to photoconductivity at $hv = 0.8eV$ that corresponds to deep defects, R_{def}. The behavior observed of E_{Upc} as a function of substrate temperature is shown in Figure 4.3. The curve shown in Figure 4.3 reveals that the parameter E_{Upc} increases from 53.2 to $93.4meV$ as the substrate temperature reduces from $T_s = 300$ to 220℃ suggesting that the structural disorder increases and then reduces from 93.4 to $51.9meV$ as the substrate temperature reduces from $T_s = 220$ to 70℃ suggesting that the structural disorder related to band tails improves.

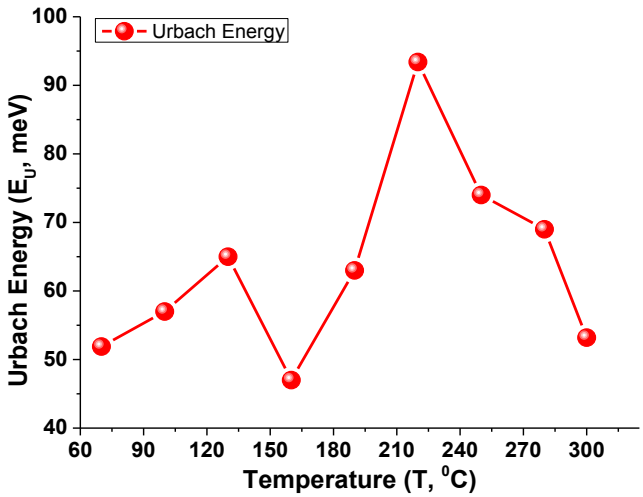

Figure 4.3: Urbach Energy obtained from sub-gap photoconductivity versus substrate temperature deposition

This tendency shows that there is no continuous change of the properties of the a-$Ge_{0.97}Si_{0.03}$:H films with reducing the substrate temperature from $T_s = 300$ to 70℃. The minimum value of $E_{Upc} = 47meV$ obtained at $T_s = 160$℃ means that the films deposited at this substrate temperature show minimal structural disorder reflected in the photoelectrical properties of the a-$Ge_{0.97}Si_{0.03}$:H thin films.

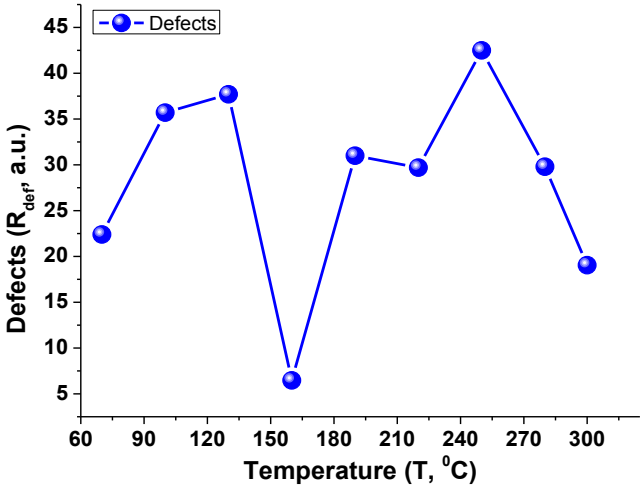

Figure 4.4: Defects ratio obtained from sub-gap photoconductivity versus substrate temperature deposition

On the other hand, the non-monotonous behavior observed for the defect ratio shown in Figure 4.4 reveals minimum of defects $R_{def} = 6.47$ in the same samples. The values obtained for the defect ratio show that the density of defects inside the optical gap increases from $R_{def} = 19.05$ to 42.4 as the deposition temperature reduces from $T_s = 300$ to 250℃ and then slightly changes in the range from 250 to 200℃. It is interesting that the samples deposited at the lowest $T_s = 70$℃ demonstrates the defect ratio $R_{def} = 22.4$ close to the value $R_{def} = 19.05$ observed in the samples deposited at $T_s = 300$℃.

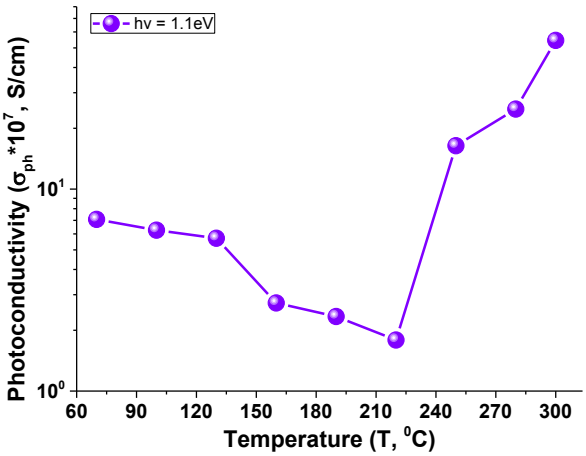

Figure 4.5: Photoconductivity obtained at hv = 1.1eV from the spectral response of photoconductivity

The minimal value of the defect ratio $R_{def} = 6.47$ shows that the density of defects in the optical band gap is lower at 160°C than the density of defects obtained in all the range from $T_s = 300$ to 70°C. This correlates with the behavior of the parameter E_{Upc}. Thus both the defects related to band tail transitions and the deep defect inside the gap show minimal values in the samples deposited at $T_s = 160$°C.

Table 4.1: Parameters of E_{Upc}, R_{def} and σ_{pc} obtained from the spectral characteristics of a-$Ge_{0.97}Si_{0.03}$:H thin films.

Reference	T_s[°C]	$E_{Upc}[meV]$	$R_{def}[a.u.]$	$\sigma_{ph} * 10^7$ $hv = 1.1eV$	$\sigma_{ph} * 10^6$ $hv = 1.8eV$
857	70	51.9	22.4	7.08	4.18
858	100	57	35.7	6.26	3.45
859	130	65	37.7	5.71	4.27
860	160	47	6.47	2.73	1.99
861	190	63	31	2.34	2.45
862	220	93.4	29.7	1.79	2.02
863	250	74	42.5	16.4	18.1
864	280	69	29.8	24.9	29.2
865	300	53.2	19.05	54.5	35.1

Figure 4.5 shows the tendency of photoconductivity measured at $hv \approx E_g$ in the samples deposited at different substrate temperatures. As substrate temperature changes from $T_s = 300$ to 220°C the photoconductivity reduces from $\sigma_{ph} = 5.45x10^{-6}$ to $1.79x10^{-7}$ reaching minimum at $T_s = 220$°C and then increases to

$\sigma_{ph} = 7.08x10^{-7}$ in the samples deposited at $T_s = 70$℃. In Table 4.1 are shown the electronic parameters obtained for the samples of a-$Ge_{0.97}Si_{0.03}$:H films deposited at different substrate temperatures by LF PECVD.

Summary

In this section, the structural and photoelectric characteristics of germanium thin films were studied using the spectral response of short-circuit current as diagnostic tool. The objective of this study was obtain $Ge_{0.97}Si_{0.03}$:H thin films with good structural properties to develop photovotaic devices on flexible subtrates. The results indicate that the $Ge_{0.97}Si_{0.03}$:H thin films do not suffer continuous structural changes when the deposition temperature decreases from $T_d = 300$ to 70℃. The structural disorder of the $Ge_{0.97}Si_{0.03}$:H thin films is similar at $T_d = 300$, 160, and 70℃. The film with the best structural quality was obtained at a deposition temperature of $T_d = 160$℃. This deposition temperature is compatible with most commercial flexible substrates. This film was selected to develop photovoltaic devices. The photoconductivity of the $Ge_{0.97}Si_{0.03}$:H thin film deposited at $T_d = 160$℃ is less than the photoconductivity of the films deposited at $T_d = 300$ and 70℃. The photoconductivity of the $Ge_{0.97}Si_{0.03}$:H thin films is due to transport of majority charge carriers (electrons). In a solar cell, the performance is determined by the transport of the slower charge carrier (holes). Therefore, the magnitude of the photoconductivity is not a limitation for the $Ge_{0.97}Si_{0.03}$:H thin film deposited at $T_d = 160$℃.

4.3 Development of Photovoltaic Devices Fabricated at INAOE

This section shows the development of the photovoltaic devices fabricated at INAOE. The $Ge_{0.97}Si_{0.03}$:H photovoltaic devices were deposited by LF-PECVD at $T_d = 160$℃ using the $Ge_{0.97}Si_{0.03}$:H thin film selected in section 4.2. Section 4.3.1 shows the performance characteristics obtained from the current-voltage characteristics under illumination, section 4.3.2 shows the diagnostic characteristics obtained from the

spectral response of the short-circuit current, section 4.3.3 shows the temperature dependence of diagnostic characteristics obtained from the spectral response of short-circuit current, section 4.3.4 shows the diagnostic characteristics obtained from the dark current-voltage characteristics, and section 4.4.5 shows the diagnostic characteristics obtained from the sub-gap photoconductivity in function of the changes performed to the structural configuration of the photovoltaic devices.

4.3.1 Performance Characteristics obtained from the Current-Voltage Characteristics of the Thin Film Photovoltaic Devices

Figure 4.8 depicts the current-voltage characteristics measured under illumination conditions in the photovoltaic devices deposited at the installations of INAOE. In order to illuminate the samples during the measurements was used the spectrum of light provided by a halogen lamp. During the measurements of current-voltage characteristics under illumination, the light beam had an intensity of $I_0 = 59.96 mW/cm^2$ which was measured with a thermopile sensor (Model 71938). In order to analyze the current-voltage characteristics under illumination were used the open circuit voltage (V_{oc}), the short circuit current (I_{sc}), the fill factor (FF), and the energy-conversion efficiency (η). Figure 4.7b shows the structural configuration of photovoltaic devices fabricated in the process 1075. As it was mentioned above, the main difference between the configuration of a conventional p-i-n structure and the configuration of the photovoltaic devices deposited at the installations of INAOE (see process 1075 in Figure 4.7b) are the intrinsic thin films of a-Si:H deposited between the interfaces p-i and i-n. The initial aim of these films was prevent the diffusion of boron and phosphorus dopants in the intrinsic film of $Ge_{0.97}Si_{0.03}$:H. In Table 3.3 of Chapter 3 we can observe that in the process 1075, the thickness of the intrinsic thin film of a-Si:H is relatively small compared to the thickness of the thin film of $Ge_{0.97}Si_{0.03}$:H (500Å and 9200Å respectively). Therefore, we could expect that the photovoltaic effect in the process 1075 was mainly caused by the photogenerated carriers in the thin film of a-$Ge_{0.97}Si_{0.03}$:H.

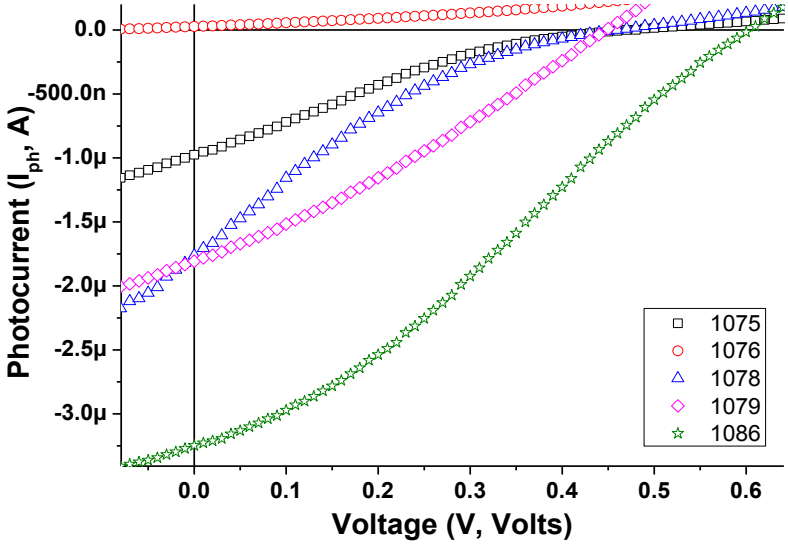

Figure 4.6: I-V characteristics measured in a-Si:H/a-$Ge_{0.97}Si_{0.03}$:H photovoltaic devices in function of device configuration

The results depicted in Figure 4.7a show that the thin films of a-Si:H not only prevent the diffusion of boron and phosphorus dopants but also affects significantly the performance of photovoltaic devices. The analysis of the energy band diagram depicted in Figure 4.7b shows that the thin film of a-Si:H deposited between the n-i interface generates a potential barrier which prevents that the electrons photogenerated in the intrinsic film of $Ge_{0.97}Si_{0.03}$:H may flow towards the n-type film of $Ge_{0.97}Si_{0.03}$:H. In the same way, the intrinsic film of a-Si:H deposited between the p-i interface generates a potential barrier which prevents that the holes photo-generated in the intrinsic film of $Ge_{0.97}Si_{0.03}$:H may flow towards the p-type film of $Ge_{0.97}Si_{0.03}$:H. These potential barriers suppress the photocurrent generated in the intrinsic film of $Ge_{0.97}Si_{0.03}$:H as is shown in the four quadrant of the current-voltage characteristics of Figure 4.7a.

Considering that in terms of the electronic characteristics, the performance of a photovoltaic device is determined by the electronic properties of the slower charge carriers (electrons or holes). In the process 1076 the thickness of the intrinsic film of a-Si:H deposited between the p-i interface was reduced from 500 to 350Å in order to reduce the potential barrier which prevents that the holes may flow from the intrinsic

film of $Ge_{0.97}Si_{0.03}$:H toward the p-type film of $Ge_{0.97}Si_{0.03}$:H. In the same way, by reducing the thickness of the intrinsic film of a-Si:H is possible to increase the flux of photons that can reach the intrinsic film of $Ge_{0.97}Si_{0.03}$:H and increase the concentration of photogenerated carriers that contribute to the photogenerated current of the photovoltaic device.

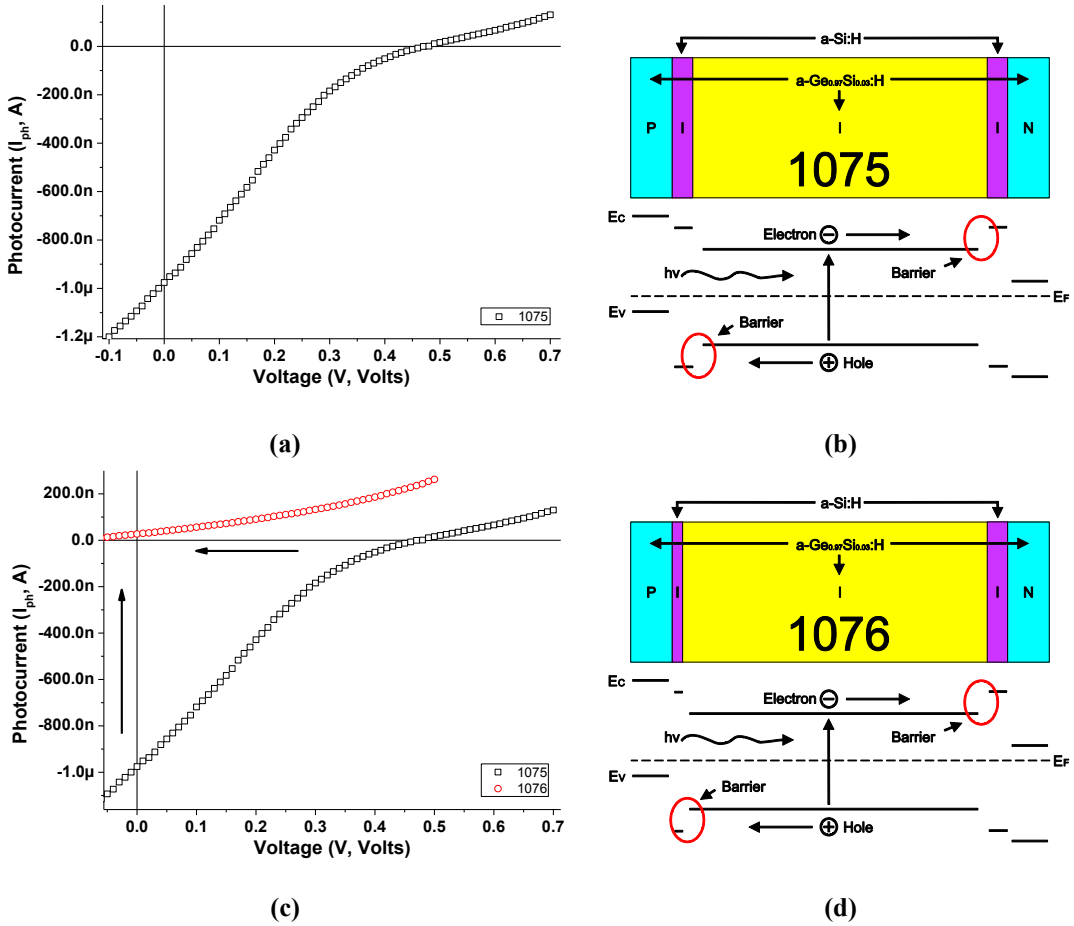

Figure 4.7: (a,c) Current-voltage characteristics and (b,d) structural configurations of the photovoltaic devices deposited in the processes 1075 and 1076 respectively

The results obtained in the process 1076 (see Figure 4.7c) showed that by reducing the thickness of the intrinsic film of a-Si:H, the magnitude of the short circuit current reduces from $I_{sc} = 0.98$ to $0.03\mu A$ (see Figure 4.8) and the magnitude of the open circuit voltage (see Figure 4.9) reduces from $V_{oc} = 0.48$ to $0.1V$. On the other hand,

the value of the fill factor shown in the Figure 4.10 increased from $FF = 0.189$ to 0.244 but the value of the energy-conversion device efficiency decreased from $\eta = 1.48$ to $0.01\ a.u.$ as is shown in Figure 4.11. These results demonstrated that the intrinsic film of a-Si:H deposited between the p-i interface of the device (see Figure 4.7d) contributes significantly to the performance of the photovoltaic device.

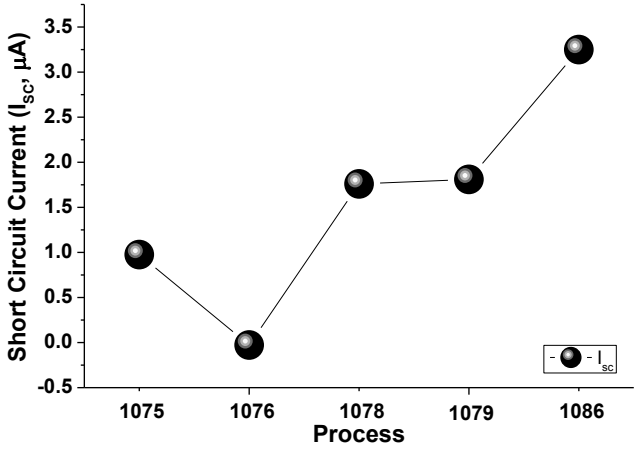

Figure 4.8: Short circuit current extracted from the I-V characteristics under illumination in a-Si:H/a-$Ge_{0.97}Si_{0.03}$:H photovoltaic devices

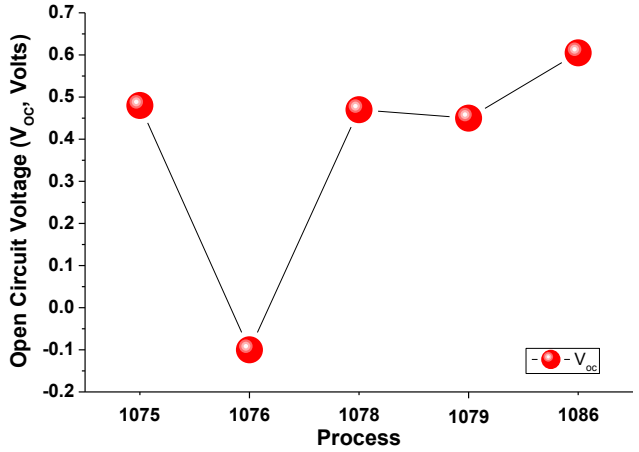

Figure 4.9: Open circuit voltage extracted from the I-V characteristics under illumination in a-Si:H/a-$Ge_{0.97}Si_{0.03}$:H photovoltaic devices

In the same way, in Figure 4.7c is also possible to observe that the polarization of the short-circuit current and open-circuit voltage changed from negative to positive and positive to negative respectively when the thickness of the intrinsic film of a-Si:H was

reduced from 500 to 350Å. This behavior demonstrated us that the potential barrier generated by the intrinsic film of a-Si:H located between the n-i interface of the device (see Figure 4.7d) dominates the photogenerated current flow when it was reduced the thickness of the intrinsic film of a-Si:H located between the p-i interface.

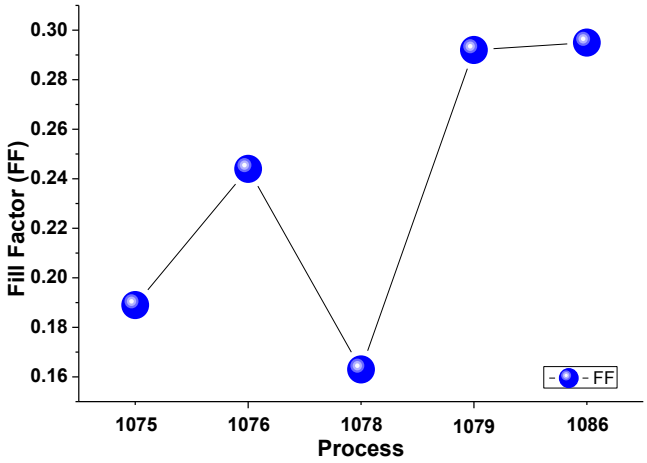

Figure 4.10: Fill factor extracted from the I-V characteristics under illumination in a-Si:H/a-$Ge_{0.97}Si_{0.03}$:H photovoltaic devices

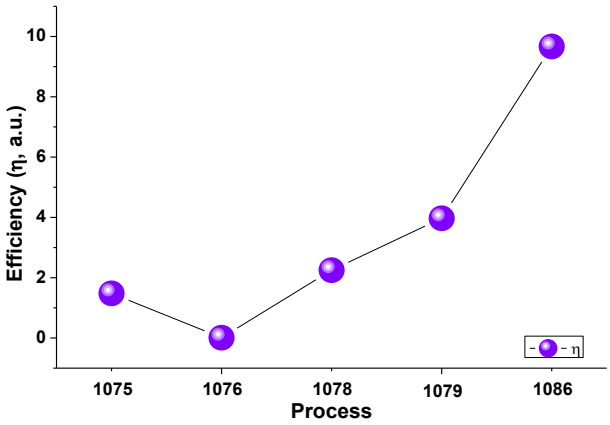

Figure 4.11: Efficiency extracted from the I-V characteristics under illumination in a-Si:H/a-$Ge_{0.97}Si_{0.03}$:H photovoltaic devices

Using the knowledge obtained in the processes 1075 and 1076, in the process 1078 was increased the thickness of the intrinsic film of a-Si:H deposited between the p-i interface of the device from 500 to 630Å with the aim of increasing the contribution

that this film gives to the photovoltaic device. In Figure 4.12c is shown the current-voltage characteristics measured in the photovoltaic device obtained in process 1078. In Figure 4.12d is shown the structural configuration of the same device.

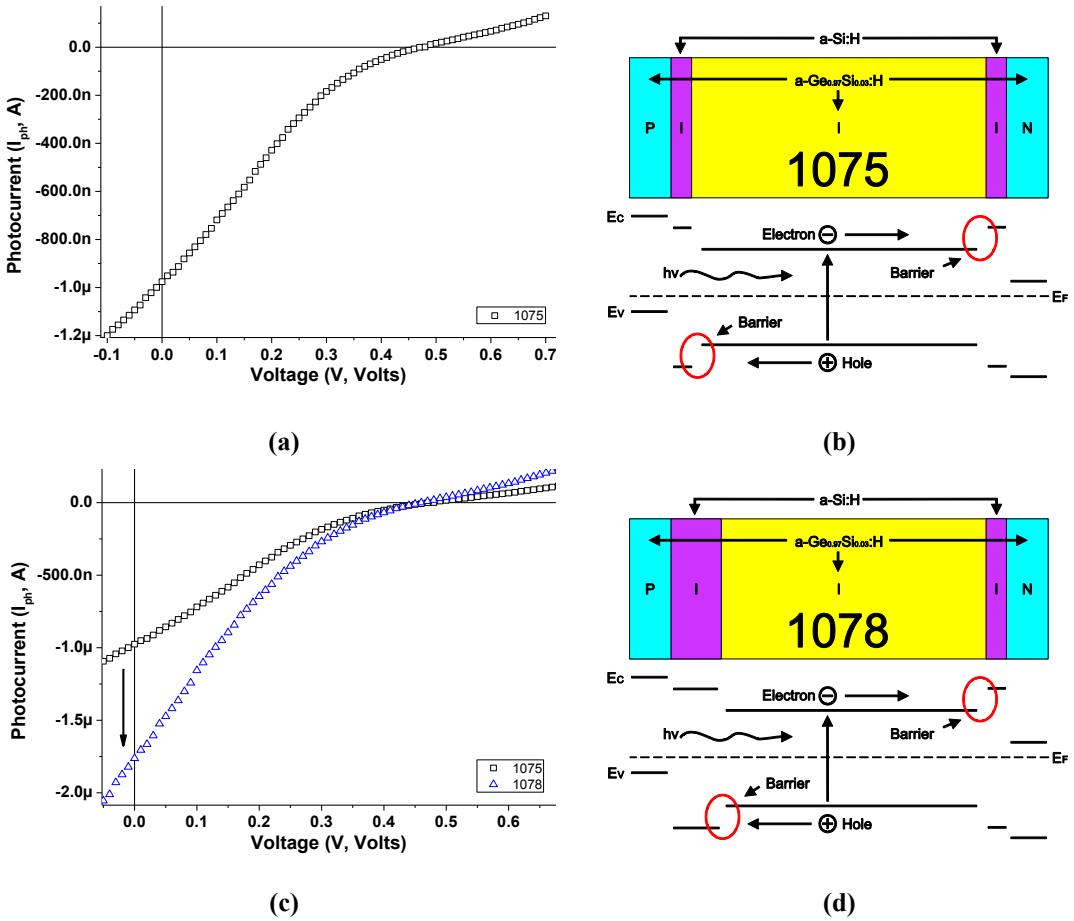

Figure 4.12: (a,c) Current-voltage characteristics and (b,d) structural configurations of the photovoltaic devices deposited in the processes 1075 and 1078 respectively

The results obtained in the process 1078 (see Figure 4.12c) demonstrated us that increasing the thickness of the intrinsic film of a-Si:H, the magnitude of the short-circuit current increased from $I_{sc} = 0.976$ to $1.76\mu A$ and the magnitude of the open-circuit voltage slightly reduced from $V_{oc} = 0.48$ to $0.47V$ taking as reference the process 1075. In process 1078 the energy-conversion efficiency of the photovoltaic device increased from $\eta = 1.48$ to $2.25\ a.u.$. Unfortunately, in the fourth quadrant of

Figure 4.12c we can observe that the current-voltage characteristics measured in the photovoltaic device of the process 1078 still show current suppression. This current suppression caused that the value of the fill factor reduced from $FF = 0.189$ to 0.163.

In the structural diagram depicted in Figure 4.12d we can observe that the potential barriers generated by the intrinsic film of a-Si:H do not suffer any changes when the thickness of the intrinsic film of a-Si:H located between the p-i interface of the device is increased from 500 to 630Å. Therefore, the potential barriers located between the p-i and n-i interfaces continue preventing that the holes and electrons photogenerated in the intrinsic film of $Ge_{0.97}Si_{0.03}$:H can flow toward the p-type and n-type film of $Ge_{0.97}Si_{0.03}$:H respectively. The current suppression depicted in Figure 4.12c remains attached to these potential barriers. However, by increasing the thickness of the intrinsic film of a-Si:H located between the p-i interfaces we reduce the concentration of photons that can reach the intrinsic film of $Ge_{0.97}Si_{0.03}$:H because large part of the concentration of photons is absorbed in the intrinsic film of a-Si:H. Fortunately, photons absorbed in the film of a-Si:H generate electron-hole pairs which contribute to increase the photogenerated current as is shown in Figure 4.12c. The structural configuration depicted in Figure 4.12d shows that the holes photogenerated in the intrinsic film of a-Si:H have no potential barriers which prevent that the holes can flow from the intrinsic film of a-Si:H toward the p-type film of $Ge_{0.97}Si_{0.03}$:H.

Again using the knowledge obtained in the process 1078, in the process 1079 it was increased the thickness of the intrinsic film of a-Si:H located between the p-i interface of the device from 630 to 715Å and it was reduced the thickness of the intrinsic film of a-Si:H located between the n-i interface of the device from 500 to 107Å. The results obtained are shown in Figure 4.13c. In Figure 4.13d is shown the structural configuration of the photovoltaic device. In Figure 4.13c and Figure 4.13d we can observe that by reducing the thickness of the intrinsic film of a-Si:H located between the n-i interface of the device, the current-voltage characteristics does not show current suppression. The value of the fill factor increased from $FF = 0.163$ to 0.292 and the

energy-conversion efficiency increased from $\eta = 2.25$ to $3.97\ a.u.$. These results demonstrated that the potential barrier located between the n-i interface of the device prevents that the electrons photogenerated in the intrinsic films of a-Si:H and $Ge_{0.97}Si_{0.03}$:H can jump the potential barrier or can tunneling through it.

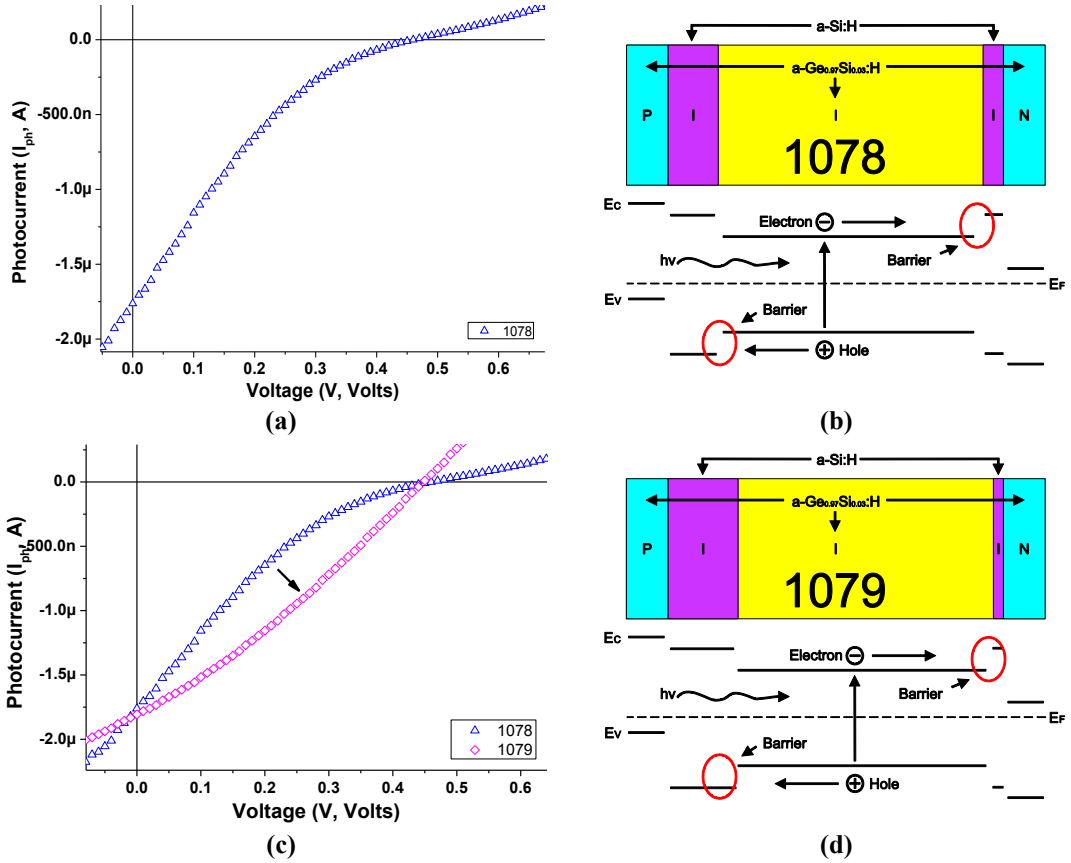

Figure 4.13: (a,c) Current-voltage characteristics and (b,d) structural configurations of the photovoltaic devices deposited in the processes 1078 and 1079 respectively

On the other hand, when we increased the thickness of the intrinsic film of a-Si:H located between the p-i interface of the device the short-circuit current increases slightly from $I_{sc} = 1.76$ to $1.81\mu A$ and the open-circuit voltage decreases from $V_{oc} = 0.47$ to $0.45V$. These results demonstrated that when we increase the thickness of the film of a-Si:H, the absorption of the flux of photons increase but the short-circuit current does not increase significantly as it was observed in the process 1078 (I_{sc} increased from 0.976 to $1.76\mu A$). This behavior indicates that the potential barrier

located between the n-i interface is more important than the potential barrier located between the p-i interface of the device and the photon absorption in the intrinsic film of a-Si:H located between the p-i interface of the device.

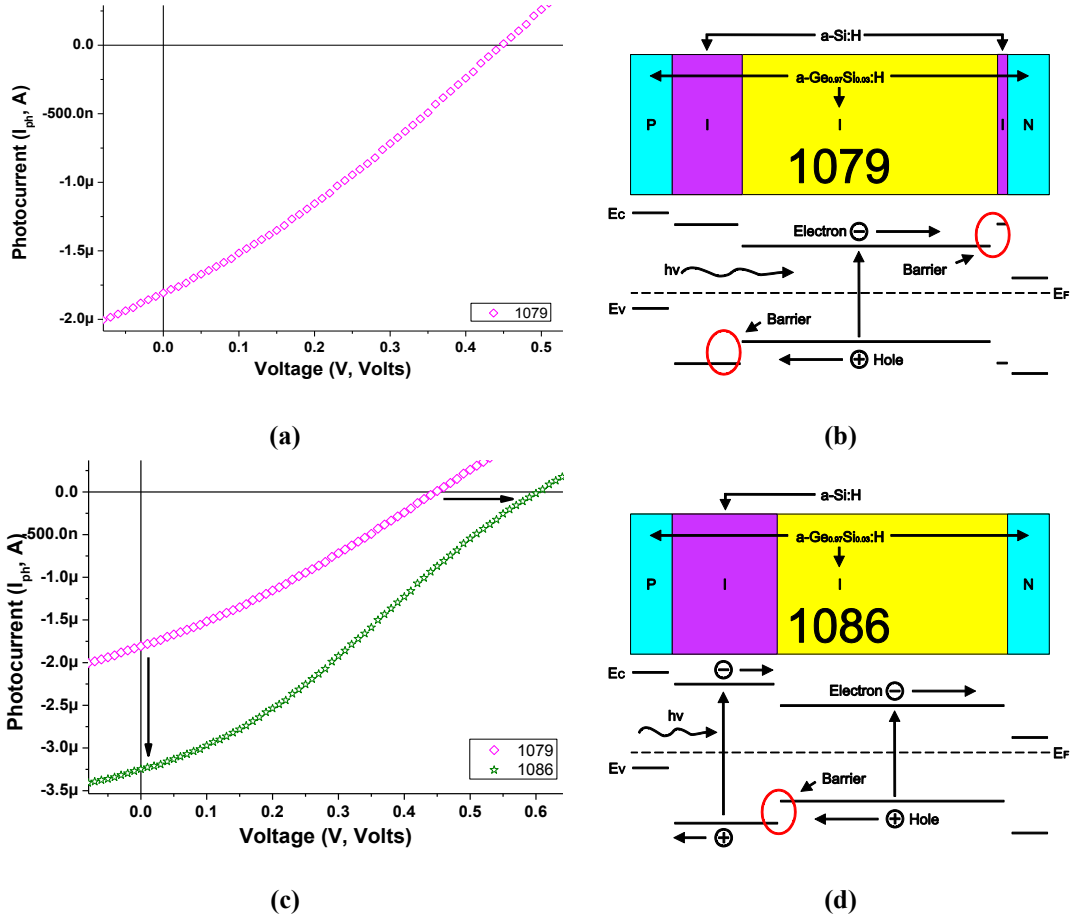

Figure 4.14: (a,c) Current-voltage characteristics and (b,d) structural configurations of the photovoltaic devices deposited in the processes 1079 and 1086 respectively

Finally in the process 1086, the intrinsic film of a-Si:H which was located between the n-i interface of the device was eliminated and the thickness of the intrinsic film of a-Si:H located between the p-i interface of the device was increased from 715 to 1071Å as is shown in Figure 4.14d. In this process the current-voltage characteristics showed that the short-circuit current increased from $I_{sc} = 1.81$ to $3.25\mu A$ and the open-circuit voltage also increased from $V_{oc} = 0.45$ to $0.61V$. The value of the fill factor increased from $FF = 0.292$ to 0.295 and the energy-conversion efficiency

increased from $\eta = 3.97$ to $9.67 a.u.$. The analysis of the energy band diagram depicted in Figure 4.14c shows that when it is removed the intrinsic film of a-Si:H which was placed between the n-i interface of the device, the electrons photogenerated in the intrinsic films of a-Si:H and a-$Ge_{0.97}Si_{0.03}$:H do not have any potential barrier that prevents them being dragged towards the n-type film of $Ge_{0.97}Si_{0.03}$:H.

The potential barrier located between the p-i interface of the device remains preventing that the holes photogenerated into the intrinsic film of $Ge_{0.97}Si_{0.03}$:H are dragged into the p-type film of $Ge_{0.97}Si_{0.03}$:H. But the holes photogenerated into the intrinsic film of a-Si:H do not have any potential barrier that prevents them being dragged towards the p-type film of $Ge_{0.97}Si_{0.03}$:H. Therefore, we can expect that the current photogenerated in the device is composed mostly by electrons photogenerated in the intrinsic films of a-Si:H and $Ge_{0.97}Si_{0.03}$:H and by holes photogenerated in the intrinsic film of a-Si:H.

4.3.1.1 **Maintenance performed in manufacturing laboratory**

Figure 4.15 shows the current-voltage characteristics measured in the processes 1086 and 1115. The process 1086 was manufactured before the annual maintenance of the manufacturing laboratory and the process 1115 was manufactured after annual maintenance. The deposition conditions and the thickness of the films that make up the devices were equal in both photovoltaic devices. Table 4.2 shows the thickness of the films that make up the photovoltaic devices.

Table 4.2: Thicknesses (Å) of the films that constitute the photovoltaic devices

Process	Susbtrate	Contact	p-type GeSi:H	intrinsic a-Si:H	intrinsic GeSi:H	n-type GeSi:H	Contact
1086			160	1071	9200	240	
1115				1070			

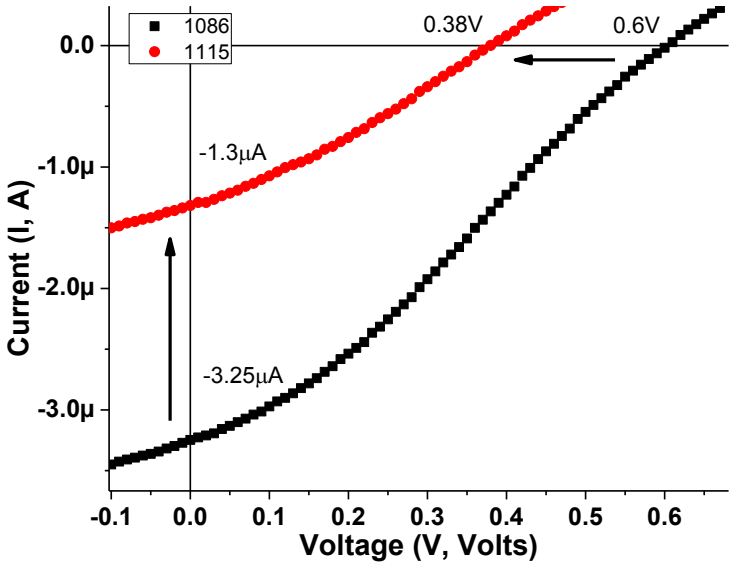

Figure 4.15: Current-Voltage characteristics measured in the processes deposited before (1086) and after (1115) maintenance performed in manufacturing laboratory

In Figure 4.15 we can see that the performance of photovoltaic devices reduced after perform the maintenance to the manufacturing laboratory. The open-circuit voltage reduced from $0.6V$ to $0.38V$ and the short-circuit current decreased from $3.25\mu A$ to $1.3uA$. The photogenerated current reduced across all the active region of the photovoltaic device.

4.3.1.2 Contribution of the intrinsic films of a-Si:H and $Ge_{0.97}Si_{0.03}$:H to the performance of the photovoltaic devices

As it was observed in the processes 1075, 1078, 1079, and 1086, the potential barrier located between the n-i interface of the device reduces the performance of the photovoltaic devices but the increase of the thickness of the intrinsic film of a-Si:H located between the p-i interface helps to improve the performance of the photovoltaic devices. Unfortunately, the results obtained so far do not show whether the film of a-Si:H is more important than the film of $Ge_{0.97}Si_{0.03}$:H in the improving of the performance of the photovoltaic devices. To answer this question in the processes 1109 and 1114 was varied the thickness of the intrinsic films of a-Si:H and $Ge_{0.97}Si_{0.03}$:H

taking as reference the process 1115. In Figure 4.16 is shown the current-voltage characteristics and the structural configurations of the photovoltaic devices obtained in the processes 1109, 1114 and 1115.

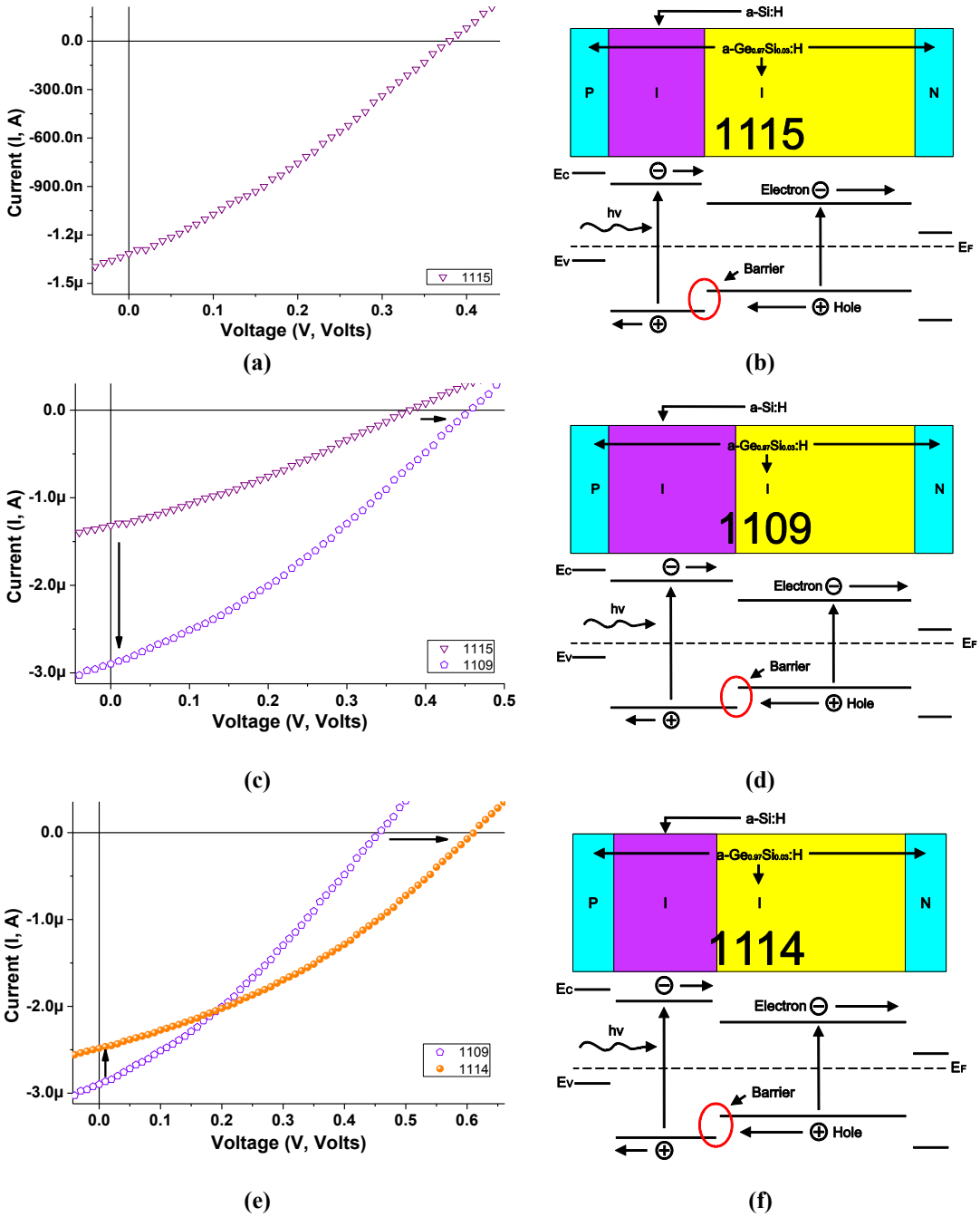

Figure 4.16: (a,c) Current-voltage characteristics and (b,d) structural configurations of the photovoltaic devices deposited in the processes 1079 and 1086 respectively

In Figure 4.16 and Figure 4.17 we can see that increasing the thickness of the intrinsic film of a-Si:H from 1070 to 1300Å and by reducing the thickness of the intrinsic film of $Ge_{0.97}Si_{0.03}$:H from 9200 to 7300Å, the value of the short-circuit current increased from $I_{sc} = 1.32$ to $2.89\mu A$ and the open circuit voltage increased from $V_{oc} = 0.38$ to $0.46V$. The value of the fill factor increased from $FF = 0.302$ to 0.314 and the energy-conversion efficiency also increases from $\eta = 2.52$ to $6.97 a.u.$.

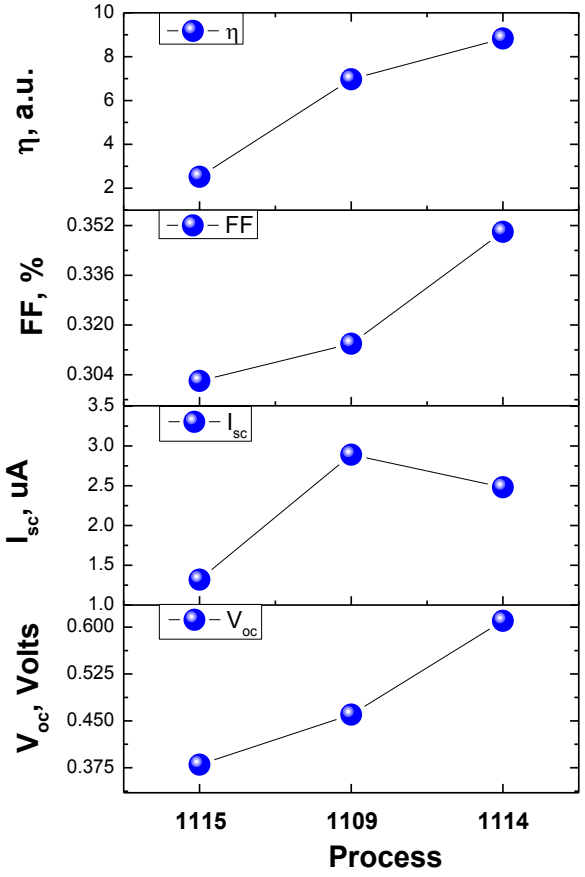

Figure 4.17: Parameters extracted from the I-V characteristics under illumination in the a-Si:H/a-$Ge_{0.97}Si_{0.03}$:H photovoltaic devices

As it was mentioned above, the electrons and holes photogenerated in the intrinsic film of a-Si:H do not have any potential barrier that avoid them being dragged into the n-type and p-type films of $Ge_{0.97}Si_{0.03}$:H, respectively. Therefore, by increasing the

thickness of the intrinsic film of a-Si:H increases the absorption of the flux of photons, increases the photogeneration of charge carriers in the intrinsic film, and increases the photogenerated current of the device. Now, we can observe in the process 1115 that the total thickness of the intrinsic region of the device is formed by the thickness of the intrinsic film of a-Si:H and the thickness of the intrinsic film of $Ge_{0.97}Si_{0.03}$:H. This gives us a total thickness of $10270Å$ for the process 1115 and a total thickness of $8600Å$ for the process 1109. Which indicates that by reducing the thickness of the intrinsic region of the device, we reduce the probability of recombination in the intrinsic region and as a result increases the open circuit voltage. An increase in the value of the short-circuit current and in the value of the open-circuit voltage, increases the value of the fill factor and consequently increases the energy-conversion efficiency.

To corroborate the above assumptions, in the process 1114 was reduced the thickness of the intrinsic film of a-Si:H from 1300 to $1070Å$ and was reduced the thickness of the intrinsic film of $Ge_{0.97}Si_{0.03}$:H from 7300 to $6100Å$. The current-voltage characteristics showed that by reducing the thickness of the intrinsic film of a-Si:H, the value of the short-circuit current was reduced from $I_{sc} = 2.89$ to $2.48\mu A$. And reducing the thickness of the intrinsic region of the device from 8600 for the process 1109 to $7170Å$ for the process 1114, the value of the open-circuit voltage increased from $V_{oc} = 0.46$ to $0.61V$. In this process the value of the fill factor increased from $FF = 0.314$ to 0.35 and the energy-conversion efficiency also increased from $\eta = 6.97$ to $8.83\ a.u.$. This behavior shows that the increase of the open-circuit voltage is more important than the decrease of the short circuit current to enhance the performance of the photovoltaic devices. Unfortunately, the potential barrier located at the p-i interface of the device continues avoiding that the holes photogenerated in the intrinsic film of $Ge_{0.97}Si_{0.03}$:H may contribute significantly to the performance of the photovoltaic devices.

Summary

In this section was performed a study about the performance characteristics of the photovoltaic devices deposited at the installations of the INAOE in function of the structural configuration. The principal difference between the configuration of the photovoltaic devices of a-Si:H/$Ge_{0.97}Si_{0.03}$:H and the configuration of a conventional p-i-n device are the a-Si:H thin films deposited between the p-i and i-n interfaces as is shown in Figure 3.3a. The main function of the a-Si:H films is avoid the diffusion of Boron and Phosphorous from the p- and n-type films into the instrinsic film of $Ge_{0.97}Si_{0.03}$:H.

The results indicate that the intrinsic film of a-Si:H deposited between the p-i interface of the device enhances the performance of the photovoltaic devices and the intrinsic film of a-Si:H deposited between the i-n interface of the devices reduces the performance of the photovoltaic devices. The device obtained in the process 1086 showed the best performance characteristics. The performance characteristics obtained in the process 1086 can not compete with the performance of the commercial devices. However at INAOE was developed for the first time a functional thin film photovoltaico device.

The study on the performance characteristics showed that the maintenance performed on manufacturing laboratory reduced the performance of the device. The performance characteristics also showed that the intrinsic films of a-Si:H and $Ge_{0.97}Si_{0.03}$:H contribute to the performance of the photovoltaic devices.

Performance characteristics studied in this work show that the structural configuration of the devices significantly affect the performance of the devices. But a deeper study is needed to understand specifically as the performance of the photovoltaic devices was affected and the performance characteristics do not give us this type of information.

4.3.2 Diagnostic of the Thin Film Photovoltaic Devices by means of the Spectral Response of Short-Circuit Current

The results obtained in section 4.3.1 demonstrated us that the intrinsic film of a-Si:H (see Figure 3.3a) deposited between the p-i and n-i interfaces of the photovoltaic devices of a-Si:H/$Ge_{0.97}Si_{0.03}$:H affect significantly the current-voltage characteristics measured under illumination conditions. In Figure 4.18 we can see that the spectral response of photovoltaic devices is also affected significantly when we change the thickness of the intrinsic film of a-Si:H.

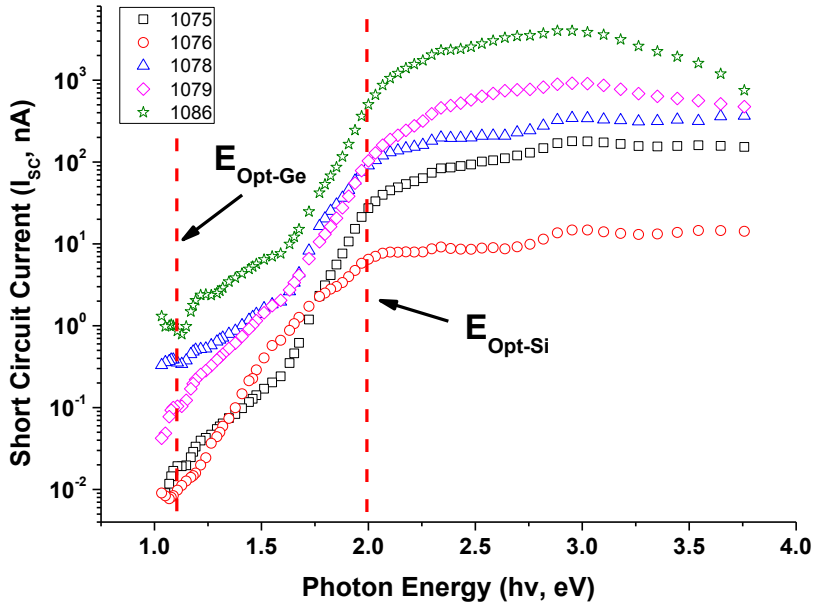

Figure 4.18: Comparison of spectral characteristics measured in a-Si:H/a-$Ge_{0.97}Si_{0.03}$:H photovoltaic devices fabricated at INAOE installations

The spectral response of photovoltaic devices was normalized to a constant intensity of $I_0 = 1.2mW/cm^2$. In Figure 4.18 we can deduce that the optical bandwidth of the intrinsic film of a-Si:H could have an approximate value of $E_g = 2eV$ and from Figure 4.1 we can deduce that the optical bandwidth of the intrinsic film of a-$Ge_{0.97}Si_{0.03}$:H could have an approximate value $E_g = 1.2eV$. Which indicate us that the flux of photons with an energy greater than $hv > 2eV$ are absorbed into extended states of the

intrinsic film of a-Si:H located at the p-i interface of the device and extended states of the intrinsic film of $Ge_{0.97}Si_{0.03}$:H. The flux of photons with an energy greater than $hv > 1.2eV$ are absorbed into extended states of the intrinsic film of $Ge_{0.97}Si_{0.03}$:H and localized states of intrinsic film of a-Si:H.

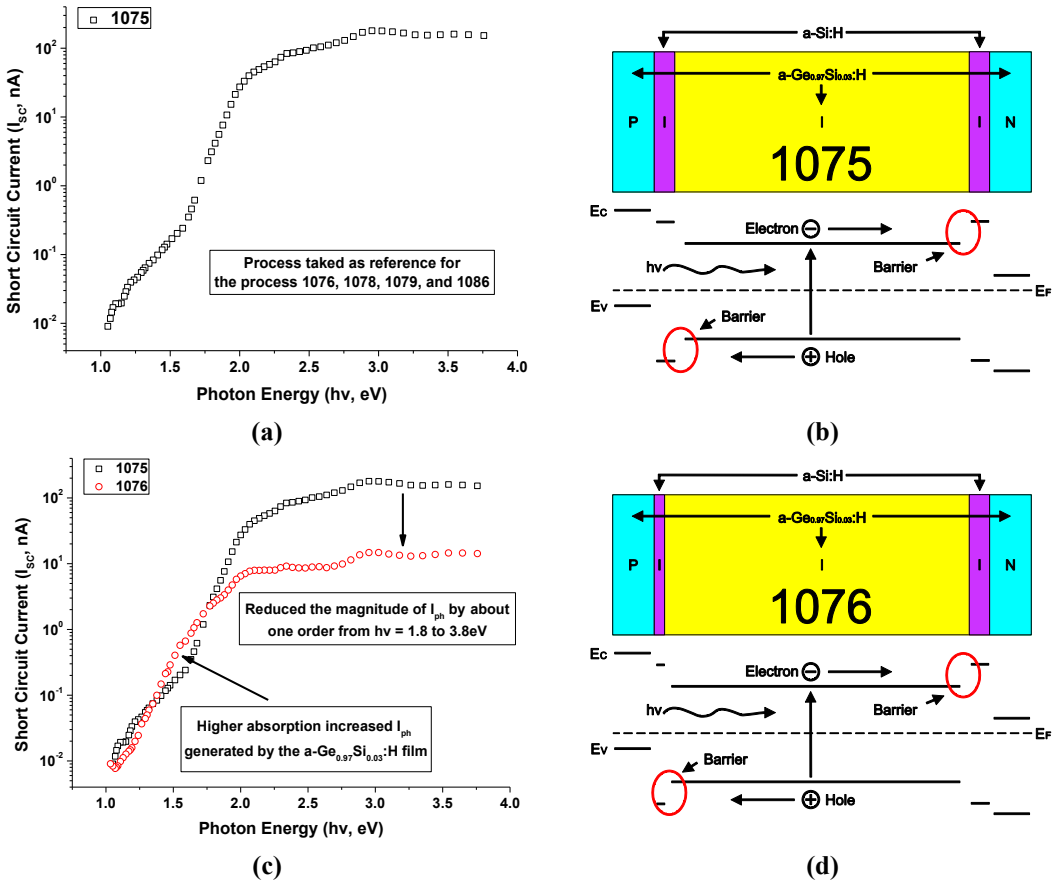

Figure 4.19: (a,c) Spectral characteristics and (b,d) structural configurations of the photovoltaic devices deposited in the process 1075 and 1076 respectively

Figure 4.19 shows the spectral response and the structural configuration of the photovoltaic devices obtained in the processes 1075 and 1076. The results obtained in these processes proved that by reducing the thickness of the intrinsic film of a-Si:H located between the p-i interface of the device from 500 to 350Å, the photocurrent obtained over an energy range from $hv = 1.8$ to $3.8eV$ reduced by approximately one order of magnitude but the magnitude of the photocurrent obtained over an energy

range from $hv = 1$ to $1.8eV$ not changes significantly. Therefore, we conclude that effectively in the process 1076, the short circuit current reduced from $I_{sc} = 0.98$ to $0.03\mu A$ because reducing the thickness of the intrinsic film of a-Si:H located between the p-i device interface we reduced the current photo-generated within the energy range from $hv = 1.8$ to $3.8eV$ as is shown in Figure 4.19 and Figure 4.7.

In Figure 4.19c we also can see that by reducing the thickness of the intrinsic film of a-Si:H, we increase slightly the photocurrent generated within the energy range from $hv = 1$ to $1.8eV$ taking as reference the process 1075. This behavior confirms that by reducing the thickness of the intrinsic film of a-Si:H we increase the flux of photons that can reach the intrinsic film of $Ge_{0.97}Si_{0.03}$:H and we increase the absorption of photons within it. By increasing the absorption of the flux of photons within the intrinsic film of $Ge_{0.97}Si_{0.03}$:H we increase the generation of the electron-hole pairs which contribute to the photocurrent of the device. Unfortunately, reducing the thickness of the intrinsic film of a-Si:H we also reduce the built-in potential inside the device and likewise reduce the magnitude of the photo-generated current in the whole energy range measured.

Figure 4.20 shows the spectral characteristics obtained in the processes 1075 and 1078 taking as reference to the process 1075. In the spectral characteristics shown in Figure 4.20c we can observe that by increasing the thickness of the intrinsic film of a-Si:H located between the p-i interface of the device from 500 to 600, the photocurrent increased over all the energy range measured. This caused that the short circuit current shown in Figure 4.12c increased from $I_{sc} = 0.976$ to $1.76\mu A$. For the energy range between $hv = 1.8$ and $3.8eV$, the photocurrent increased approximately half an order of magnitude evenly but for the energy range between $hv = 1$ and $1.8eV$ the photocurrent do not increase uniformly. In this energy range, the photocurrent increased more than one order of magnitude for an energy of $hv = 1eV$ and reduced as the energy photon increased until to obtain an increase of approximately half order of magnitude for an energy of $hv = 1.8eV$. This behavior shows that increasing the

thickness of the intrinsic film of a-Si:H we increase the absorption of the flux of photon by extended and localized states of the intrinsic film of a-Si:H. Therefore, we can expect that to increasing a little more the thickness of the intrinsic film of a-Si:H we can increase again the photocurrent throughout the energy range measured.

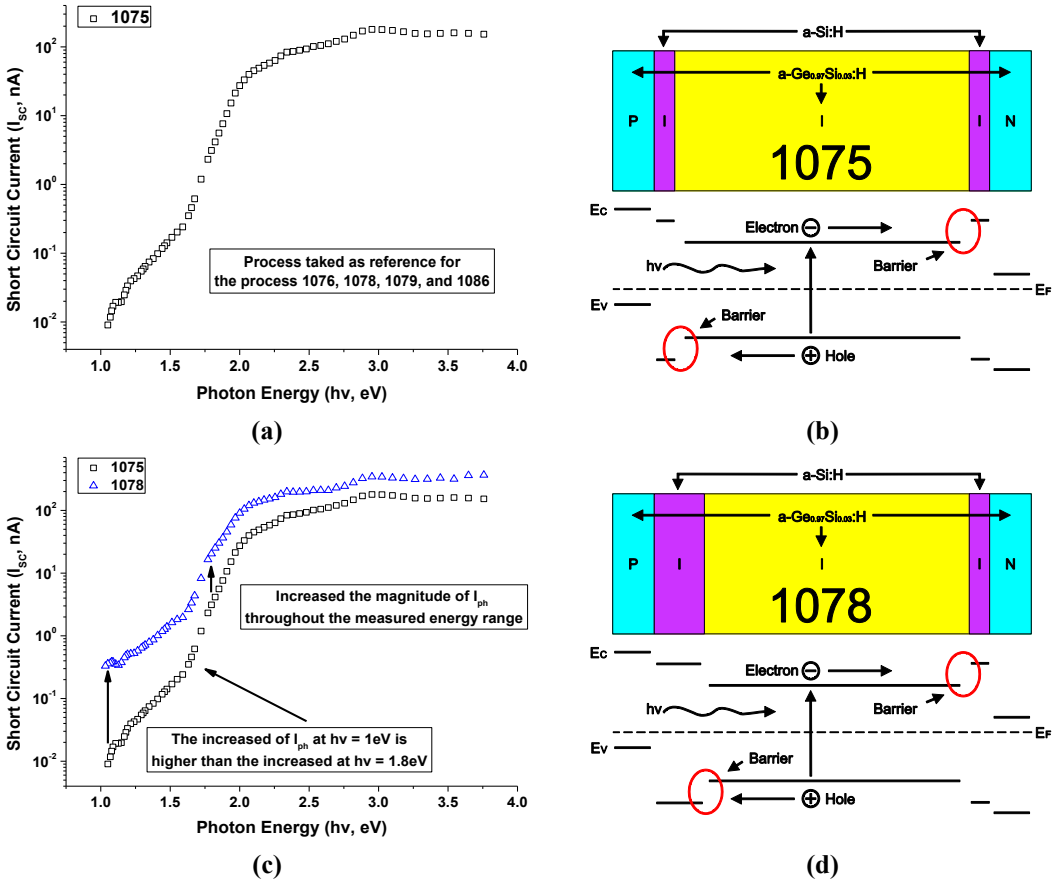

Figure 4.20: (a,c) Spectarl characteristics and (b,d) structural configurations of the photovoltaic devices deposited in the process 1075 and 1078 respectively

In the process 1079 was increased the thickness of the intrinsic film of a-Si:H located between the p-i interface of the device from 630 to 715 and was reduced the thickness of the intrinsic film of a-Si:H located between the i-n interface of the device from 500 to 107 as is shown in Figure 4.21d. The spectral craracteristics obtained in the process 1079 (see Figure 4.21c) demonstrated that increasing the thickness of the intrinsic film of a-Si:H, the current increases between the energy range from $hv = 2$ to

$3.8eV$. The current obtained within the energy range from $hv = 1.6$ to $2eV$ do not change significantly and the current obtained within the energy range from $hv = 1$ to $1.6eV$ reduces in comparison with the current obtained in the process 1078. This behavior explains why the short-circuit current only increased from $I_{sc} = 1.76$ to $1.81eV$ (see Figure 4.13c of Section 4.3.1) when we increase the thickness of the intrinsic film of a-Si:H from 630 to 715.

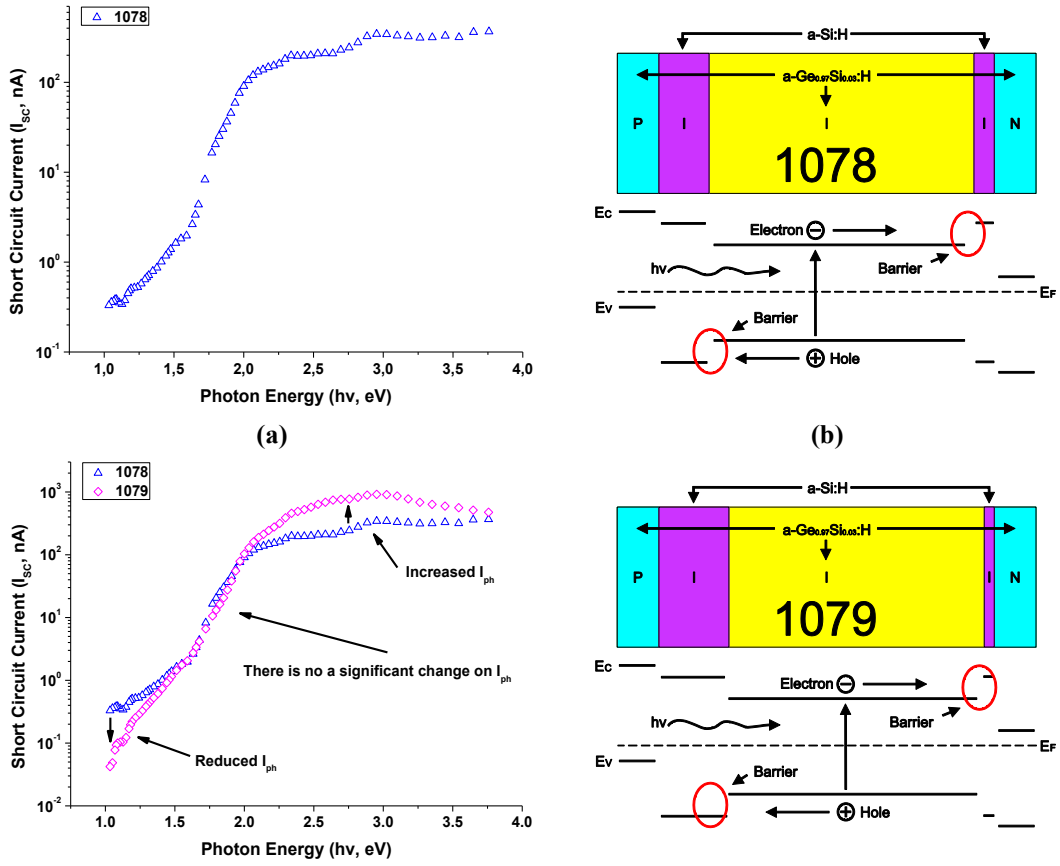

Figure 4.21: (a,c) Current-voltage characteristic and (b,d) structural configuration of the photovoltaic device deposited in the process 1078 and 1079 respectively

However, the current obtained within the energy range from $hv = 1$ to $1.6eV$ (see Figure 4.21c) indicates that in the process 1078, the current within the energy range from $hv = 1$ to $1.8eV$ (see Figure 4.20c) not only increase due to the absorption of the flux of photons by the localized states of the intrinsic film of a-Si:H. The current

increases because a portion of the flux of photons was absorbed by the intrinsic film of $Ge_{0.97}Si_{0.03}$:H. Therefore, when we increased the thickness of the intrinsic film of a-Si:H in the process 1079, the flux of photons that are absorbed by the intrinsic film of $Ge_{0.97}Si_{0.03}$:H was reduced, and in consequence, the photocurrent generated within the energy range from $hv = 1$ to $1.8eV$ was reduced.

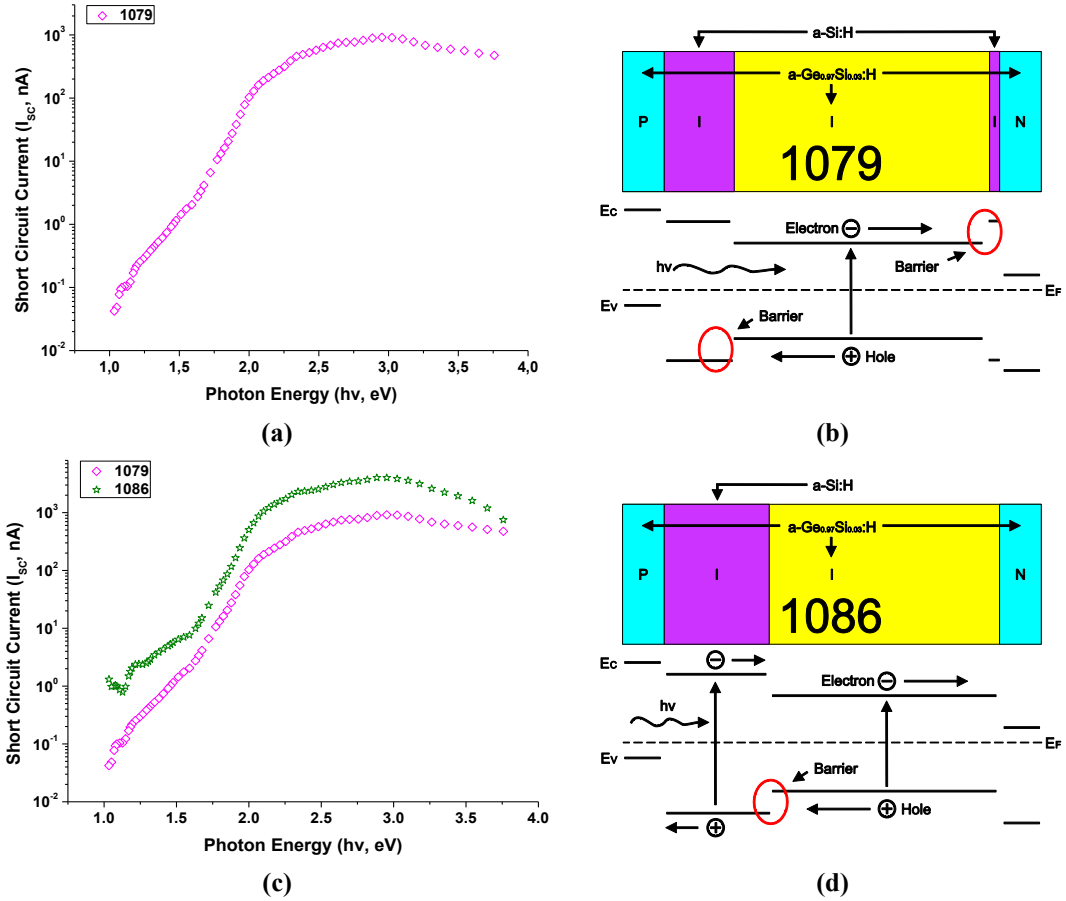

Figure 4.22: (a,c) Current-voltage characteristic and (b,d) structural configuration of the photovoltaic device deposited in the process 1079 and 1086 respectively

Finally in the process 1086 was increased the thickness of the intrinsic film of a-Si:H located between the p-i interface of the device from 715 to 1070 and was removed the intrinsic film of a-Si:H located between the n-i interface of the device. Figure 4.22 shows the spectral characteristics and the structural configurations of the processes 1079 and 1086. The spectral characteristics obtained in the process 1086 (see Figure

4.22c) demonstrated that to eliminate the potential barrier generated by the intrinsic film of a-Si:H located between the n-i interface of the device, the photocurrent increased in all the energy range measured in comparison with the spectral characteristics measured in the process 1079. This behaviour caused that the short-circuit current and the open-circuit voltage shown in Figure 4.14c increased from $I_{sc} = 1.81$ to $3.25 \mu A$ and $V_{oc} = 0.45$ to $0.61 V$, respectively.

If the value of the open-circuit voltage increases when we eliminate the potential barrier located between the n-i interfaces of the device then the built-in potential of the device also increases. Therefore, the electric field that draws the electron-hole pairs photogenerated in the intrinsic films of a-Si:H and $Ge_{0.97}Si_{0.03}$:H towards the n- and p-type films of the device also increases. This behavior could explain why the photocurrent increase over all the energy range measured by means of removing the potential barrier located at n-i interface of the device.

4.3.2.1 Maintenance Performed in Manufacturing Laboratory

Figure 4.23 shows the spectral response of the short-circuit current measured in the processes deposited before (1086) and after (1115) maintenance performed to the manufacturing laboratory.

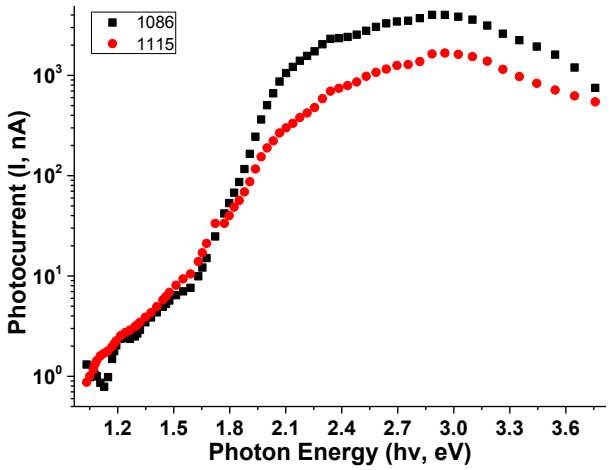

Figure 4.23: Spectral characteristics of short-circuit current measured in the processes deposited before (1086) and after (1115) maintenance performed in manufacturing laboratory

Section 4.3.1.1 shows that the maintenance performed to the manufacturing laboratory reduces the performance of the photovoltaic devices. In Figure 4.23 we can see that after laboratory maintenance, the short-circuit current decreases within the energy range from $hv \geq 1.8$ to $3.8eV$. In this region the contribution of the a-Si:H film has a greater impact, therefore, the reduction of short-circuit current is mainly attributed to the contribution of the intrinsic thin film of a-Si:H.

4.3.2.2 Contribution of the Intrinsic Films of a-Si:H and $Ge_{0.97}Si_{0.03}$:H to the Performance of the Photovoltaic Devices

Figure 4.24 shows the comparison of the spectral response of the short-circuit current obtained in the processes 1115, 1109 and 1114 taking as reference the process 1115. In Figure 4.24c is shown that increasing the thickness of the intrinsic film of a-Si:H, the short-circuit current increases within the energy range from 1.8 to $3.8eV$. This behavior indicates us that when we increase the thickness of the intrinsic film of a-Si:H, the absorption of the flux of photons within the same energy range is increased and hence the short-circuit current is also increased. The short-circuit current does not change significantly within the energy range from $hv \geq 1.0$ to $1.8eV$.

Figure 4.24e shows that when we reduces the thickness of the intrinsic films of a-Si:H and $Ge_{0.97}Si_{0.03}$:H, the short-circuit current generated within the energy range from $hv > 2.2$ to $3.8eV$ reduces and the short-circuit current generated within the energy range from $hv \geq 1$ to $2.2eV$ increases. This behavior indicate us that the short-circuit current generated within the energy range from $hv > 2.2$ to $3.8eV$ reduces because the contribution of the intrinsic film of a-Si:H reduces and the short-circuit current generated within the energy range from $hv \geq 1$ to $2.2eV$ increases because the absorption of the flux of photons in the intrinsic film of $Ge_{0.97}Si_{0.03}$:H increases. These results show that the thickness of the intrinsic film of $Ge_{0.97}Si_{0.03}$:H contributes to the generation of photocurrent but the potential barrier localized between the interface of the intrinsic films of a-Si:H and $Ge_{0.97}Si_{0.03}$:H reduces the contribution.

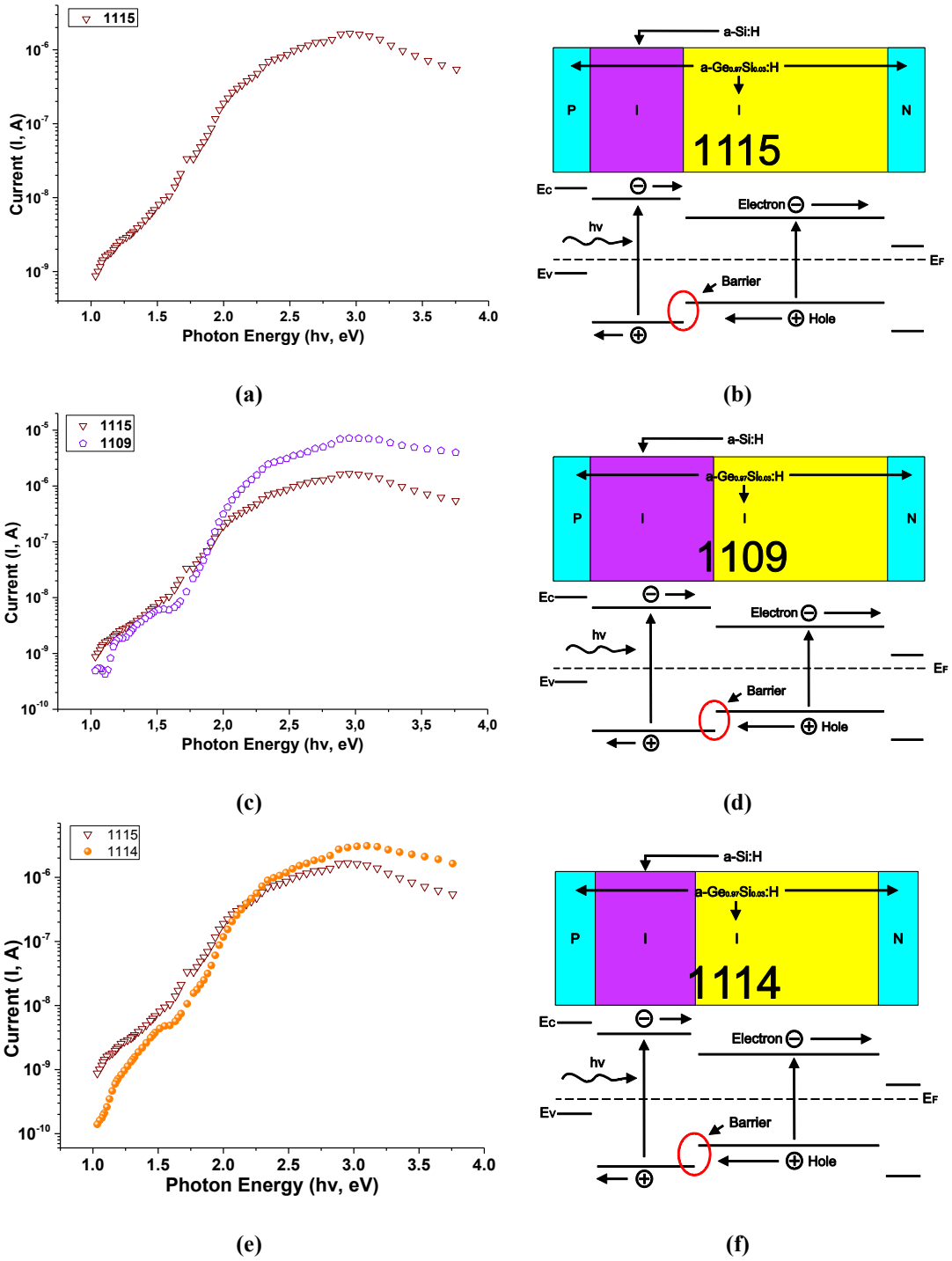

Figure 4.24: (a,c) Current-voltage characteristic and (b,d) structural configuration of the photovoltaic device deposited in the process 1079 and 1086 respectively

Summary

In this section the spectral response of the short-circuit current was used to diagnostic the performance of the photovoltaic devices deposited at the installation of the INAOE. The results obtained in this section confirms that the short circuit-current increases due to the absorption of the photon flux increases in the intrinsic film of a-Si:H.

The results also showed that when we remove the intrinsic film of a-Si:H deposited in the n-i interface, the current increases throughout the measured energy range. This behavior shows that the potential barrier localized in the n-i interface reduces the current photogenerated in all the structure.

The spectral response of the short-circuit current reveals that the intrinsic film of $Ge_{0.97}Si_{0.03}$:H contributes to the performance of the photovoltaic devices throughout the measured energy range.

The spectral response of the short-circuit current also reveals that after perform the laboratory maintenance the short-circuit current decreased due to the contribution the intrinsic film of a-Si:H reduces.

4.3.3 Effect of Temperature on the Spectral Response of the Short-Circuit Current of the Photovoltaic Devices

Figure 4.25 shows the temperature dependence of the spectral response of the short-circuit current measured on the a-Si:H/a-$Ge_{0.97}Si_{0.03}$:H photovoltaic device (Process 1114) as a function of the operating temperature. In this figure we can see that the increase of the operating temperature increases the photocurrent in all the energy range measured. The temperature dependence of the of the short-circuit current obtained at a photon energy of $hv = 1.8$, 3 and $3.8eV$ is shown in Figure 4.26. The short circuit current increases with increasing temperature at a rate of $1.58nA/°K$ for a photon

energy of $hv = 1.8eV$, $50.9nA/°K$ for a photon energy of $hv = 3eV$, and $21.9nA/°K$ for a photon energy of $hv = 3.8eV$ in the following form:

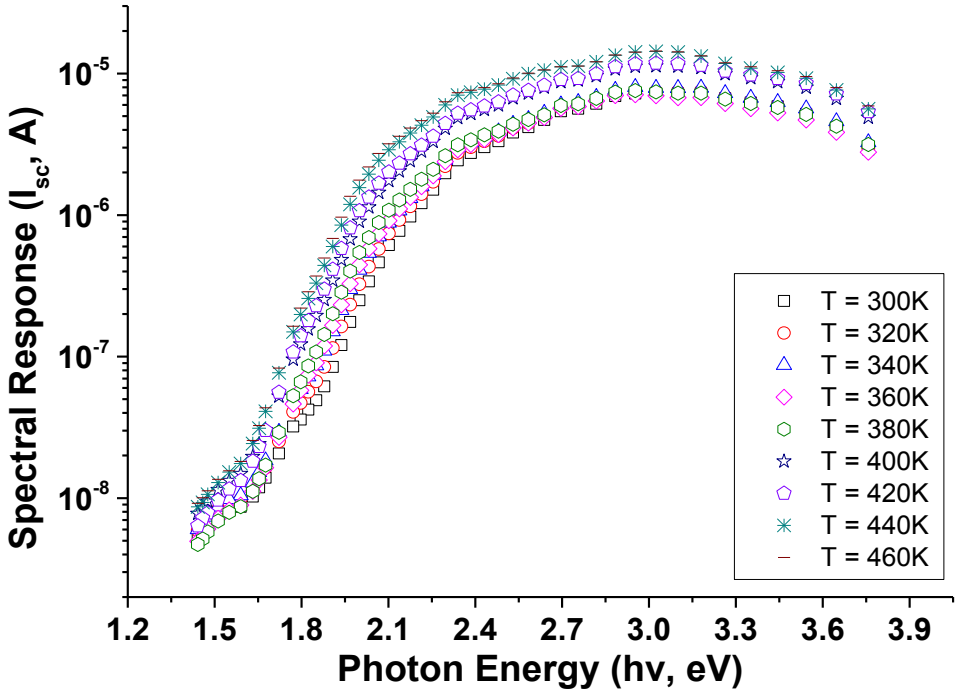

Figure 4.25: Temperature dependence of spectral characteristics of the a-Si:H/a-Ge0.97Si0.03:H plotted on scales a) $I_{sc}(hv)$ vs hv and b) $\ln(I_{sc}(hv))$ vs hv, respectively

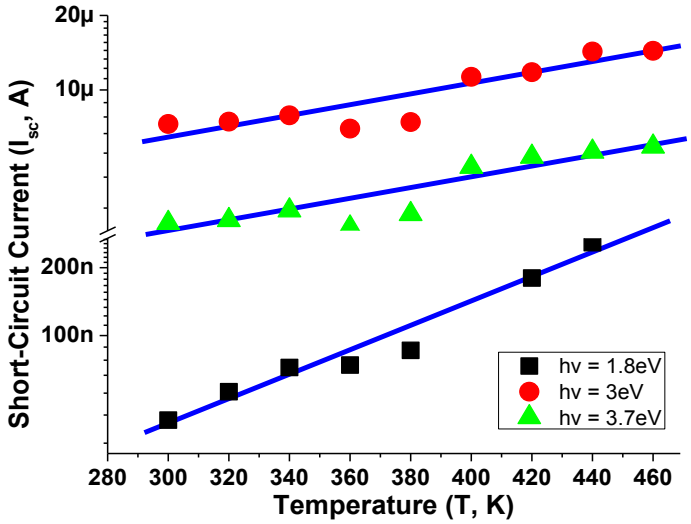

Figure 4.26: Short-Circuit Current measured at a photon energy of $hv = 1.8$, 3 and $3.8eV$ in function of the operating temperature

$$I_{sc} = I_s \exp\left(-\frac{E_a}{kT}\right) \qquad [4.1]$$

This is indicative of thermally activated hopping transport with a hopping activation energy of $E_a = 144meV$ for a photon energy of $hv = 1.8eV$, $E_a = 56.6meV$ for a photon energy of $hv = 3eV$, and $E_a = 60.6meV$ for a photon energy of $hv = 3.8eV$ at zero bias.

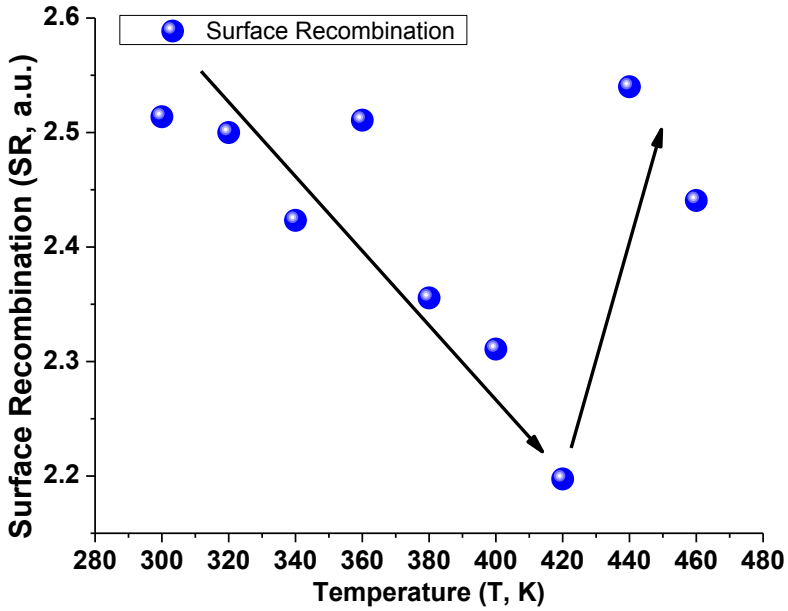

Figure 4.27: Ratio of surface recombination measured in the a-Si:H/a-GeSi:H photovoltaic device in function of the operating temperature

The ratio of surface recombination in function of the operating temperature is shown in Figure 4.27. In this figure the ratio of surface recombination shows two different regions with different behavior: the first one from 300 to $420°K$ and the second one from 420 to $460°K$. In the first region, the ratio of surface recombination decreases from $SR = 2.5$ to $2.2 a.u.$ but in the second region the ratio of surface recombination increases from $SR = 2.2$ to $2.5 a.u.$. The interpretation of these data is not so single because the operating temperature used in these measurements is higher than the

temperature used for the film deposition. At this temperature the film might suffer thermal annealing.

4.3.4 Diagnostic of the Thin Film Photovoltaic Devices by means of the Dark Current-Voltage Characteristics

Figure 4.28 shows the dark current-voltage characteristics measured in the processes 1075, 1076, 1078, 1079 and 1086. In this figure we can see that the structural configuration of the photovoltaic devices affects considerably the current measured with reverse and forward polarization. To diagnose to the photovoltaic devices, in this section will be consider the information extracted from the dark current-voltage characteristics with forward polarization. The methodologies used to extract the diagnostic characteristics are shown in section 3.3.5.

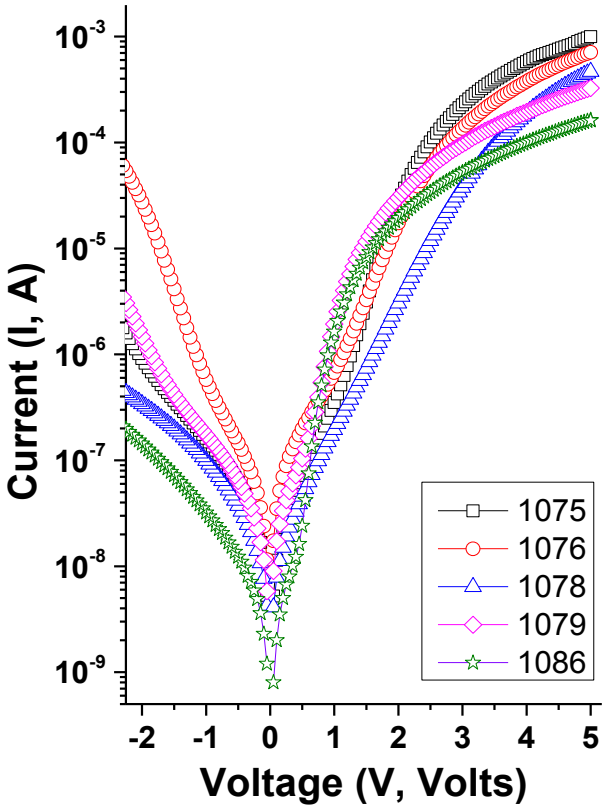

Figure 4.28: Dark I-V characteristics measured on $Ge_{0.97}Si_{0.03}$:H/a-Si:H devices deposited by low frequency plasma at the installations of INAOE

Figure 4.29a shows the results obtained in the processes 1075, 1076, 1078, 1079, and 1086. Figure 4.29b shows the results of the processes 1115, 1109 and 1114. In Figure 4.29a we can see that by varying the thickness of the intrinsic film of a-Si:H located between the p-i interface of the device from 500 to 630Å and maintaining fixed the thickness of the intrinsic film of a-Si:H located between the n-i interface of the device, the diode ideality factor increases from $n = 8.22$ to 13.69. After, by reducing the thickness of the intrinsic film of a-Si:H located between the n-i interface of the device from 500 to 0Å and increasing the thickness of the intrinsic film of a-Si:H located between the p-i interface of the device from 630 to 1071Å, we reduce the diode ideality factor from $n = 13.69$ to 3.41.

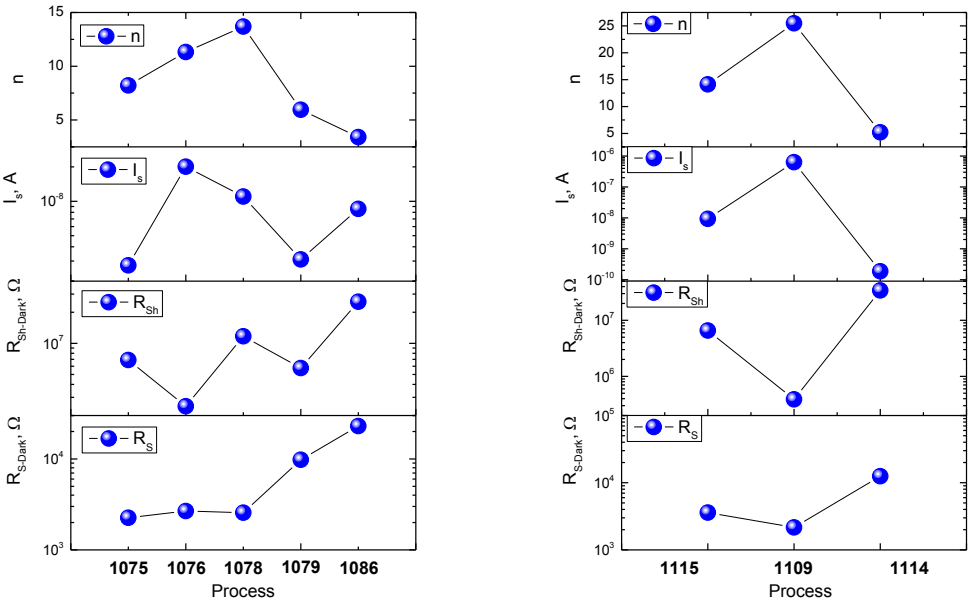

(a) **(b)**

Figure 4.29: Parameters extracted from dark I-V characteristics a) before and b) after laboratory maintenance

In Figure 4.29b we see that by reducing the thickness of the intrinsic film of $Ge_{0.97}Si_{0.03}$:H from 9200 to 7600Å and by increasing the thickness of the intrinsic film of a-Si:H from 1070 to 1300Å, the diode ideality factor increases from $n = 14.13$ to

25.48. After, by reducing the thickness of the intrinsic film of $Ge_{0.97}Si_{0.03}$:H from 7600 to 6100Å and by reducing the thickness of the intrinsic film of a-Si:H from 1300 to 1070Å, we reduce the diode ideality factor from $n = 25.48$ to 5.21. The saturation current showed a behavior similar to that observed in the diode ideality factor. On the other hand, Shunt resistance (see Figure 4.29a) did not vary systematically but increases with the increasing of the thickness of the intrinsic film of a-Si:H located between the p-i interface of the device from 500 to 1071Å and by reducing the thickness of the intrinsic film of a-Si:H located between the n-i interface of the device from 500 to 0Å. In Figure 4.29b, the Shunt resistance reduces when we increase the thickness of the intrinsic film of a-Si:H located between the p-i interface of the device from 1070 to 1300Å and reduce the thickness of the intrinsic film of $Ge_{0.97}Si_{0.03}$:H from 9200 to 7600Å. The shunt resistance increases when we increase the thickness of the intrinsic film of a-Si:H located between the p-i interface of the device from 1300 to 1070Å and reduce the thickness of the intrinsic film of $Ge_{0.97}Si_{0.03}$:H from 7600 to 6100Å. Series resistance showed a similar behavior to the behavior observed in the Shunt resistance.

Summary

In this section the dark current-voltage characteristics were used to diagnostic the performance of the photovoltaic devices deposited at the installation of the INAOE. The results shows that the Series resistance increase when we increase the thickness of the intrinsic film of a-Si:H located between the p-i interface and reduce the thickness of the intrinsic film of a-Si:H located between the n-i interface of the device. If the series resistance is large, the performance characteristics are deteriorated. However, the current-voltage characteristics measured under illumination and the spectral response of the short-circuit current showed that by increasing the thickness of the intrinsic film of a-Si:H located between the p-i interface of the device, the performance characteristics are improved due to that the carriers photogenerated in this film are

increased. To reduce the series resistance and improve the performance of photovoltaic devices without increasing the thickness of the intrinsic film of a-Si:H, we must eliminate the pontencial barrier located between the interface of the intrinsic films of a-Si:H and $Ge_{0.97}Si_{0.03}$:H. This barrier avoid that the holes photogenerated in the intrinsic film of $Ge_{0.97}Si_{0.03}$:H contribute to the performance of the photovoltaic devices.

The diode ideality factor shows that by increasing the thickness of the intrinsic film of a-Si:H located between the p-i interface of the device, the diode in the structure becomes more leaky. But the diode improves when we eliminate the intrinsic film of a-Si:H located between the n-i interface of the device. The value of the diode ideality factor in this structures is higher than the value of the conventional p-i-n structures. Shunt resistance and saturation current do not show systematic behaviors but the Shunt resistance increase when we increase the thickness of the intrinsic film of a-Si:H located between the p-i interface of the devices.

Diode ideality factor and saturation current show that by reducing the total length of the device, the diode in the structure improves. Shunt and Series resistances increased in this case.

4.3.5 Diagnostic of the Thin Film Photovoltaic Devices by means of Sub-gap Short-Circuit Current

The spectral response of sub-gap short-circuit current measured in the a-Si:H/$Ge_{0.97}Si_{0.03}$:H photovoltaic devices are shown in Figure 4.30. To characterize the defects in photovoltaic devices we used the ratio of the short-circuit current measured at the photon energy corresponding to defects $hv = 0.8eV$ and the short-circuit current measured at the photon energy corresponding to the optical band gap $hv = 1.2eV$ (see section 3.3.6 from Chapter 3: Methdologies and Characterization Techniques). To characterize the width of the band tail of the optical bandgap we used the parameter $E_{U_{pc}}$. The values of these parameters are shown in Figure 4.31.

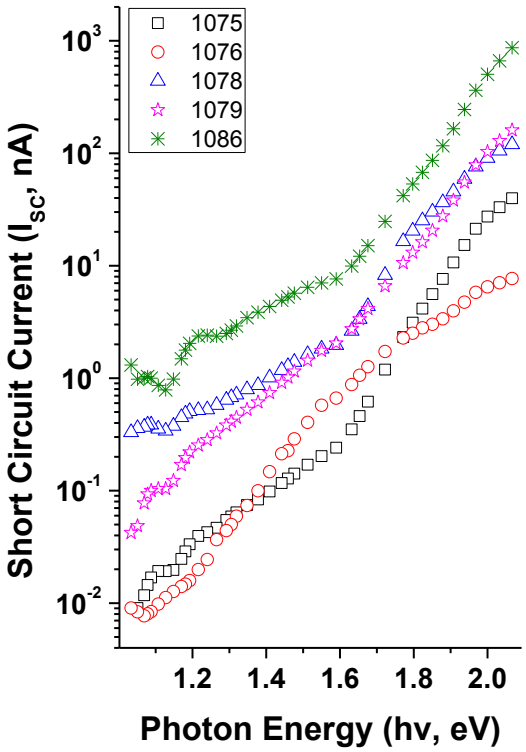

Figure 4.30: Sub-gap characteristics measured on a-Si:H/$Ge_{0.97}Si_{0.03}$:H photovoltaic devices deposited at INAOE installations

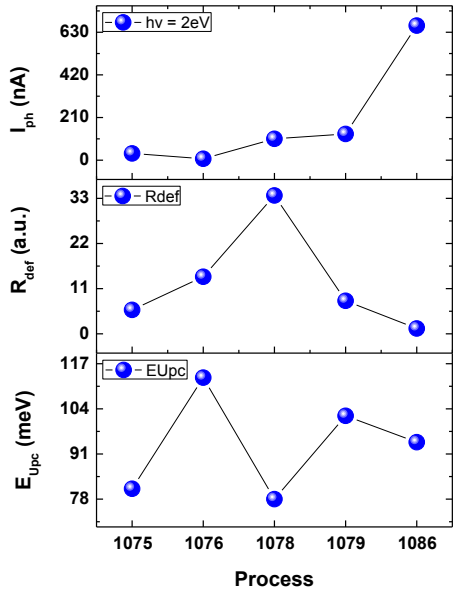

Figure 4.31: Parameters extracted from the spectral characteristics of subgap absoption measured in the devices of a-Si/$Ge_{0.97}Si_{0.03}$:H photovoltaic devices

In general, in Figure 4.31 we can see that the short-circuit current measured at a photon energy of $hv = 2eV$ increases when we increase the thickness of the intrinsic film of a-Si:H located between the p-i interface of the device and when we remove the intrinsic film of a-Si:H located between the n-i interface of the device. On the other hand, the ratio of defects increases with the increasing of the thickness of the intrinsic film of a-Si:H located between the p-i interface of the device but reduce with the elimination of the intrinsic film of a-Si:H located between the n-i interface of the device. The parameter $E_{U_{pc}}$ do not have a systematically behaviour as is shown in Figure 4.31.

4.4 Performance Characteristics of Photovoltaic Devices Fabricated with Different Semiconducting Materials

Figure 4.32 shows the performance characteristics measured in the µc-Si:H, pm-Si:H, a-Si:H/$Ge_{0.97}Si_{0.03}$:H and organic photovoltaic devices. In this figure we can see that depending on the material used, the performance of photovoltaic devices varies in a different way when we change the operating point of the photovoltaic devices. For example, in this Figure we can see that the highest current was obtained in the µc-Si:H photovoltaic device. The optical bandgap of the µc-Si:H thin film is narrower than the optical bandgap of the pm-Si:H thin film. Therefore, the µc-Si:H thin film can absorb photons with longer wavelengths from the solar spectrum in comparison with the pm-Si:H thin film and hence produce higher photocurrent. On the other hand, the open-circuit voltage of the µc-Si:H photovoltaic device has the lowest value in comparison with the other photovoltaic devices. The pm-Si:H photovoltaic device has the highest value of the open-circuit voltage.

The a-Si:H/$Ge_{0.97}Si_{0.03}$:H device is composed of $Ge_{0.97}Si_{0.03}$:H thin films with an optical band gap of about $E_{opt} \approx 1.2eV$. This value of optical bandgap would make us expect a value of current similar to the value obtained in the µc-Si:H photovoltaic

device but in Figure 4.32 we can see that the value of the current obtained in this device has the lowest value in comparison with the other photovoltaic devices. In Figure 4.32 we also can see that when we increase the value of the load resistance, the value of the current obtained in the a-Si:H/$Ge_{0.97}Si_{0.03}$:H photovoltaic device reduces faster than in the other photovoltaic devices. This behavior indicate us that the parasitic elements (i.e., leakage current, surface recombination, parasitic resistances, etc.) have a more pronounced effect on the a-Si:H/$Ge_{0.97}Si_{0.03}$:H photovoltaic device in comparison with the photovoltaic devices of µc-Si:H and pm-Si:H.

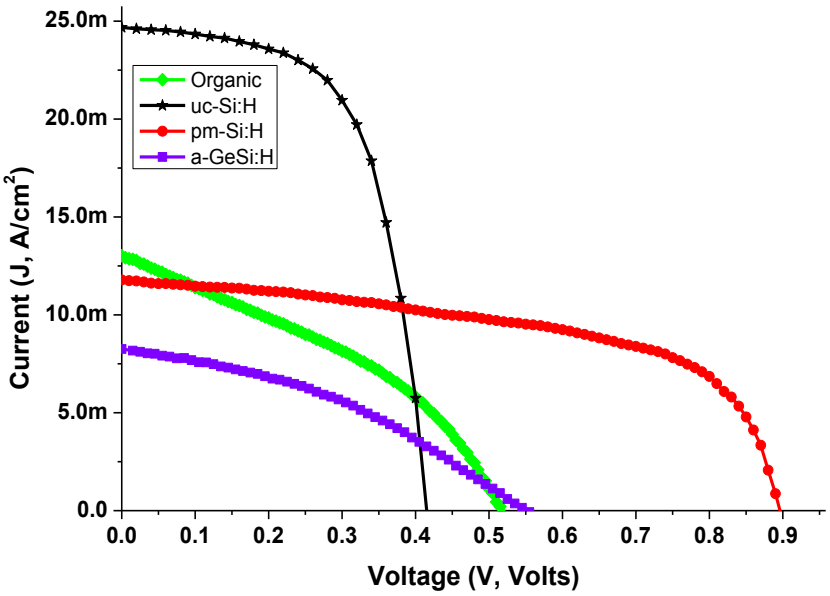

Figure 4.32: I-V characteristics measured under illumination in pm-Si:H, µc-Si:H, a-Si:H/a-$Ge_{0.97}Si_{0.03}$:H, and organic photovoltaic devices

The value of the open-circuit voltage of the a-Si:H/$Ge_{0.97}Si_{0.03}$:H photovoltaic device is higher than the value of the open-circuit voltage of the µc-Si:H photovoltaic device. This behaviour could indicates us that the value of optical bandgap in the a-Si:H/$Ge_{0.97}Si_{0.03}$:H photovoltaic device is higher than the value of the optical bandgap in the µc-Si:H photovoltaic device or a smaller surface recombination in the photovoltaic device of a-Si:H/$Ge_{0.97}Si_{0.03}$:H. The physics of organic photovoltaic device is governed by different operating mechanisms than the operating mechanisms

of the devices previously mentioned. However, we can observe that by varying the value of the load resistance the value of the current decreases faster than the value of the current of the a-Si:H/$Ge_{0.97}Si_{0.03}$:H photovoltaic device. Organic material device is capable to provide more current than the polymorphous silicon device but its open circuit voltage is lower. In general, we can see that the organic material and a-Si:H/$Ge_{0.97}Si_{0.03}$:H technologies need more development to reach a more optimal performance.

4.5 Spectral Characteristics of the Photovoltaic Devices Fabricated with Different Semiconducting Materials

Figure 4.33 shows the spectral characteristics of the µc-Si:H, pm-Si:H, $Ge_{0.97}Si_{0.03}$:H and organic photovoltaic devices. The solid line represents the spectrum of solar radiation. In this figure we can see that the surface recombination velocity is higher in the µc-Si:H photovoltaic device because the photocurrent measured within the energy range from $hv = 3$ to $3.8eV$ decreases faster in comparison to the photocurrent measured in the other photovoltaic devices.

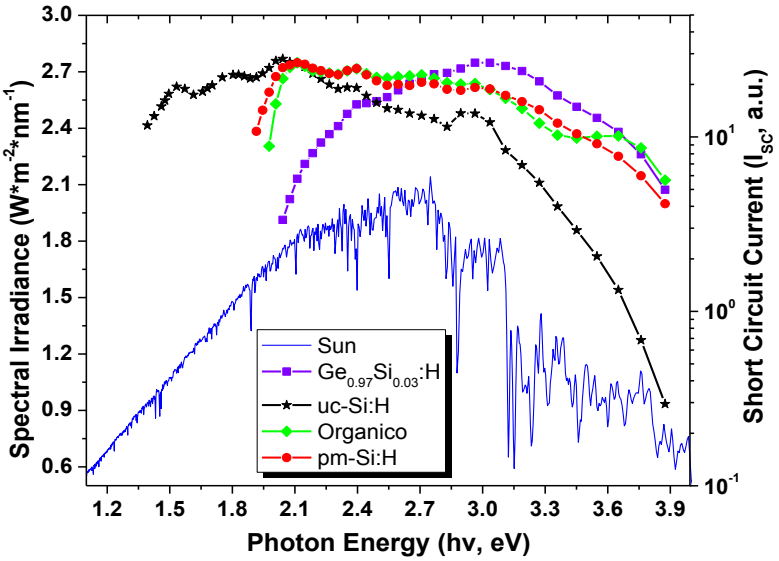

Figure 4.33: Comparison of spectral characteristics measured in pm-Si:H, µc-Si:H, a-Si:H/$Ge_{0.97}Si_{0.03}$:H, and organic photovoltaic structures

On the other hand, the μc-Si:H photovoltaic device can also absorb longer wavelengths (lower photon energy) of the solar spectrum compared with the other photovoltaic devices as is shown in Figure 4.33. The behavior of the photocurrent measured in the other three devices showed no significant change in the same photon energy range. Within the energy range from $hv = 2$ to $2.6eV$, the photocurrent measured in the a-Si:H/$Ge_{0.97}Si_{0.03}$:H device reduces faster compared to the photocurrent measured in the pm-Si:H and organic photovoltaic devices. This behavior has been attributed to the width of the optical bandgap of the a-Si:H thin films of the a-Si:H/$Ge_{0.97}Si_{0.03}$:H device, which apparently controls the performance of the photovoltaic device. The trend observed in the pm-Si:H and organic photovoltaic devices is very similar in both cases, indicating that the width of the optical band gap may be similar in the two devices.

4.6 Dark Current-Voltage Characteristics of Photovoltaic Devices Fabricated with Different Semiconducting Materials

Figure 4.34 shows the dark current-voltage characteristics measured in the μc-Si:H, pm-Si:H, a-Si:H/$Ge_{0.97}Si_{0.03}$:H and organic photovoltaic devices. All the structures demonstrated rectification behavior. a-Si:H/$Ge_{0.97}Si_{0.03}$:H had lower reverse and forward current. pm-Si:H had higher reverse and forward current followed by μc-Si:H and organic photovoltaic devices. The voltage corresponding to injection in forward direction is higher in the a-Si:H/$Ge_{0.97}Si_{0.03}$:H (starting at about $V = 0.8V$). This value is similar to the value of the pm-Si:H which start at about $V = 0.75V$. The voltage corresponding to injection in forward direction is $0.37V$ and $0.33V$ in organic and μc-Si:H photovoltaic devices, respectively. In a-Si:H/$Ge_{0.97}Si_{0.03}$:H and pm-Si:H at lower bias voltage as it can be seen in Figure 4.34 the current is controlled by the shunt resistance $R_{Sh-Dark}$. The parameters extracted from the dark current-voltage characteristics are summarized in Table 4.3.

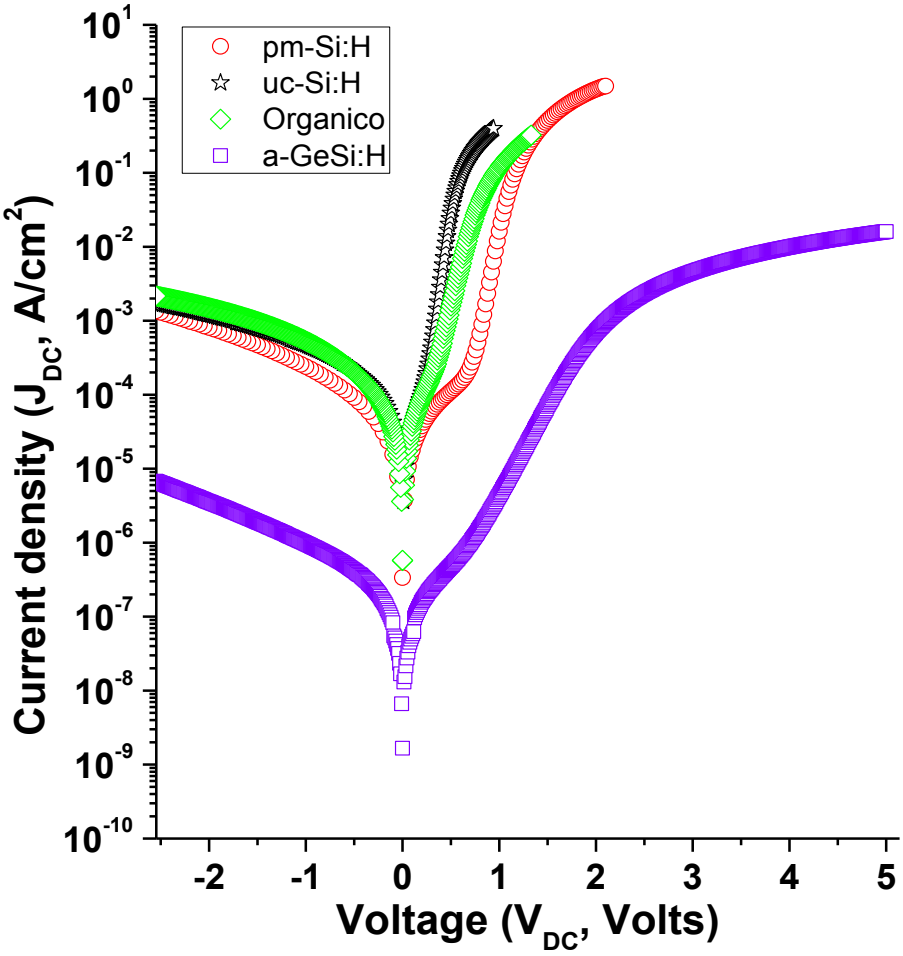

Figure 4.34: Dark I-V characteristics obtained on pm-Si:H and uc-Si:H PIN Structure

Table 4.3: Parameters extracted from Dark I-V Characteristics

Parameter	Dark I-V characteristics			
	pm-Si:H	µc-Si:H	a-Si:H/a-GeSi:H	Organic
	Forward Bias			
n	2.40 ± 0.01	1.74 ± 0.01	3.41 ± 0.04	3.12 ± 0.01
J_s [A/cm^2]	(1.7 ± 0.4)*10^{-9}	(5.1 ± 0.2)*10^{-7}	(8.58 ± 0.06)x10^{-9}	(3.27 ± 0.06)*10^{-6}
$R_{Sh\text{-}Dark}$ [Ω]	(1.37 ± 0.01)*10^5	(2.05 ± 0.02)*10^4	(2.53 ± 0.09)x10^7	(8.9 ± 0.1)*10^4
$R_{s\text{-}Dark}$ [Ω]	16.5	7.37	2.3x10^4	39.38
F_R	1.67x10^3	9.07x10^2	2.01x10^2	2.19x10^2

It was observed that the diode ideality factor $n = 1.74$ is better in µc-Si:H device in comparison with that $n = 2.4$, 3.12 and 3.41 for pm-Si:H, organic and a-Si:H/$Ge_{0.97}Si_{0.03}$:H devices suggesting in the latter current losses either in volume or at

the p-i, n-i interfaces. Organic photovoltaic device demonstrate higher saturation current and reverse bias current density J_s and J_r. In this case the higher J_s and J_r values seem to be related to higher "parasitic" current because of both factor: recombination current in the bulk and/or interfaces and current through shunt resistance. Lower $R_{Sh-Dark}$ and R_{S-Dark} were obtained in μc-Si:H samples because of high conductivity of μc-Si:H films. pm-Si:H device demonstrate higher rectification ratio, $F_R = 1.67x10^3$, followed by μc-Si:H with a value of $F_R = 9.07x10^2$. Similar values of rectification ratio were obtaind in organic and a-Si:H/a-GeSi:H devices. Reverse bias current density at voltage bias $V > 0V$ becomes practically the same in the structures of organic, μc-Si:H and pm-Si:H devices in comparison with a-Si:H/$Ge_{0.97}Si_{0.03}$:H device.

4.7 Losses Caused by the Parasitic Resistances in the Photovoltaic Devices Fabricated with μc-Si:H and pm-Si:H Thin Films

The current-voltage characteristics under illumination are depicted in Figure 4.35 for pm-Si:H and μc-Si:H p-i-n structures. In both structures the efficiency is approximately the same ($\eta = 6.64\%$ for pm-Si:H and $\eta = 7.07\%$ for μc-Si:H) but short circuit current density and fill factor is larger in μc-Si:H ($J_{sc} = 25.3mA/cm^2$ and $FF = 0.63$) than those in pm-Si:H ($J_{sc} = 11.8mA/cm^2$ and $FF = 0.56$). The open circuit voltage is larger in pm-Si:H ($V_{oc} = 0.89V$) than in μc-Si:H ($V_{oc} = 0.42V$). The current-voltage curves in Figure 4.35 describe the behavior of the experimental samples i.e. include effects of both $R_{Sh-Light}$ and $R_{S-Light}$ and do not allow us to see behavior of the junctions themselves (diodes).

Data similar to those obtained from current-voltage without $R_{Sh-Light}$ and $R_{S-Light}$ analysis shown in Figure 4.35 are commonly published. These data do not provide information on junctions making comparison ambiguous and misleading as it will be shown further. Our more detailed study of current-voltage together with analysis of the

model in Figure 3.5 revealed that the diode in polymorphous silicon structure has a higher efficiency $\eta = 9.3\%$ with $FF = 0.77$ (see Figure 4.35, and Figure 4.36a) than that for the diode in microcrystalline silicon structure $\eta = 7.86\%$ with $FF = 0.72$ (see Figure 4.35, and Figure 4.36b).

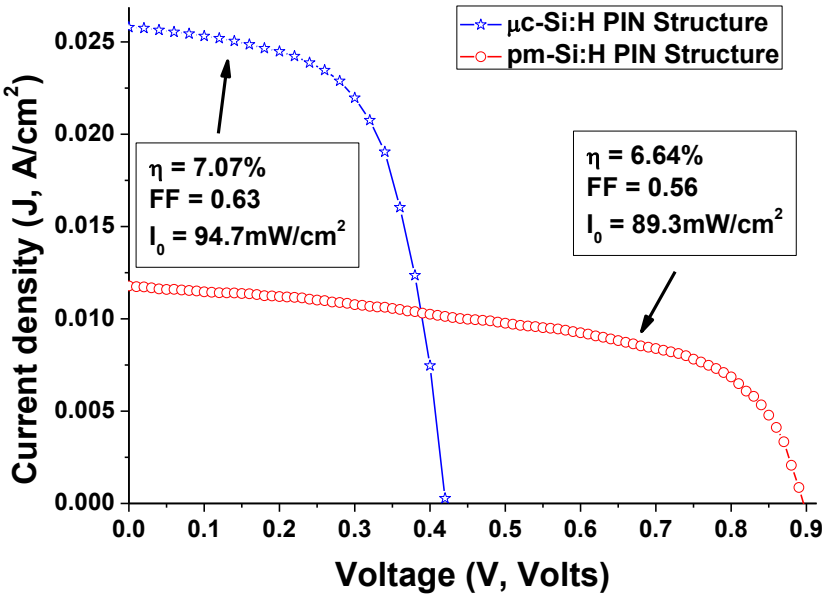

Figure 4.35: Current-voltage characteristics of p-i-n diodes illuminated with the light of sun through the p+layer

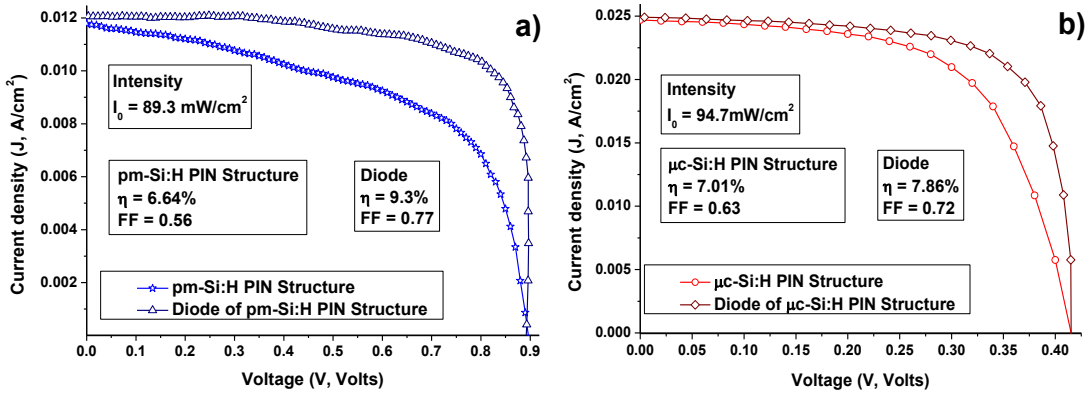

Figure 4.36: Current-voltage characteristics for the a) pm-Si:H and b) µc-Si:H PIN structures and corresponding diodes under sun illumination

Table 4.4: Parameters of p-i-n pm-Si:H and µc-Si:H structures extracted from the current-voltage characteristics under illumination

Parameter	Parameters from I-V characteristics under illumination			
	Experimental PIN structure		Diode (w/o R_s, R_{sh})	
	pm-Si:H	µc-Si:H	pm-Si:H	µc-Si:H
Light Intensity [mW/cm^2]	89.3	94.07	89.3	94.07
J_m [mA/cm^2]	8.12	20.77	10.34	21.2
V_m [Volts]	0.73	0.32	0.80	0.35
J_{sc} [mA/cm^2]	11.78	25.3	11.78	25.3
V_{oc} [Volts]	0.89	0.42	0.89	0.42
FF	0.56	0.63	0.77	0.72
η [%]	6.64	7.01	9.3	7.86
$R_{s\text{-}Light}$ [Ω]	247 ± 5	20.5 ± 0.6	0	∞
$R_{Sh\text{-}Light}$ [Ω]	(1.09 ± 0.02)*10^4	(2.9 ± 0.2)*10^3	0	∞

Figure 4.36a shows that the shunt ($R_{Sh-Light} = (1.09 \pm 0.02) * 10^4\Omega$) and series ($R_{S-Light} = (247 \pm 5)\Omega$) resistances of pm-Si:H reduce the efficiency from $\eta = 9.3\%$ to $\eta = 6.64\%$ (i.e. about 30% of the value). While data in Figure 4.36b show that the shunt ($R_{Sh-Light} = (2.9 \pm 0.2) * 10^3\Omega$) and series ($R_{S-Light} = (20.5 \pm 0.6)\Omega$) resistances of µc-Si:H reduce the efficiency from $\eta = 7.86\%$ to $\eta = 7.01\%$ (i.e. about 12% of the value). Thus the losses because of shunt and series resistances in the pm-Si:H p-i-n structure are higher than those in µc-Si:H. In pm-Si:H the resistances reduce the fill factor from $FF = 0.77$ to 0.56, and in the µc-Si:H reduce from $FF = 0.72$ to 0.63. The characteristics measured in both structures are summarized in Table 4.4.

4.8 Effect of Temperature on the Performance Characteristics of the µc-Si:H Photovoltaic Device

Figure 4.37 shows the current-voltage characteristics measured under illumination conditions in the µc-Si:H p-i-n structure. During the measurements, the temperature of the p-i-n structure was varied over a range from 300 to 480°K. The sample was illuminated through the n-contact back by means of a halogen lamp. From the current-voltage characteristics were obtained the values of the open-circuit voltage, short-circuit current, fill factor, and energy-conversion efficiency for each temperature.

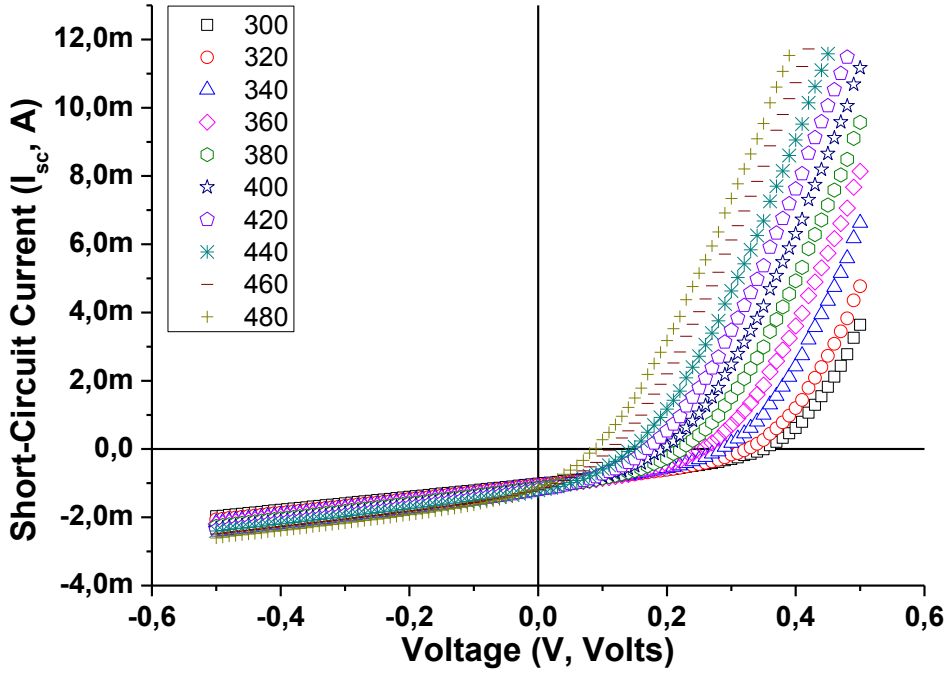

Figure 4.37: I-V characteristics measured in the µc-Si:H pin structure as a function of temperature

In Figure 4.38 is shown the (a) open-circuit voltage and (b) short-circuit current measured in a µc-Si:H pin structure as a function of temperature. In Figure 4.38(a) is possible to observe that the open-circuit voltage measured in the µc-Si:H pin structure linearly decreases with the increasing temperature. The linear fit realized to the data of the Figure 4.38(a) revealed that the open circuit voltage decrease at a ratio of $m_{temp} = -1.48 mV/°C$. That is, the open circuit voltage decreases by about 0.42% per °C. The behavior observed in the open circuit voltage is similar to the behavior observed in crystalline materials. From an extrapolation to $T = 0°K$ on a $V_{oc}\ vs\ T$ plot, the activation energy may be obtained. In crystalline materials the activation energy represents bulk recombination if E_a is equal to the bandgap energy. If it is less than the bandgap energy, then interface recombination is the limiting mechanism. An extrapolation to the zero degree value gives $E_a = 0.789eV$. This is less than the bandgap of the absorber which indicates that the dominant limiting transport mechanism under illumination is interface recombination or via some band-tail sates.

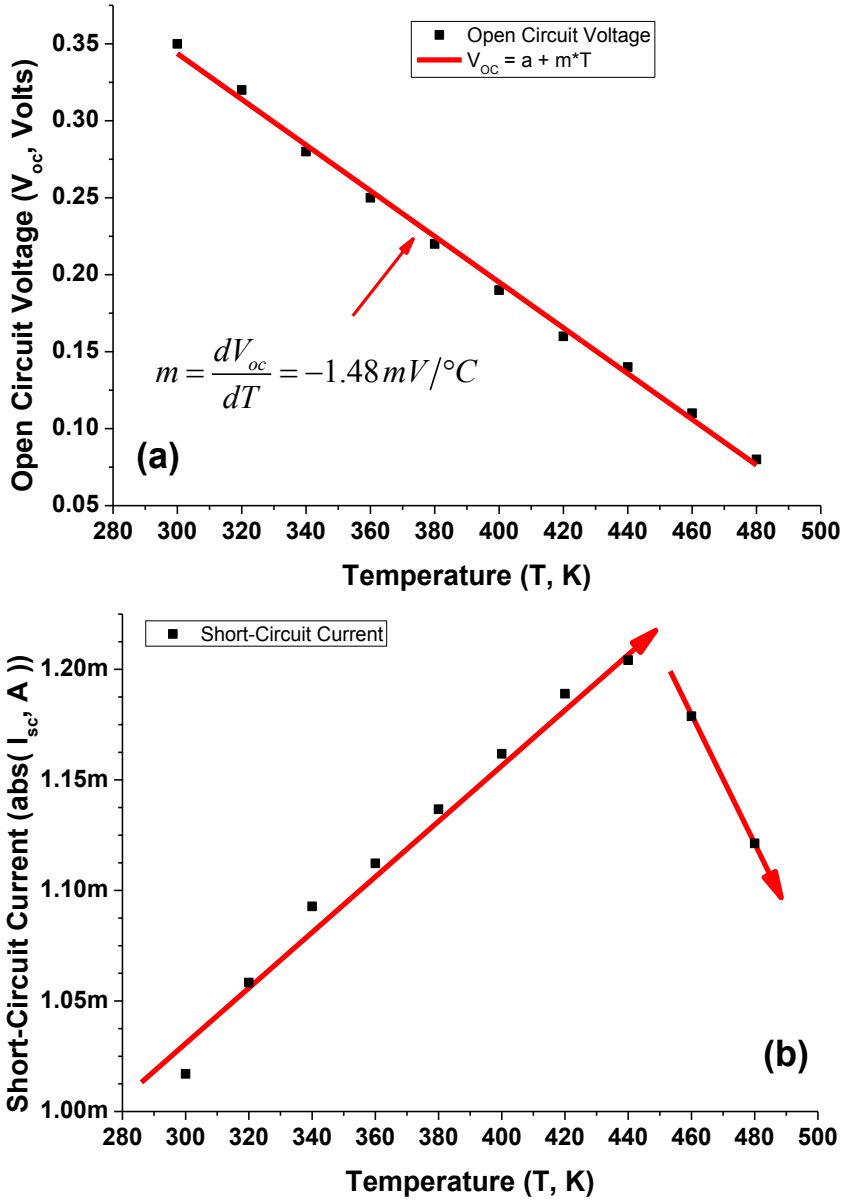

Figure 4.38: Shows the open circuit voltage and short-circuit current measured in the µc-Si:H pin structure as a function of temperature

The short-circuit current shown in Figure 4.38(b) do not present a continuous tendency in function of the temperature but his value increases slightly with the increasing temperature, owing to decreasing optical gap and correspondingly increased absorption coefficient across the spectrum. This is indicative of thermally activated hopping transport with a hopping activation energy of $E_a = 13.4meV$ at zero bias.

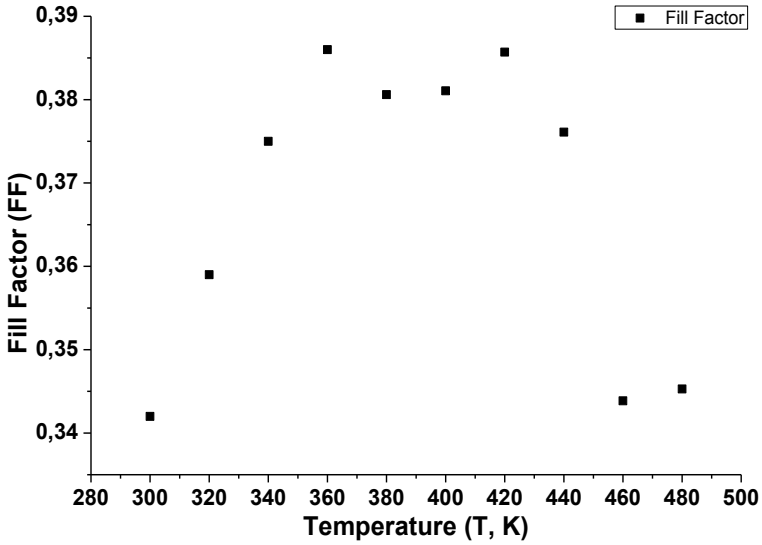

Figure 4.39: Shows the fill factor obtained in the µc-Si:H pin structure as a function of temperature

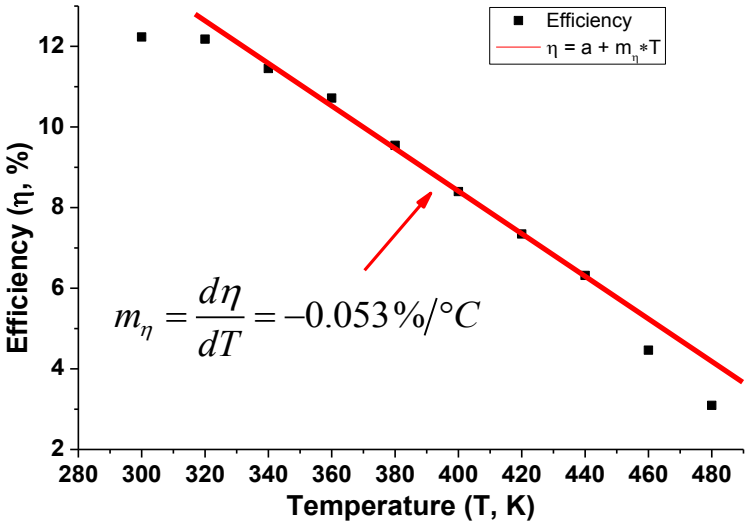

Figure 4.40: Shows the energy-conversion efficiency obtained in the µc-Si:H pin structure as a function of temperature

In Figure 4.39 is shown the fill factor obtained from the current-voltage characteristics measured in the µc-Si:H pin structure under illumination. In this Figure the fill factor increases when the temperature increases from $T = 300$ to $420K$ and reduces when the temperature increases from $T = 420$ to $480K$. The increase of the fill factor may be due to decreasing resistance effects or increasing 'mobility-lifetime'

products within the collection region for non-crystalline solar cells. The behavior observed in the fill factor is in contrast with the behavior observed in crystalline solar cells in which the fill factor reduce with the increasing temperature. Finally, in Figure 4.40 is shown the energy-conversion efficiency measured in the μc-Si:H pin structure. The linear fit realized to the data of the Figure 4.40 revealed that the energy-conversion efficiency decrease at a ratio of $m_{temp} = -0.053\%/℃$. That is, the energy conversion efficiency decreases by about 0.43% per ℃.

4.9 Spectral Characteristics of the Photovoltaic Devices Fabricated with μc-Si:H and pm-Si:H Thin Films

The spectral dependence of photocurrent was normalized to the constant intensity of $I_o = 0.99 mW/cm^2$. The parameter similar to Urbach energy E_{Upc} was obtained in the region where the short circuit current exhibits an exponential dependence of energy $I_{sc} = I_0 * exp(hv/E_{Upc})$. In order to characterize defects we used a ratio of short circuit current at arbitrary selected photon energy corresponding to the defects: $hv = 1.07eV$ and $hv = 0.94eV$ for pm-Si:H p-i-n and for μc-Si:H p-i-n, respectively, to photon energy corresponding to optical gap $E_g = 1.77eV$ and $E_g = 1.15eV$ for pm-Si:H p-i-n and for μc-Si:H p-i-n, respectively. This selection of the range for defect characterization is based on the assumption that tail states extension does not exceed $0.3eV$. In the pm-Si:H p-i-n structure, the defects ratio was calculated as $R_{def} = \left(I_{sc}(hv = 1.07eV)/I_{sc}(hv = 1.77eV)\right)$. In the μc–Si:H p-i-n structure, the defects ratio was determined as $R_{def} = \left(I_{sc}(hv = 0.94eV)/I_{sc}(hv = 1.15eV)\right)$.

The spectral responses for short circuit current $I_{sc}(hv)$ are shown in Figure 4.41 for pm-Si:H and μc-Si:H p-i-n structures. In the latter we observed that the $I_{sc}(hv)$ has a better response for low photon energy (from $hv = 0.75$ through $1.8eV$) and a worse one for high photon energy $hv > 2.7eV$ in comparison to that for polymorphous silicon

structure. This difference results apparently from the difference in optical bandgaps (the values of optical bandgap estimated from the curves in Figure 4.41 are as follows $E_g \approx 1.77eV$ and $1.15eV$ for pm-Si:H and µc-Si:H, respectively). pm-Si:H p-i-n demonstrated, however, better by about one order of magnitude response for high energy photons $hv > 3.2eV$ suggesting lower surface recombination at the frontal interface. $I_{sc}(hv)$ at photon energy below optical gap is determined by spectral dependence of $\alpha\mu\tau$–product where α is the absorption coefficient, μ is the carrier mobility and τ is the carrier life-time. Assuming that quantum yield $\eta = 1$ and $\mu\tau$ does not depend on photon energy $I_{sc}(hv)$ is determined by $\alpha(hv)$ for sub-gap absorption.

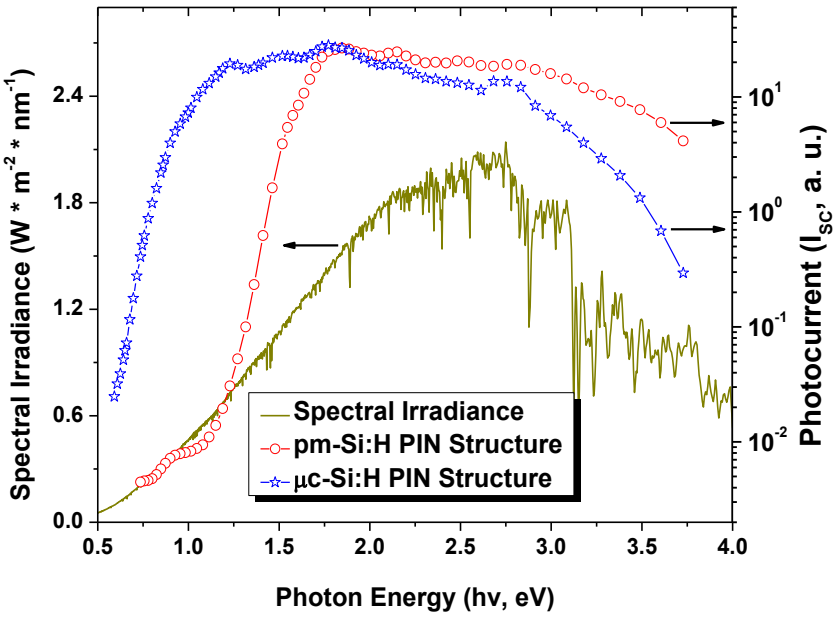

Figure 4.41: Spectral dependence of the short circuit current I_{sc} (hv) for both pm-Si:H p-i-n and µc-Si:H p-i-n structures

Under these assumptions it is possible to characterize the spectral response in this range by means of characteristic energy E_{Upc} similar to Urbach energy in $\alpha(hv)$ and by the defect ratio $R_{def} = I_{sc}(hv = E_{def})/I_{sc}(hv = E_g)$. Boundary between tail and defect states notified here as defect energy was accepted as $E_{def} = 0.94eV$ for µc-Si:H

and $1.07eV$ for pm-Si:H. The data obtained show that the density of states related to the tails within the optical gap is slightly higher in pm-Si:H ($E_{Upc} = 52meV$) than that in µc-Si:H ($E_{Upc} = 49meV$) sample.

The defect ratio value R_{def} characterizing deep localized states obtained for pm-Si:H $R_{def} = 1.3x10^{-3}$ was close to the value $R_{def} = 1.1x10^{-3}$ for µc-Si:H. Spectral characteristics reported in literature were measured in the range of $400\text{-}1000nm$, which did not allow to analyze sub-gap absorption and high photon response and consequently to characterize quality of i-layer and surface recombination at the frontal interface, respectively.

4.10 Effect of Temperature on the Dark Current-Voltage Characteristics of the µc-Si:H and pm-Si:H Photovoltaic Devices

Figure 4.42 shows the temperature dependence of dark current-voltage characteristics measured in (a) pm-Si:H and (b) µc-Si:H p-i-n photovoltaic devices. In both devices an increase of dark current is observed, when the temperature increases from $T = 300$ up to $480K$. This increase of current was observed in both forward and reverse polarization. However, the effect of temperature is stronger in forward polarization than that in reverse polarization.

The temperature dependence of series resistance extracted from current-voltage data is shown in Figure 4.43 for (a) pm-Si:H and (b) µc-Si:H p-i-n photovoltaic devices. In pm-Si:H photovoltaic device it was observed that the series resistance reduces from $R_S = 16.28$ to 7.46Ω when the temperature increase from $T = 300$ up to $480K$. This behavior is commonly observed in semiconductors in the case when this resistance is controlled by low field region (out of depletion) in the device. Another behavior is observed in microcrystalline device. In this case R_s increases with temperature and this is metal like behavior, which suggests dominating contribution of electrodes (or more

resistive one). Interpretation of both types of temperature dependence is not simple. Because if re-plot the graph in Figure 4.43(a) as $Log(1/R_s) = f(1/kT)$ we shall receive a curve with two slopes corresponding to activation energies $E_a = 0.037eV$ (in the range of $1/kT = 23 - 30(eV)^{-1}$) and $E_a = 0.067eV$ (in the range of $1/kT = 32 - 38(eV)^{-1}$). Both are small in comparison with activation energy of conductivity meaning that current passes via some states practically at the same energetical level, in other words by tunneling.

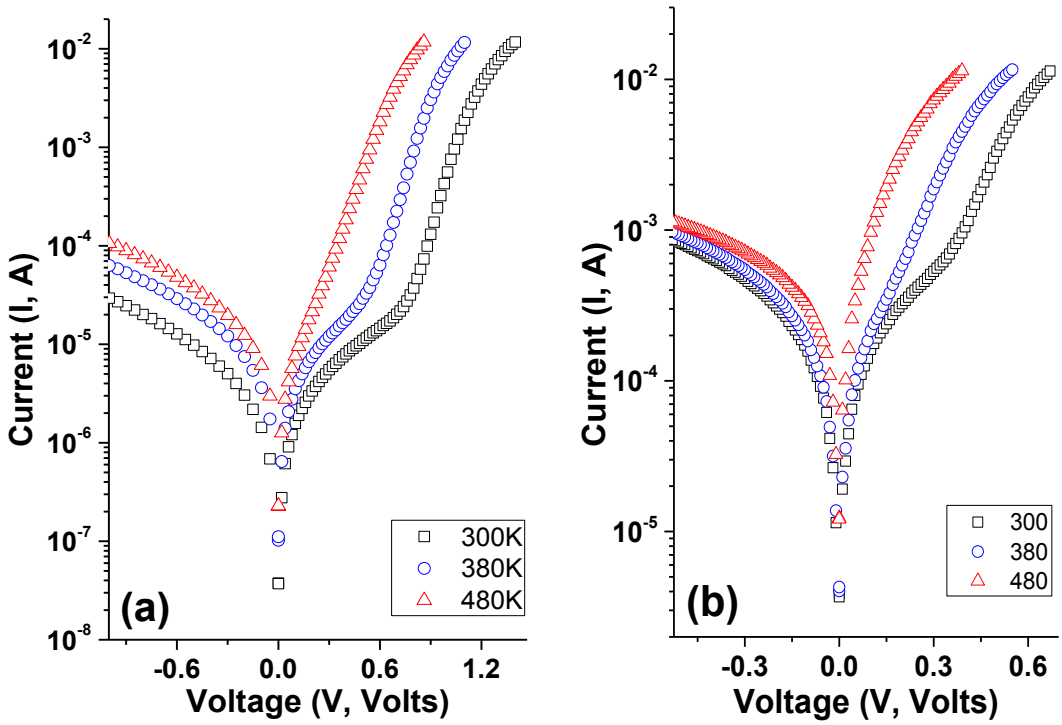

Figure 4.42: Dark current-voltage characteristics obtained in (a) polymorphous and (b) microcrystalline silicon PV structures at T = 300K (squares), 380K (circles) and 480K (triangles).

If consider graph of Figure 4.43b corresponding to metal like behavior and re-plot this graph as $Log[(R_s - R_{s0})/R_{s0}] = const * T^{\gamma}$ we shall obtain $\gamma = 1.83$, while linear dependence with $\gamma = 1$ could be expected for metal. Thus more study is required to make clear an origin of the observed behavior in both cases. Ideality factor n extracted for diodes as a function of temperature is shown in Figure 4.44(a) for

polymorphous and (b) for microcrystalline PV structures. We can see different behavior with temperature: if for pm-Si:H devices n increases with temperature, for µc-Si:H devices an opposite trend is observed.

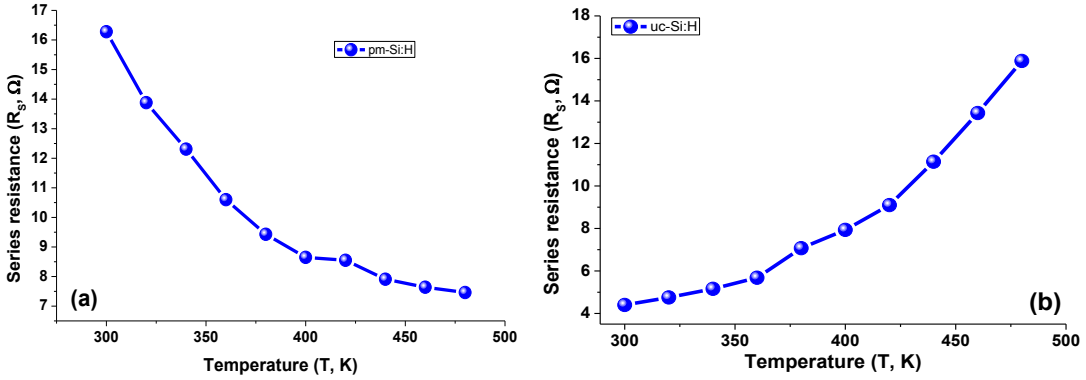

Figure 4.43: Temperature dependence of series resistance measured on (a) polymorphous and (b) microcrystalline silicon PV structures over a range from T = 300 to 480K.

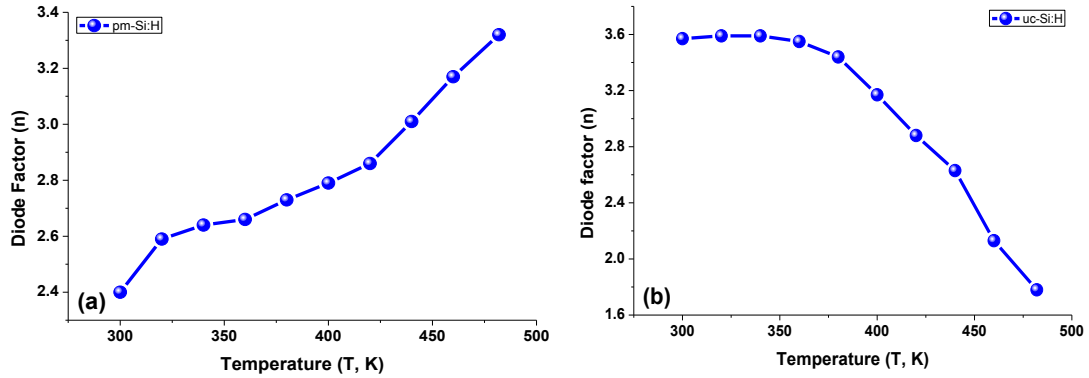

Figure 4.44: Temperature dependence of diode factor measured on (a) polymorphous and (b) microcrystalline silicon PV structures in the range from T = 300 to 480K.

Theory for crystalline p-n junction gives maximum value $n = 2$ in the case of strong recombination. While the observed data show remarkably higher values. In general larger n value corresponds to "leaky" diode (higher parasitic currents). Origin of "leaky" behavior in non crystalline materials is related not only to recombination

because of existence a great number of factors (surface states, leakage through some non junction channels, superficial leakage, etc.) for leakage current. It is interesting to notice different trends in temperature dependence of n value: pm-SiH devices become more "leaky" with temperature while µc-Si:H devices demonstrate clearly opposite trend becoming less "leaky" with temperature. We have at present not enough data to propose some reasonable interpretation for both cases.

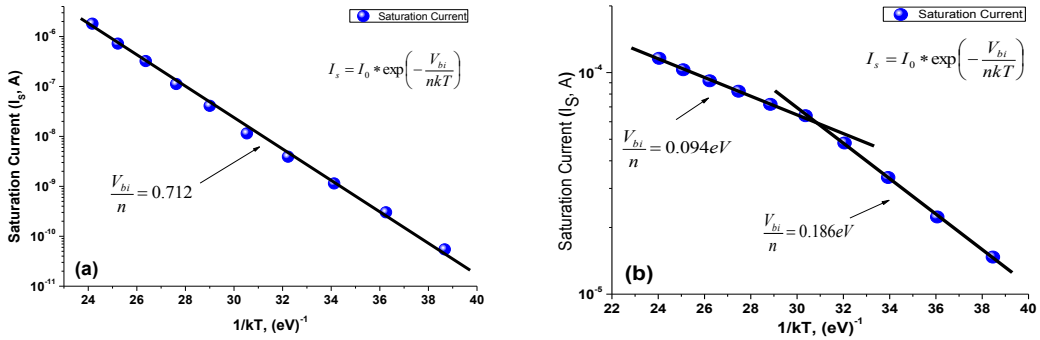

Figure 4.45: Temperature dependence of saturation current measured on (a) polymorphous and (b) microcrystalline silicon PV structures over the range from T = 300 to 480K.

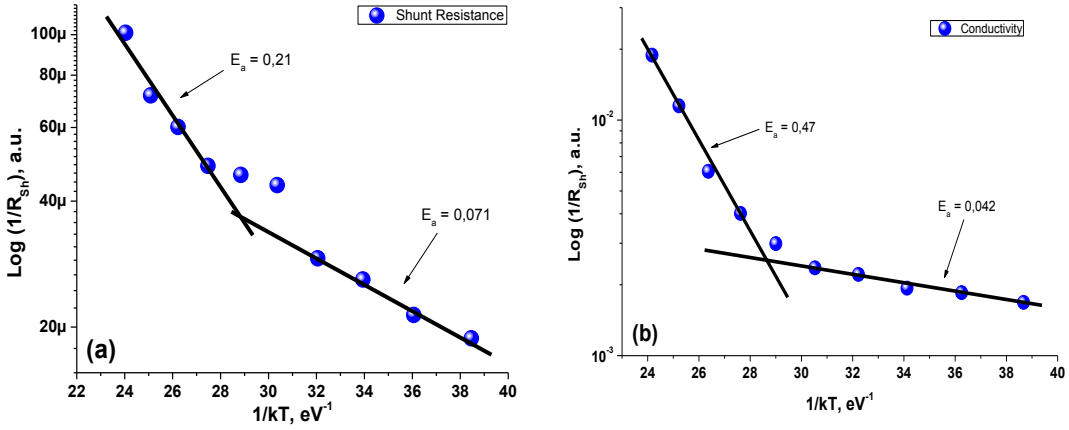

Figure 4.46: Temperature dependence of shunt resistance Rsh measured in (a) polymorphous and (b) microcrystalline silicon PV structures over a range from T = 300 to 480K.

Behavior of saturation current I_s with temperature presented in Figure 4.45 shows activation character with some slopes assigned to activation energies. pm-Si:H devices show clearly one activation energy, which can be attributed to built-in potential $E_a = eV_{bi}/n = 0.71$. Open circuit voltage V_{oc} cannot exceed V_{bi}. From experimental data for pm-Si:H $V_{oc\,exp} = 0.89V$ and $V_{bi\,max} = 1.7V$ and for µc-Si:H $V_{oc\,exp} = 0.42V$ and $V_{bi\,max} = 0.68V$, in other words built potential works more effective in µc-SiH structures.

Temperature dependence of shunt resistance in the form of $1/R_{Sh} = f(1/kT)$ to reveal activation character of the current through shunt resistance is shown Figure 4.46 for (a) pm-Si:H and for (b) µc-Si:H PV devices. Current-Voltage characteristics corresponding to current limited by shunt showed symmetrical behavior with polarization in entire range of temperature. Both curves demonstrate similar character dependence but with different values for activation energy. At room temperature and moderate heating (to about $T \approx 380K$) in both samples small activation energies $E_a = 0.071$ and $0.042eV$ for pm-Si:H and for µc-Si:H, respectively, are observed. They could be due to variable range hopping transport. And at high temperature $T > 380K$ activation energies increases reaching the values $E_a = 0.21eV$ and $0.47eV$ for pm-Si:H and µc-Si:H, respectively. For µc-Si:H devices activation energy observed is close to the value of Fermi level position meaning that shunt current flows through some fragments of area of the device, in other words junction does not occupy entire nominal area of the device and some parts work as resistance rather than junction contributing in R_{Sh}. For pm-Si:H devices activation energy $E_a = 0.21eV$ is remarkably less than energy of Fermi level. An origin of this kind of shunt current is unknown at present. It is reasonable to assume that shunt current could flow through some pores (and or defects on surface of the pores). Anyway the curves in Figure 4.46 demonstrate on one side similar trends and on other side difference in the values of activation energies.

Chapter 5

Discussion of the results

The silicon-germanium thin films have gained a great interest for the development of photovoltaic devices because the optical bandwidth can be adjusted by varying the germanium content in the alloy [5-7, 12, 13]. Furthermore, the silicon-germanium technology is also compatible with the amorphous silicon technology. Unfortunately, studies performed on silicon-germanium alloys have demonstrated that the density of deep defects increases with the increasing of the germanium content [17]. An increase of the density of deep defects deteriorates its photoelectrical properties. For this reason, in the state-of-art there is not much information about studies in silicon-germanium thin films and devices with high germanium content ($C_{Ge} > 50\%$) [2-41].

On the other hand, results obtained before the completion of this thesis showed that a small concentration of silicon ($C_{Si} = 3\%$) improved the photoelectric and structural properties of the silicon-germanium alloys with high content of germanium ($C_{Ge} = 97\%$) [42]. These preliminary results encouraged the development of photovoltaic devices studied in this thesis.

5.1 Optoelectronic Characteristics of $Ge_{0.97}Si_{0.03}$:H Thin Films

- The spectral response of the photocurrent is used commonly to characterize the performance of the films and photovoltaic devices [56, 59, 63, 65]. In the section 4.2, the spectral response of photoconductivity was used to characterize the structural disorder of the $Ge_{0.97}Si_{0.03}$:H thin films in function of the deposition temperature.

The structural disorder is characterized commonly using the spectral response of the absorption coefficient by means of the Urbach Energy (E_u) [42-44, 46, 50, 55]. In this thesis, the structural disorder was characterized by means of the defects ratio and the parameter E_{Upc} which were extracted from the spectral response of the photocurrent. The parameter E_{Upc} is similar to the Urbach Energy (E_u) but the parameter E_{Upc} takes into account the absorption by localized states in the optical band-tails, the drift mobility (μ_{drift}), and lifetime (τ) of the charge carriers. Results obtained in this thesis and in reference [68] shows that the magnitude of the parameter E_{Upc} is higher that the magnitude of the Urbach Energy (E_u) but the behavior observed is the same in both parameters.

The results obtained from the spectral response of the coefficient absorption allow us to characterize the density of localized states of the $Ge_{0.97}Si_{0.03}$:H thin films within the energy range from $hv = 0.95$ to $1.2eV$ [50]. In this thesis, the results obtained from the spectral response of the photocurrent allow us to characterize the density of the localized states of the $Ge_{0.97}Si_{0.03}$:H thin films within the energy range from $hv = 0.8$ to $1.2eV$. The photocurrent changes four orders of magnitude in this energy range.

The parameters E_{Upc} and R_{def} revealed that when we reduce the deposition temperature, the $Ge_{0.97}Si_{0.03}$:H thin films do not suffer continuous structural changes. The lowest values of $R_{def} = 6.47$ and $E_{U_{pc}} = 47meV$ were obtained at a deposition temperature of $T_s = 160℃$ followed by the values obtained at the deposition

temperatures of $T_s = 70$ ($R_{def} = 22.4$ and $E_{U_{pc}} = 51.9meV$) and 300℃ ($R_{def} = 19.5$ and $E_{U_{pc}} = 53.2meV$), which indicates that at $T_s = 160$ and 70℃ the $Ge_{0.97}Si_{0.03}$:H thin films have a lower structural disorder and is very similar to the obtained at $T_s = 300$℃. These results agree with those reported in reference [50]. In reference [50] was reported that the Urbach Energy and the refractive index have their lowest value at a deposition temperature of $T_s = 160$℃. The Urbach energy had a value of $E_u = 33meV$ and the refractive index had a value of $n_\infty = 3.92$. These results indicate that the absorption by localized states in the valence and conduction band-tails and the density of silicon-germanium films is lower at a deposition temperature of $T_s = 160$℃. The films obtained at $T_s = 70$℃ do not have the best values but they are compatible with most commercial flexible substrates.

5.2 Development of Photovoltaic Devices Fabricated at INAOE

- The performance characteristics are used to evaluate the performance of photovoltaic devices and compare it with the performance of photovoltaic devices fabricated in other laboratories or with different semiconducting materials [56-59, 61-65]. In the section 4.3.1, the performance characteristics were used to develop the photovoltaic devices fabricated at the installations of INAOE. Unfortunately, the performance characteristics did not provide enough information to reveal and understand problems related with the operation of the photovoltaic devices and their technological problems.

The performance characteristics reveal that the a-Si:H thin films deposited between the interfaces of the intrinsic film of $Ge_{0.97}Si_{0.03}$:H directly affect the performance of the photovoltaic devices. The first indication of the effect caused by the intrinsic film of a-Si:H was revealed in the process 1076. In this process, the thickness of the a-Si:H film located between the p-i interface of the device was reduced from 500 to 350Å. In the process 1076, the short-circuit current and the open-circuit voltage reduce and

change their polarity from $I_{sc} = 0.98$ to $-0.03\mu A$ and from $V_{oc} = 0.48$ to $-0.1V$, respectively. This behavior indicates that the intrinsic film of a-Si:H located between the n-i interface of the device generates a built-in potential that reduce the open-circuit voltage and avoids the flow of charge. In the following processes was observed that the current increases from $I_{sc} = 0.98$ to $3.25\mu A$ with the increasing of the thickness of the intrinsic film of a-Si:H located at the p-i interface of the device. This behavior was attributed to that the increase of the thickness of the a-Si:H film increases the absorption of photons in the same and hence the generation of charge carriers which contribute to the flow of charge. Unfortunately, the current-voltage characteristics showed current suppression. The suppression of current was reduced by removing the silicon film located between the n-i interfaces of the device. Taking into account the above results we can declare that the current is improved because the intrinsic film of a-Si:H located between the p-i interface of the device contributes to the photogeneration of charge carriers. The electrons photogenerated in the intrinsic film of $Ge_{0.97}Si_{0.03}$:H also contributes to the performance of the device. Unfortunately, the a-Si:H film located between the n-i interface of the device generates a potential barrier that prevents that the holes photogenerated in the intrinsic film of $Ge_{0.97}Si_{0.03}$:H contribute to the performance of the device. This barrier allows that the holes photogenerated in the intrinsic film of a-Si:H control the operation of the device. In reference [41] was reported that by increasing the thickness of the a-Si:H film deposited between the p-i interface of the photovoltaic device from 0 to 2500Å, the open-circuit voltage increases from $V_{oc} = 0.65$ to $0.71V$. This results agree with the results obtained in our devices but the results do not agree when the thickness of the a-Si:H film deposited between the n-i interface of the photovoltaic device increases from 0 to 1500Å. In this case, the open-circuit voltage increases from $V_{oc} = 0.645$ to $0.705V$ but decreases slightly from $V_{oc} = 0.705$ to $0.692V$ when the a-Si:H film increases from 1500 to 2500Å.

- The spectral characteristics are used commonly to evaluate the performance of the photovoltaic devices [56, 59, 63, 65]. In the section 4.3.2, the spectral

characteristics in function of the structural configuration were used to determine the contribution of the thin films of a-Si:H and $Ge_{0.97}Si_{0.03}$:H during the development of the photovoltaic devices. The structural quality of the intrinsic films of the devices was monitored by means of the spectral characteristics.

The spectral characteristics revealed that both the a-Si:H film and the $Ge_{0.97}Si_{0.03}$:H film contributes to the performance of photovoltaic devices. The spectral characteristics in the process 1076 showed that when we reduce the thickness of the intrinsic film of a-Si:H located between the p-i interface from 500 to 350Å, the short circuit current only reduces within the energy range from $hv = 1.8$ to $3.8eV$. The current measured within the energy range from $hv = 1$ to $1.8eV$ does not show a significant change. This behavior indicates that the intrinsic film of $Ge_{0.97}Si_{0.03}$:H contributes in the entire range of measured energy. In the following processes was observed that if we continue increasing the thickness of the intrinsic film of a-Si:H from 500 to 630Å, the contribution of both films is increased. But if we increase the thickness of the intrinsic film of a-Si:H from 630 to 715Å the contribution of the a-Si:H film is increased and the contribution of the $Ge_{0.97}Si_{0.03}$:H film is reduced because the absorption of photons in it is reduced. Moreover, when we remove the intrinsic film of a-Si:H located between the n-i interface of the device, the contribution of both films is increased throughout the measured energy range. With these results we see that indeed the silicon film located between the n-i interface of the device prevents the flow of charge carriers photogenerated in the intrinsic films of a-Si:H and $Ge_{0.97}Si_{0.03}$:H.

- The temperature dependence of the spectral response of short-circuit current revealed that the short-circuit current increase throughout the energy range measured and it is shifted to lower photon energies when we increase the temperature from $T_s = 300$ to $460°K$. From the spectral response of the short-circuit current was obtained the hopping activation energy for a photon energy of $hv = 1.8$ $(E_a = 144meV)$, 3 $(E_a = 56.6meV)$, and $3.8eV$ $(E_a =$

$60.6meV$). The lower hopping activation energy was obtained at a photon energy of $hv = 3eV$. On the other hand, the ratio of surface recombination reduces from $SR = 2.5$ to 2.2 when the temperature increases from $T_s = 300$ to $420°K$. When the temperature increases from $T_s = 420$ to $460°K$ the ratio of surface recombination increases from $SR = 2.2$ to ≈ 2.5. The deposition temperature is $T_d = 433°K$. Temperatures higher than the deposition temperature may cause thermal annealing. Unfortunately, information like this is not reported commonly in the state-of-art and it is not possible compare our results.

- Dark current-voltage characteristics are reported in literature [57, 59] but without analysis of the parasitic resistances, diode ideality factor, and saturation current. In the section 4.3.4, the dark current-voltage characteristics were used to determine the effect of parasitic resistances and the quality of the junctions during the development of the photovoltaic devices.

Dark current-voltage characteristics revealed that the diode of the photovoltaic devices becomes more "leaky" when we increase the thickness of the intrinsic film of a-Si:H located between the p-i interface of the photovoltaic device. The quality of the diode enhanced when we remove the intrinsic film of a-Si:H located between the n-i interface of the photovoltaic device. The behavior observed in the diode was attributed to losses related to the parasitic series resistance of the devices. In Figure 4.28 we can see that the current reduces when we increase the thickness of the intrinsic film of a-Si:H located between the p-i interface of the devices (see the current at a voltage of $V = 5V$).

The losses related to the leakage current (Shunt resistance) reduce when we increase the thickness of the intrinsic film of a-Si:H located between the p-i interface of the devices and when we remove the intrinsic film of a-Si:H located between the n-i interface of the device.

5.3 Performance Characteristics of Fotovoltaic Devices Fabricated with Different Semiconducting Materials

The performance characteristics revealed that depending on the technology used, the performance characteristics vary in a different way when we change the operating point of the device. The μc-Si:H device has the highest value of the short-circuit current but the lowest value of the open-circuit voltage. This behavior was mainly attributed to the optical bandgap of μc-Si:H is narrower than the optical band gap of pm-Si:H for example. An optical band gap lower results in a better absorption of the solar spectrum. The width of the optical band gap of $Ge_{0.97}Si_{0.03}$:H is similar to the width of the optical band gap of μc-Si:H. Therefore, the value of the current measured in the device of $Ge_{0.97}Si_{0.03}$:H should be similar to the value of the current measured in the device of μc-Si:H. The results showed that the a-Si:H/$Ge_{0.97}Si_{0.03}$:H photovoltaic device has the lowest value of current indicating that the losses caused by the parasitic elements are higher in this device. Increasing the load resistance, the value of the current reduces faster than in the other devices.

5.4 Diagnostic of the Fotovoltaic Devices Fabricated with Different Semiconducting Materials

The diagnostic characteristics of non-crystalline photovoltaic devices are not reported commonly in the state-of-art [55, 59-60]. The diagnostic characteristics help us to understand the physical mechanisms of operation of the photovoltaic devices. A more precise knowledge about the physical mechanisms that govern the operation of the photovoltaic devices helps us to identify some problems related with the manufacturing technology, the quality of the junctions, the quality of the intrinsic material, the metallic contacts, the optical and electrical properties of the materials that make up the device, etc.

From Section 4.4 to Section 4.10, the characterization techniques described in Chapter 3 (Methodologies and Characterization Techniques) are used for a diagnosis of the photovoltaic devices manufactured with different materials (organic and non-organic materials) in different laboratories (Ecole-polytechnique, France, University of Cologne, Germany, and INAOE, Mexico) to try to show the importance of the diagnostic characteristics in non-crystalline photovoltaic devices.

5.4.1 Losses Caused by the Parasitic Resistances in the Photovoltaic Devices Fabricated with µc-Si:H and pm-Si:H Thin Films

The losses caused by parasitic resistances were studied and analyzed in µc-Si:H and pm-Si:H photovoltaic devices. In these results the energy conversion efficiency is approximately the same for µc-Si:H ($\eta = 7.07\%$) and pm-Si:H ($\eta = 6.64\%$) photovoltaic devices but the short-circuit current density and fill factor are larger in µc-Si:H ($J_{sc} = 25.3\, mA/cm^2$ and $FF = 0.63$) than those in pm-Si:H ($J_{sc} = 11.8\, mA/cm^2$ and $FF = 0.56$). The open circuit voltage is larger in pm-Si:H ($V_{oc} = 0.89V$) than in µc-Si:H ($V_{oc} = 0.42V$). The analysis of data showed that without the losses caused by the parasitic elements (i.e., series and Shunt resistance), the diode in pm-Si:H structure has a higher efficiency ($\eta_d = 9.3\%$ with $FF = 0.77$) in comparison with the efficiency of the diode in µc-Si:H ($\eta_d = 7.86\%$ with $FF = 0.72$). In other words, the parasitic resistance in the structure of µc-Si:H ($R_{Sh} = (2.9 \pm 0.2) * 10^3 \Omega$ and $R_s = (20.5 \pm 0.6)\Omega$) reduces the efficiency by about 12% while in the structure of pm-Si:H ($R_{Sh} = (1.09 \pm 0.02) * 10^4 \Omega$ and $R_s = (247 \pm 5)\Omega$) reduce the efficiency by about 30%. This type of analysis is not reported in the state-of-art and for this reason we can not make a comparison of our results.

5.4.2 Diagnostic of the µc-Si:H and pm-Si:H Photovoltaic Devices by means of the Temperature Dependence of Dark Current-Voltage Characteristics

As it was mentioned previously, the dark current-voltage characteristics are reported in the state-of-art but without analysis of parasitic resistances, diode ideality factor, and saturation current. In section 4.10, the parasitic resistances, diode ideality factor, and saturation current in function of operating temperature are used to diagnose the µc-Si:H and pm-Si:H photovoltaic devices. The diagnostic characteristics in function of operating temperature revealed that:

- pm-Si:H photovoltaic device becomes more "leaky" with temperature (n increases with temperature) while µc-Si:H photovoltaic device demonstrate clearly opposite trend becoming less "leaky" with temperature. Origin of "leaky" behaviour in non-crystalline materials is related not only to recombination because of existence a great number of factors for leakage current (surface states, leakage through some non-junction channels, etc.).
- The parasitic series resitance has a dominant contribution of the electrodes (or more resistive one) in the µc-Si:H photovoltaic device (R_s increases with temperature) while in the pm-Si:H photovoltaic device the parasitic series resistance is controlled by low field region (R_s decreases with temperature).
- The parasitic shunt resistance shows similar behaviour with temperature in both photovoltaic devices but with different values for activation energy which suggest different physical mechanisms of conduction in both devices.

An analysis like the analysis performed in section 4.10 is not reported commonly in the state-of-art and is not possible to compare our results.

Chapter 6

Conclusions

In this thesis work we performed a systematic study of the optoelectronic properties of germanium-silicon thin films and related photovoltaic devices. The study was divided into three sections. In the first section was made a study of the optoelectronic characteristics of germanium-silicon thin films as a function of deposition temperature. In this study it was observed that the photoelectric and structural properties of germanium-silicon films do not have a linear behavior when the deposition temperature decreases from 300 to 70℃. The film with improved photoelectric and structural properties was obtained at a deposition temperature of 160℃. The results of this deposition temperature was used as a basis for the development of a-Si:H/$Ge_{0.97}Si_{0.03}$:H photovoltaic devices. The systematic study of the opto-electronic characteristics used for the development of the $Ge_{0.97}Si_{0.03}$:H photovoltaic devices is shown in the second section. Finally, in the third section was performed a systematic study of the performance characteristics of photovoltaic devices manufactured with different technologies (i.e., polymorphous and microcrystalline silicon, germanium-silicon alloys and organic materials). The results of this section show that depending on the technology used, the photovoltaic devices are faced with different problems, both technological and design which significantly affect the operation thereof.

Conclusions on $Ge_{0.97}Si_{0.03}$:H thin films

1. In this thesis work was performed a systematic study of the electronic properties of the intrinsic $Ge_{0.97}Si_{0.03}$:H thin films deposited at low temperature in the range of $T_d = 70$ to 300℃.
2. Non monotonous change of electronic characteristics (σ_{ph}, R_{def} and E_{Upc}) was observed with reducing of T_d from 300 to 70℃ (maximum and minimum values were obtained).
3. Low sub-gap absorption ($E_{Upc} = 51.9$, 47, and $53.2meV$) was observed at $T_d = 70$, 160 and 300℃. Optimal deposition temperature for fabrication of photovoltaic devices was accepted as $T_d = 160$℃ ($E_{Upc} = 47meV$ and $R_{def} = 6.47$). This deposition temperature agrees with the results obtained from absorption coefficient measurements in reference [50].
4. The quality of the films deposited at 70℃ was not the best ($E_{Upc} = 51.9meV$ and $R_{def} = 22.4$) but this deposition temperature is compatible with most of commercially available plastics.

Conclusions about the development of a-Si:H/$Ge_{0.97}Si_{0.03}$:H Photovoltaic Devices

1. A systematic study of electronic characteristics of photovoltaic devices including the performance characteristics and diagnostic characteristics was done. This study was performed by application of both original techniques (spectral dependence of sub-gap photoconductivity) and modified known techniques (dark I-V characteristics, I-V characteristics under illumination, I-V characteristics as a function of temperature) with advanced date processing. Investigation was performed with photovoltaic devices fabricated in Ecole-

Polytechnique, France (with μc-Si:H and pm-Si:H intrinsic layers) and INAOE (with a-Si:H and $Ge_{0.97}Si_{0.03}$:H intrinsic films).

2. The advanced characterization was used for developing of original photovoltaic structures with two intrinsic layers.
3. The advanced characterization revealed:
    a. The thickness of the intrinsic film of a-Si:H deposited between the p-i interface of the photovoltaic device contributes to the output current.
    b. The intrinsic film of a-Si:H deposited between the i-n interface of the photovoltaic device generates a potential barrier that reduce the current and voltage output.
    c. Both a-Si:H and $Ge_{0.97}Si_{0.03}$:H layers contribute to the output current.
    d. Both holes and electrons photogenerated in the intrinsic film of a-Si:H deposited between the p-i interface of the device contribute to the output current.
    e. Electrons photogenerated in the intrinsic film of $Ge_{0.97}Si_{0.03}$:H contribute to the output current but the holes photogenerated in the intrinsic film of $Ge_{0.97}Si_{0.03}$:H do not contribute to the output current because they have a potential barrier in the interface of the a-Si:H-$Ge_{0.97}Si_{0.03}$:H thin films that reduce their contribution.
    f. It is possible to increase the contribution of the holes photogenerated in the intrinsic film of $Ge_{0.97}Si_{0.03}$:H if the configuration of the photovoltaic device is changed from p-i-n to n-i-p configuration.
    g. The losses generated by the parasitic resistances reduce significantly the performance of photovoltaic devices.
    h. It is necessary to reduce the resistances of the metallic contacts to improve the performance of photovoltaic devices.
    i. The reduction of the length of the photovoltaic device increases the open-circuit voltage.

4. Using the results obtained on characterization, new photovoltaic structure n-i-i-p were developed and optimized (the fabrication has been developed in INAOE by Dr. I. Cosme and described in reference [50]). The best characteristics obtained are: $J_{sc} = 1.12x10^{-3}\, mA/cm^2$, $V_{oc} = 0.438mV$.
5. The studied p-i-i-n structures demonstrate that inside the structure there is a barrier suppresing hole current. Therefore further work is necessary to reduce the barrier to avoid current suppression. Would the internal barrier for holes be eliminated the p-i-i-n structures become competing with tandem p-i-n-p-i-n structures with principal advantage related to neck of n-p interface inside the structure.

Conclusions on the losses caused by the parasitic resistances of the photovoltaic devices

1. Diagnostic characteristics were used to study the losses caused by parasitic elements in photovoltaic structures of μc-Si:H and pm-Si:H.
2. Measured efficiency values in the structures of μc-Si:H ($\eta = 7.07\%$) and pm-Si:H ($\eta = 6.64\%$) were close, however, a more detailed analysis revealed that the efficiency of the diode in the pm-Si:H structure is higher ($\eta = 9.3\%$ with $FF = 0.77$) than of the diode in the μc-Si:H structure ($\eta = 7.86\%$ with $FF = 0.72$). The losses caused by parasitic resistances (Shunt, R_{Sh}, and series, R_S, resistances) are larger in the pm-Si:H structure.
3. Diagnostic characteristics (obtained from spectral response related to sub-gap absorption) of photovoltaic structures indicates that the density of band-tail states in the optical gap in μc-Si:H is less than in pm-Si:H films, i.e., $E_{Upc} = 49meV$ and $E_{Upc} = 52meV$, respectively. The defect ratio (R_{def}) is observed approximately equal for both samples.

4. In the polymorphous silicon structure, we observed a local maximum in the spectral response at $hv \approx 1.3eV$. This maximum could be related to the density of defects within the optical bandgap.
5. In the microcrystalline silicon structure, the spectral response for short-circuit current has a better performance for long wavelengths due to narrower optical bandgap and a worse performance for short wavelengths in comparison to that of polymorphous silicon structure suggesting higher surface recombination at the frontal interface.

Conclusion on temperature dependence of diagnostic characteristics

1. Temperature dependence of current-voltage characteristics has been studied in the temperature range of T = 300 up to 480K in pm-Si:H and μc-SiH solar cells with efficiency η = 6.64% and 7.07%, respectively.
2. Using conventional equivalent circuit diagram for junction, such elements as saturation current (I_s), diode ideality factor (n) for diode, shunt resistance (R_{sh}) and series resistance (R_s) were extracted as the parameters from I(V,T) best fit procedure. Temperature dependence of the above elements have been presented and analyzed. R_s(T) revealed qualitatively different trends in pm-Si:H (semiconductor like behavior) and in μc-Si:H (metal like behavior). Diode ideality factor n showed increase with temperature for pm-Si:H samples and decrease for μc-Si:H samples. Saturation current in pm-Si:H showed thermo activation with one characteristic energy, while for μc-Si:H two activation energies. Inverse shunt resistance as a function of temperature showed activation character with two characteristic energies. Unambiguous interpretation of the data obtained with only one model is impossible at present and additional experiments e.g. under illumination are required.

List of Figures

List of Tables

References

[1]. K. L. Chopra, P. D. Paulson, and V. Dutta, "Thin-film solar cells: Anoverview," Progr. Photovolt.: Res. Appl., vol. 12, no. 2/3, pp. 69–92, Mar.–May 2004.

[2]. Matsuda, A., M. Kayama, N. Ikuchi, Y. Imanishi, and K. Takada, 1986, Guiding Principle in Preparation of High-Photosensitive Hydrogenated Amorphous Si-Ge Alloys from Glow-Discharge Plasma, Jpn. J. Appl. Phys., 25:1, L54-L56.

[3]. Matsuda, A. and K. Tanaka, 1987, Guiding Principle for Preparing Highly Photosensitive Si-Based Amorphous Alloys, J. Non-Cryst. Solid, 97&98, 1367-1374.

[4]. Tanaka, K., 1989, Hydrogenated Amorphous Si and Its Alloy Materials: New Approach to Structural Control, Optoelect. Dev and Tech., 4:2, 143-153.

[5]. Pratima Agarwal, H. Povolny, S. Han, X. Deng, "Study of a-SiGe:H films and n–i–p devices used in high efficiency triple junction solar cells". Journal of Non-Crystalline Solids 299–302 (2002) 1213–1218.

[6]. Mursal, A. Supu, I. Usman, T. Winata, Sukirno, and M.Barmawi, "Growth of Amorphous Silicon Germanium (a-SiGe:H) Alloys Thin Film by PECVD". Indonesian Journal of Physics, Vol. 15 No.2, April 2004.

[7]. A.H. Mahan, Y. Xu, L.M. Gedvilas, R.C. Reedy and H.M. Branz, "a-SiGe:H Materials and Devices Deposited by Hot Wire CVD Using a Tantalum Filament Operated at Low Temperature". Prepared for the 31st IEEE Photovoltaics Specialists Conference and Exhibition Lake Buena Vista, Florida January 3–7, 2005.

[8]. Timilsina, R., & Biswas, P., "Voids and molecuar hydrogen in hydrogenated amorphous silicon". Bulletin of the American Physical Society, Volume 57 (2012).

[9]. Chakraborty, S., Bobela, D. C., Taylor, P. C., & Drabold, D. A. "Voids in Hydrogenated Amorphous Silicon: A Comparison of ab initio Simulations and Proton NMR Studies". MRS Proceedings, 1066, A11.2.1-A11.2.6, (2008).

[10]. Wang, C.-M., Huang, Y.-T., Kuo-Hsi, Y., Hsu, H.-J., Hsu, C.-H., Zan, H.-W., & Tsai, C.-C. "Influence of Hydrogen on the Germanium Incorporation in a-$Si_{1-x}Ge_x$:H for Thin-film Solar Cell Application". MRS Proceedings, 1245, A04.02.1-A04.02-6 (2010).

[11]. Origo, F., Hammer, P., Comedi, D., & Chambouleyron, I. The Effect of Ion-Bombardment on the Formation of Voids During Deposition of a-Ge:H. MRS Proceedings, 507, 477-482 (1998)

[12]. Mursal, Ida Usman, Toto Winata, Sukirno, Moehamad Barmawi, "Optimization of Deposition Parameters for high Quality a-SiGe:H Thin Films". JURNAL MATEMATIKA DAN SAINS, JUNI 2006, VOL. 11 NO. 2.

[13]. Baojun Yan, Lei Zhao, Bending Zhao, Jingwei Chen, Guanghong Wang, Hongwei Diao, and Wenjing Wang, "High-performance a-SiGe:H thin film prepared by plasma-enhanced chemical vapor deposition with high plasma power for solar-cell application". Phys. Status Solidi A 209, No. 12, 2527–2531 (2012). DOI: 10.1002/pssa.201228281.

[14]. Terakawa, A., M. Shima, K. Sayama, H. Tarui, S. Tsuda, H. Nishiwaki, and S. Nakano, 1993, Film Property Control of Hydrogenated Amorphous Silicon Germanium for Solar Cells, Jpn. J. Appl. Phys., 32, 4894-4899.

[15]. Chao-ChunWang, Dong-SingWuu, Shui-Yang Lien, Yang-Shih Lin, Chueh-Yang Liu, Chia-Hsum Hsu, and Chia-Fu Chen, "Characterization of Nanocrystalline SiGe Thin Film Solar Cell with Double Graded-Dead Absorption Layer". International Journal of Photoenergy, Volume 2012, Article ID 890284, 6 pages. Doi:10.1155/2012/890284.

[16]. Gopal G. Pethuraja, Roger E. Welser, Ashok K. Sood, Changwoo Lee, Nicholas J. Alexander, Harry Efstathiadis, Pradeep Haldar, Jennifer L. Harvey, "Effect of Ge Incorporation on Bandgap and Photosensitivity of Amorphous SiGe Thin Films". Materials Sciences and Applications, 2012, 3, 67-71. Doi.org/10.4236/msa.2012.32010.

[17]. M. Gunes, M. E. D. Yavas, J. Klomfass, F. Finger, "The effects of native and light induced defects on optoelectronic properties of hydrogenated amorphous

silicon–germanium (a-SiGe:H) alloy thin films". J Mater Sci: Mater Electron (2010) 21:153–159. DOI 10.1007/s10854-009-9886-3.

[18]. Mursal, S. Amiruddin, I. Usman, T. Winata, Sukirno, and M. Barmawi, "Substrate Temperature Control of Narrow Band Gap Hydrogenated Amorphous Silicon Germanium for Solar Cells". Asian J. Energy Environ., Vol. 5, Issue 3, (2004), pp. 211-222.

[19]. Long Gu, Huidong Yang, Guoguan Wen, Yanmin Li, "Substrate Temperature Influence on Properties of Amorphous Silicon-Germanium Thin Films Prepared by RF-PECVD". 978-1-4244-6554-5/11/$26.00 ©2011 IEEE.

[20]. D. L. Staebler and C. R. Wronski, "Reversible conductivity changes in discharge-produced amorphous Si". Applied Physics Letters, Vol. 31, Issue 4, 292 (1977). Doi.org/10.1063/1.89674.

[21]. H. Fritzsche, "Development in Understanding and Controlling the Staebler-Wronski Effect in a-Si:H". Annual Review of Materials Research, vol. 31, 2001, pp. 47 - 79.

[22]. V. Nádazdy and M. Zeman, "Origin of charged gap states in a-Si:H and their evolution during light soaking", Physical Review B, vol. 69, Apr. 2004, p. 165213.

[23]. A. Klaver and R. van Swaaij, "Modeling of light-induced degradation of amorphous silicon solar cells", Solar Energy Materials and Solar Cells, vol. 92, Jan. 2008, pp. 50 - 60.

[24]. D. Redfield, Appl. Phys. Lett. 52 (1988) 492.

[25]. D. Redfield, Proceedings of the 11th EC Photovoltaic Solar Energy Conference, Montreux, 1992, p. 179.

[26]. Akira Terakawa, Masaki Shima, Masao Isomura, Makoto Tanaka, Seiichi Kiyama, Shinya Tsuda, Hiroyuki Matsunami, "Effect of the optical gap on the temperature dependence of a-SiGe solar cell stability". Journal of Non-Crystalline Solids 227–230 (1998) 1267–1271.

[27]. M. Stutzmann, R. A. Street, C. C. Tsai, J. B. Boyce, S. E. Ready, J. Appl. Phys. 66, (1989).

[28]. G. Schumm, C. D. Abel, G. H. Bauer, Mater. Res. Soc. Symp. Proc. 258, 505 (1992).

[29]. J. Kolodzey, S. Aljishi, Z. E. Smith, V. Chu, R. Schwarz, S. Wagner, Mater. Res. Soc. Symp. Proc. 70, 237 (1986).

[30]. O. Breitenstein, J. P. Rakotoniaina, S. Neve, M. A. Green, Z. Jianhua, W. Aihua, and G. Hahn, Lock-in Thermography Investigation of Shunts in Screen-Printed and PERL Solar Cells (IEEE, Piscataway, NJ, 2002), pp. 430-433.

[31]. H. Hoppe, J. Bachmann, B. Muhsin, K.-H. Drue, I. Riedel, G. Gobsch, C. Buerhop-Lutz, C. J. Brabec, and V. Dyakonov, J. Appl. Phys. 107, 014505 (2010).

[32]. K. Bothe, K. Ramspeck, D. Hinken, C. Schinke, J. Schmidt, S. Herlufsen, R. Brendel, J. Bauer, J. M. Wagner, N. Zakharov, and O. Breitenstein, J. Appl. Phys. 106, 104510 (2009).

[33]. S. Dongaonkar, J. D. Servaites, G. M. Ford, S. Loser, J. Moore, R. M. Gelfand, H. Mohseni, H. W. Hillhouse, R. Agrawal, M. A. Ratner, T. J. Marks, M. S. Lundstrom, and M. A. Alam, "Universality of non-Ohmic shunt leakage in thin-film solar cells". J. Appl. Phys. 108, 124509 (2010). Doi: 10.1063/1.3518509.

[34]. J. W. Seo, S. J. Baik, S. J. Kang, Y. H. Hong, J.-H. Yang, L. Fang, and K. S. Lim, Appl. Phys. Lett. 96, 053504 (2010).

[35]. S. H. Jo and W. Lu, Nano Lett. 8, 392 (2008).

[36]. F. Meillaud, A. Shah, C. Droz, E. Vallat-Sauvain, C. Miazza, "Efficiency limits for single-junction and tandem solar cells". Solar Energy Materials and Solar Cells 90, issues 18-19, 2952-2959, 2006.

[37]. Takuya Matsui, Haijun Jia and Michio Kondo, "Thin film solar cells incorporating microcrystalline Si1–xGex as efficient infrared absorber: an application to double junction tandem solar cells". Prog. Photovolt: Res. Appl. 2010; 18:48–53. DOI: 10.1002/pip.922.

[38]. S.T. Chang, M.H. Liao, W. -K. Lin, "Si/SiGe hetero-junction solar cell with optimization design and theoretical analysis". Thin Solid Films 519 (2011) 5022–5025.

[39]. Qi Hua Fan, Xianbo Liao, Changyong Chen, Xianbi Xiang, Guofu Hou, William Ingler, Nirupama Adiga, Shibin Zhang, Wenhui Du, Xinmin Cao, Xunming Deng, "Numerical simulation and experimental investigation of a-si/a-sige tandem junction solar cells". Photovoltaic Specialists Conference (PVSC), 2010 35th IEEE. DOI: 10.1109/PVSC.2010.5617031.

[40]. Eiji Maruyama, Shingo Okamoto, Akira Terakawa, Wataru Shinohara, Makoto Tanaka, Seiichi Kiyama, "Toward stabilized 10% efficiency of large-area (>5000 cm2) a-Si/a-SiGe tandem solar cells using high-rate deposition". Solar Energy Materials & Solar Cells 74 (2002) 339–349.

[41]. D. Lundszien, F. Finger, H. Wagner, "A-Si:H buffer in a-SiGe:H solar cells". Solar Energy Materials & Solar Cells 74 (2002) 365–372.

[42]. Liborio Sánchez Morales. "Growth and Characterization of NanostructuredSilicon-Germanium Films depositedby LF PE CVD" [Phd. Thesis]. INAOE, Puebla, 2007.

[43]. William B. Jordan and Sigurd Wagner, "Electrical Properties of phosphorus-doped and Boron-doped nanocrystalline Germanium Thin-Films for p-i-n devices", Mater. Res. Soc. Symp. Proc., Vol. 762, pp. A5.7.1-A5.7.6, (2003).

[44]. A. Matsuda, "Formation kinetics and control of microcrystallite in μc-Si:H from glow discharge plasma" Journal of Non-crystalline Solids, Vol. 59&60, pp.767-774, (1983).

[45]. W. A. Turner, S. J. Jones, D. Pang, B. F. Bateman, J. H. Chen, Y.-M. Li, F. C. Marques, A. E. Wetsel, P. Wickboldt, W. Paul, J. Bodart, R. E. Norberg, I. El Zawawi and M. L. Theye, "Structural, optical, and electrical characterization of improved amorphous hydrogenated germanium", Journal of Applied Physics, Vol. 67 pp. 7430-7438, (1990).

[46]. Y. Nasuno, M. Kondo, and A. Matsuda, "Passivation of oxygen-related donors in microcrystalline silicon by low temperature deposition", Applied Physics Letters, Vol. 78(16), pp. 2330-2332, (2001).

[47]. F. Fajardo, D. Comedi, and I. Chambouleyron, “lndium and gallium p-type doping of hydrogenated amorphous germanium thin films”, Appl. Phys. Lett., Vol. 64(24), pp. 3273-3275, (1994).

[48]. I. Chambouleyron and A. R. Zanatta, “On the doping efficiency of nitrogen in hydrogenated amorphous germanium”, Appl. Phys. Lett., Vol. 62(1), pp. 58-60, (1993).

[49]. R. Martins, H. Aguas, V. Silva, I. Ferreira, A. Cabrita and E. Fortunato, “Nanostructured silicon films produced by PECVD”, Mat. Res. Soc. Symp. Proc., Vol. 664, pp. A9.6.1-A9.6.6, (2001).

[50]. Ismael Cosme Bolaños. “Study of GeSi:H materials deposited by PECVD at low temperatures (Td<200 °C) for device applications” [Phd. Thesis]. INAOE, Puebla, 2013.

[51]. Zhimeng Wu, Qingsong Lei, Jianping Xi, “Hydrogenated microcrystalline silicon films prepared by VHF-PECVD and single junction solar cell”, J. Mater SCI 41 (2006), 1721-1724.

[52]. N. I. Klyui, V. G. Litovchenko, A. N. Lukyanov, L. V. Neselevskaya, A. V. Sarikov, V. G. Dyskin, U. Kh. Gaziev, Z. S. Settarova, and M. N. Tursunov, “Influence of Deposition Conditions on the Antireflection Properties of Diamond-Like Carbon Films for Si-Based Solar Cells”, Technical Physics, 2006, vol. 51, No. 5, pp. 654-658.

[53]. M. Serin, N. Harder, R. Carius, “Investigation of the transport properties of microcrystalline silicon by time-of-flight (TOF)”, Journal of Materials Science: Materials in Electronics, 14 (2003), pp. 733-734.

[54]. H. Keppner, J. Meier, P. Torres, D. Fisher, A. Shah, “Microcrystalline silicon and micromorph tanden solar cells”, Appl. Phys. A. 69, 169-177 (1999).

[55]. Yuan Yujie, HOU GuoFu, ZHANG JianJun, XUE JunMing, CAO LiRan, ZHAO Ying, and GENG XinHua, “Performance improvement of n-i-p uc-Si:H solar cells by gradient hydrogen dilution technique”, Science in China Series E: Technological Sciences, Jun. 2009, vol. 52, No. 6, 1756-1761.

[56]. B. Rech, H. Wagner, “Potential of amorphous silicon for solar cells”, Appl. Phys. A 69, 155-167 (1999).

[57]. Erik V. Johnson, Pere Roca I Cabarrocas, “Spectral response and field enhanced revese current in a-Ge:H nip photodiodes”, Solar Energy Materials and Solar Cells 91 (2007), pp. 877-881.

[58]. A. I. Kosarev, Y. Poissant, A. S. Abramov, and P. Roca I Cabarrocas, “Effect of the recombination of photoinduced carriers at the frontal interface on the performance of amorphous silicon solar cells”.

[59]. Q. Zhang, E. V. Johnson, V. Djeridane, A. Abramov, and P. Roca I Cabarrocas, “Decouplin crystalline volume fraction and VOC in microcrystalline silicon pin solar cells by using a uc-SiF:H intrinsic layer”, phys. Stat. sol. (RRL) 2, No. 4, 154-156 (2008).

[60]. Y. M. Soro, A. Abramov, M. E. Gueunier-Farret, E. V. Johnson, C. Longeaud, P. Roca i Cabarrocas, J. P. Kleider, “Device grade hydrogenated polymorphous silicon deposited at high rates”, Journal of Non-Crystalline Solids (2008).

[61]. A. V. Shah, J. Meier, E. Vallat-Sauvain, N. Wyrsch, U. Kroll, C. Droz, U. Graf, “Material and solar cell research in microcrystalline silicon”, Solar Energy Materials and solar cells 78, issue 1-4, 469-491, 2003.

[62]. J. Meier, U. Kroll, E. Vallat-Sauvain, J. Spitznagel, U. Graf, A Shah, “Amorphous solar cells, the micromorph concept and the role of VHF-GD deposition technique”, Solar Energy 77, issue 6, 983-993, 2004.

[63]. Pere Roca i Cabarrocas, N Chaabane, A V Kharchenko and S Tchakarov, “Polymorphous silicon thin films produced in dusty plasmas: application to solar cells”, Plasma Phys. Control. Fusion 46 (2004) B235–B243.

[64]. P. Roca i Cabarrocas, Y. Djeridane, Th. Nguyen-Tran, E. V. Johnson, A. Abramov and Q. Zhang, “Low Temperature plasma synthesis of silicon nanocrystals: a strategy for high deposition rate and efficient polymorphous and microcrystalline soalr cells”, Plasma Phys. Control. Fusion 50 (2008), 124037 (9pp).

[65]. Q. Zhang, E. V. Johnson, V. Djeridane, A. Abramov, and P. Roca I Cabarrocas, "Decoupling crystalline volume fraction and VOC in microcrystalline silicon pin solar cells by using a μc-Si:F:H intrinsic layer". Phys. Stat. Sol. 2, No. 4, 154-156 (2008).

[66]. G. Juska, K. Arlauskas, M. Viliunas, and J. Kocka, Phys. Rev. Lett. 84, 4946 (2000).

[67]. Sebastian Bange, Marcel Schubert, and Dieter Neher, Phys. Rev. B 81, 035209 (2010).

[68]. Fancisco Temoltzi Avila, "Estudio de las características electrónicas en base a la fotoconductividad en películas de silicio-germanio y dispositivos semiconductores" [MC. Thesis]. INAOE, Puebla, 2013.

List of Publications

1. **Andrey Kosarev and Francisco Avila**, "Sub-gap Photoconductivity in Germanium-silicon Films Deposited by Low Frequency Plasma". Mater. Res. Soc. Symp. Proc., 1245,1245-A17-04 (2010). DOI: 10.1557/PROC-1245-A17-04 (ISBN: 9781605112220).
2. **Francisco Avila, Andrey Kosarev, Ismael Cosme**, "Sub-gap Photoconductivity in Ge_xSi_{1-x}:H Films Deposited by Low Frequency Plasma at Different Substrate Temperatures". Conference proceedings of International Congress on Instrumentation and Applied Sciences 2011, 6 pages (ISBN: 978-607-02-2298-6).
3. **Francisco Avila, Andrey Kosarev, Ismael Cosme1, Mario Moreno, Pere Roca i Cabarrocas**, "Electronic Characteristics of PIN Photovoltaic Structures Made of Polymorphous and Microcrystalline Silicon Deposited by Plasma". Conference proceedings of International Congress on Instrumentation and Applied Sciences 2011, 8 pages (ISBN: 978-607-02-2298-6).
4. **I. Cosme, A. Kosarev, F. Temoltzi, A. Itzmoyotl**, "Electronic Properties of Ge_ySi_{1-y}:H Films Deposited by LF PECVD at Low Temperatures". 2011 8th International Conference on Electrical Engineering, Computing Science and Automatic Control, pag. 995-998 (ISBN: 978-1-4577-1013-1).
5. **I. Cosme, A. Kosarev, F. Temoltzi, A. Itzmoyotl**, "Study of Doping of $Ge_{0.96}Si_{0.04}$:H Films with B, and P During Low Frequency Plasma Deposition at Low Temperature". 2011 8th International Conference on Electrical Engineering, Computing Science and Automatic Control, pag. 999-1001 (ISBN: 978-1-4577-1013-1).
6. **Francisco Temoltzi Avila, Andrey Kosarev, Ismael Cosme, Mario Moreno, P. Roca y Cabarrocas**, "Temperature dependence of current-voltage characteristics in μc-Si:H and pm-Si:H PIN structures". Mater. Res. Soc. Symp. Proc., 1426, 2012, DOI: 10.1557/opl.2012.1176 (ISBN: 9781605114033).

7. **Ismael Cosme, Andrey Kosarev, Francisco Temoltzi and Adrian Itzmoyotl**, "Comparison of Doping of Ge_ySi_{1-y}:H (y > 0.95) Films Deposited by Low Frequency PECVD at High (300ºC) and Low (160ºC) Temperatures". Mater. Res. Soc. Symp. Proc., 1426, 2012, DOI: 10.1557/opl.2012.865 (ISBN: 9781605114033).

List of Conferences

1. **Sub-gap Photoconductivity in Germanium-silicon Films Deposited by Low Frequency Plasma**. Andrey Kosarev and Francisco Avila. MRS 2010 Spring Meeting; Symposium A: Amorphous and Polycrystalline Thin-Film Silicon and Technology, San Francisco, California, USA (2010).
2. **Comparison of Electronic Characteristics of PIN Photovoltaic Structure made of Polymorphous and Microcrystalline Silicon Deposited by Plasma**. Francisco Avila, Andrey Kosarev, Ismael Cosme1, Mario Moreno, Pere Roca i Cabarrocas.
    a. 11º Encuentro de Investigación, 4-5 de Noviembre del 2010. INAOE, Puebla, México.
    b. II International workshop Advanced Materials for Optoelectronics and Related Physics 2010, October 11-15, INAOE, Puebla, México.
3. **Sub-gap Photoconductivity in Ge_xSi_{1-x}:H Films Deposited by Low Frequency Plasma at Different Substrate Temperatures**. Francisco Avila, Andrey Kosarev, Ismael Cosme.
    a. II International workshop Advanced Materials for Optoelectronics and Related Physics 2010, October 11-15, INAOE, Puebla, México.
    b. Photovoltaics, Solar Energy Materials & Technologies Symposium at the XX International Materials Research Congress held in Cancun, Mexico from August 14th to 19th, 2011.
    c. 2nd International Congress on Instrumentation and Applied Sciences, Puebla, Puebla, México, October 5-8, 2011.
4. **Electronic Characteristics of PIN Photovoltaic Structures Made of Polymorphous and Microcrystalline Silicon Deposited by Plasma**. Francisco Avila, Andrey Kosarev, Ismael Cosme1, Mario Moreno, Pere Roca i Cabarrocas.

a. Photovoltaics, Solar Energy Materials & Technologies Symposium at the XX International Materials Research Congress held in Cancun, Mexico from August 14th to 19th, 2011. 6.
b. 2nd International Congress on Instrumentation and Applied Sciences, Puebla, Puebla, México, October 5-8, 2011.

5. **Study of Optical and Electrical Properties of Ge_ySi_{1-y}:H Films Deposited by Low Temperature PECVD Process**. Ismael Cosme, Andrey Kosarev, Francisco Temoltzi, Adrian Itzmoyotl. Photovoltaics, Solar Energy Materials & Technologies Symposium at the XX International Materials Research Congress held in Cancun, Mexico from August 14th to 19th, 2011.
6. **Electronic properties of $Ge_{0.97}Si_{0.03}$:H Films Doped with B, and P Deposited by Low Frequency PECVD Process at Low Temperature**. Ismael Cosme, Andrey Kosarev, Francisco Temoltzi, Adrian Itzmoyotl.
    a. Electrical Engineering Computing Science and Automatic Control (CCE), 2011 8th International Conference on, Merida, Yucatan, México.
    b. Photovoltaics, Solar Energy Materials & Technologies Symposium at the XX International Materials Research Congress held in Cancun, Mexico from August 14th to 19th, 2011.
7. **Study of doping of $Ge_{0.96}Si_{0.04}$:H films with B, and P during low frequency plasma deposition at low temperature**. Electrical Engineering Computing Science and Automatic Control (CCE), 2012 8th International Conference on Merida, Yucatan, México.
8. **Photo-Electronic Characteristics of a-Si:H/a-$Ge_{0.97}Si_{0.03}$:H Photovoltaic Devices and Their Relation to the Device Configuration**. Francisco T. Avila, Andrey Kosarev, Oleksandr Malik. International workshop Advanced Materials for Optoelectronics and Related Physics 2012, October 8-12, INAOE, Puebla, México.
9. **Temperature dependence of current-voltage characteristics in µc-Si:H and pm-Si:H PIN structures**. Francisco Temoltzi Avila, Andrey Kosarev, Ismael Cosme, Mario Moreno, P. Roca y Cabarrocas. MRS 2012 Spring Meeting;

Symposium A: Amorphous and Polycrystalline Thin-Film Silicon and Technology, San Francisco, California, USA (2012).

10. **Comparison of Doping of Ge_ySi_{1-y}:H (y > 0.95) Films Deposited by Low Frequency PECVD at High (300°C) and Low (160°C) Temperatures**. Ismael Cosme, Andrey Kosarev, Francisco Temoltzi and Adrian Itzmoyotl. MRS 2012 Spring Meeting; Symposium A: Amorphous and Polycrystalline Thin-Film Silicon and Technology, San Francisco, California, USA (2012).
11. **Photo-electronic Characteristics of a-Si:H/a-$Ge_{0.97}Si_{0.03}$:H Photovoltaic Devices and Their Relation to the Device Configuration**. Francisco T. Avila, Andrey Kosarev, and Oleksandr Malik. 25th International Conference on Amorphous and Nano-crystalline Semiconductors (ICANS25). August 18–23, 2013 Toronto, Ontario Canada.

List of Proyects

1. “Photovoltaic solar cells based in silicon-germanium deposited by plasma on flexible substrates” No. 152244 (2011-2013) Mexican Council for Science and Technology-CONACyT.